Optical Properties of Bilayer Graphene Quantum Dots

Matthew Albert

Thesis submitted to the University of Ottawa
in partial Fulfillment of the requirements for the
Master's degree in Physics

Department of Physics
Faculty of Sciences
University of Ottawa

Abstract

In this thesis, we study graphene's optical and electrical properties, primarily focusing on bilayer graphene (BLG) quantum dots (QDs). We discuss a tight-binding model to accurately model the single-particle behavior of monolayer and bilayer graphene. Additionally, we introduce theoretical and numerical methods, including the many-body Hamiltonian, configuration interaction method, Bethe-Salpeter equation (BSE), and computation of Coulomb matrix elements to analyze electron-electron interactions in many-body systems.

We examine gated BLG under a perpendicular electric field, which opens a gap in the band structure. Next, lateral gates can be applied in a way that leads to the emergence of a QD that effectively confines electrons and holes. Employing an atomistic tight-binding model for millions of atoms, we compute the single-particle QD energy spectrum and dipole matrix elements (DMEs) to analyze the oscillator strengths and optical selection rules. We incorporate electron-electron interactions via microscopic Coulomb matrix elements and solve the BSE to obtain the excitonic energy spectrum. Furthermore, we obtain the excitonic absorption spectrum and predict the existence of dark low-energy exciton states.

Subsequently, we examine the effects of a shallow lateral confining potential and trigonal warping (TW) on the electronic structure of laterally gated BLG QDs. We begin by analyzing the influence of TW on the QD energy spectrum as the confining potential depth varies. We find a regime where the QD levels are dominated by the presence of three minivalleys for each K-valley. We obtain the absorption spectrum for a shallow confining potential depth, which further amplifies the effects of TW on the optical properties. Our results predict two degenerate bright exciton states, each built of the three minivalley states.

Finally, we utilize an effective mass model for BLG QDs to explain the previously observed optical selection rules, where TW effects were neglected. Labeling the QD states with a generalized angular momentum gives deeper insights into the selection rules that were not apparent in the atomistic model. Understanding interacting electrons and holes

in gated BLG QDs opens potential applications in storing, detecting, and manipulating photons in the terahertz (THz) energy range.

Acknowledgements

I would like to express my gratitude to everyone who supported and guided me throughout my academic journey. First, I would like to thank my research supervisor, Dr. Pawel Hawrylak, for welcoming me to the Quantum theory research group during my undergraduate Honours project and my master's degree. He has taught me so much about conducting good research and how to think about physics. I am very grateful for his guidance and would like to continue collaborating with him as I pursue my PhD at the University of Toronto.

Next, I would like to thank the other group members. Beginning with Dr. Yasser Saleem, who was a great TA for mechanics and quantum mechanics. Although he was strict with marking, he enhanced my learning by pushing me to write everything clearly and systematically. I am thankful for his patience and guidance during my Honours project when I was new to research and throughout my master's. Also, Dr. Daniel Miravet would help me with any physics concepts and numerical troubles I encountered despite his hectic schedule. Dr. Ibsal Assi, a new group member, quickly became friends with me, and we enjoyed many spirited conversations and laughs. Alina Wania Rodrigues and Mahan Mohseni are both PhD students, and I enjoyed talking to you both in the office and outside of group meetings. Dr. Marek Korkusinski for helping me along the way and for fruitful discussions during group meetings.

In addition, I would like to thank Professor Liang Chen for giving me the opportunity to conduct summer research after finishing my third year of undergrad without any prior research experience. I enjoyed our collaboration and the two papers we wrote together. I will be forever grateful for that first learning opportunity to get me started along my research journey, which has helped me a lot throughout my career.

I would like to thank my childhood friends John Kasimatis and Ivan Quintero for being there to hang out or talk whenever I needed it most. We are the Three Musketeers. Finally, I would like to thank my Mom, my dad, and my relatives for their love and support. I would not be where I am today nor the person that I have become without them.

Acronyms

BLG	Bilayer graphene
BLG QD	Bilayer graphene quantum dot
BSE	Bethe-Salpeter equation
CB	Conduction band
CI	Configuration interaction
DME	Dipole matrix elements
FT	Fourier transform
GS	Ground state
NN	Nearest neighbour
NNN	Next nearest neighbour
QD	Quantum dot
TB	Tight binding
THz	Terahertz
TW	Trigonal warping

VB	Valence band
X	Exciton

Table of Contents

List of Figures

List of Tables

Chapter 1

Introduction

1.1 Graphene

Graphene rose into the spotlight with its first isolation by Andre Geim and Konstantin Novoselov at the University of Manchester in 2004 [1], an achievement that earned them the Nobel Prize in 2010. They pioneered an ingenious and inexpensive method to obtain a single graphene layer from graphite, consisting of many stacked graphene layers. Using ordinary sticky tape, they peeled off a single layer of graphene from graphite and studied the electronic properties of these thin graphene sheets in the presence of an externally applied electric field, observing properties characteristic of those found in two-dimensional semimetals. This groundbreaking work has ignited interest in graphene throughout the scientific community ever since.

The band structure of graphene was initially analyzed theoretically by P.R. Wallace in 1946 [2], which displayed linear dispersion around the Dirac points where the conduction and valence bands meet, resembling the dispersion of massless Dirac fermions [3,4]. Among the two-dimensional materials, bilayer graphene, consisting of two single layers of graphene stacked on top of each other, has attracted significant interest [5–11]. BLG provides a more complex system due to interactions between atoms on two graphene layers, resulting in parabolic low-energy dispersion similar to that of massive chiral quasiparticles [12–14],

although the energy gap remains closed [15]. By using lateral gates, an electric field can be applied perpendicular to the two layers, opening the energy gap and yielding a voltage-tunable semiconductor [16–23]. The size of the band gap can be controlled by the strength of the displacement field, making it tunable from zero to the mid-infrared energy range [24]. The bandgap plays a key role in the optical and electrical properties of a material; therefore, the continuously tunable band gap found in gated BLG has facilitated insulating states [25], gate-tunable excitons [26, 27], and phase transitions in fractional quantum Hall states [28]. Furthermore, this tunability enables various applications in nanoelectronic and nanophotonics devices [17, 27].

Additionally, twisting the layers of BLG relative to each other results in vast changes in the band structure compared to untwisted BLG. Twisted BLG has become a highly researched material, with the magic twist angle of approximately 1.1 degrees resulting in flat bands [29–31] and sharp peaks in the density of states, which has lead to magnetism [32], superconductivity [33–36] and correlated insulating phases [37–40] at low temperatures. Moreover, there have been studies of twisted trilayer [41–44] and even twisted quadrilayer graphene [45, 46], which present a higher level of complexity with a variety of twist angles between different layers, spanning a very large parameter space. However, this thesis will focus primarily on BLG, particularly BLG QDs.

1.2 Quantum dots

Quantum dots enable the confinement of electrons or holes, allowing for improved control and manipulation over the properties of these charge carriers [47]. Self-assembled and graphene QDs garnered much attention [48–51] for their ability to confine electrons and holes simultaneously due to their structure with a multitude of applications, including lasers [52], light emitting diodes (LEDs) [53], storage devices [54], and sources of entangled photon pairs via biexciton-exciton cascade [55–57]. However, their optical properties are challenging to tune once engineered. In contrast, the gate voltages permit easy tunability of the optical and electrical properties of lateral QDs [58–60]. The main shortcomings of

lateral QDs are that they confine either electrons or holes, but not both simultaneously [61, 62].

Interestingly, lateral gates can be applied to BLG in a way to create a QD that effectively confines both electrons and holes [60, 63–65] and also allows for high tunability of the optical and electronic properties through lateral gate voltages. The ability to confine electrons and holes simultaneously, and hence confine excitons with high tunability via gate voltages, provides an ideal system for studying electrically tunable confined excitons that couple strongly to light [65, 66]. This has motivated Chapter 3, where we will discuss the formation of excitons in BLG QDs and study their fine structure. Finally, the weak spin-orbit interaction and low hyperfine coupling present in BLG [67, 68] promise long coherence times [69], which demonstrates that BLG QDs are a promising candidate for well-controlled long-lived valley and spin-valley qubits [70–76].

1.3 Thesis contributions

The contents of this thesis are based on research published in peer-reviewed journals, manuscripts currently under peer review, as well as nonpublished research conducted during my master's. A list of manuscripts related to this thesis are:

1. K. Sadecka, Y. Saleem, D. Miravet, M. Albert, M. Korkusinski, G. Bester, and P. Hawrylak, *Electrically tunable fine structure of negatively charged excitons in gated bilayer graphene quantum dots*, Phys. Rev. B, 109, 085434 (2023).

2. M. Albert, D. Miravet, Y. Saleem, K. Sadecka, M. Korkusinski, G. Bester, and P. Hawrylak, *Optical properties of gated bilayer graphene quantum dots with trigonal warping*, arXiv:2405.09725 [cond-mat], submitted for publication to Phys. Rev. B, 2024.

For manuscript 1, I am a co-author in collaboration with other members of the Quantum Theory Group. I reproduced all calculations and derivations involving gated BLG band

structure, QD energy spectrum, and DME with TW. Later, I extended the previous theory of excitons established and studied the effects of a shallow confining potential depth and TW on the optical properties of gated BLG QDs, resulting in Manuscript 2 and Chapter 4 in this thesis.

1.4 Thesis outline

The thesis is organized as follows: Chapter 1 introduces the topics covered in the thesis, including the history, motivation, and applications of graphene research. Next, Chapter 2 presents the numerical and theoretical methods utilized throughout this thesis.

In Chapter 3, we study gated BLG and introduce gated BLG QDs through lateral gates, allowing the confinement of electrons and holes on separate layers of the BLG system. We compute the QD energy spectrum and dipole matrix elements to study the optical selection rules. We also examine excitons in a many-body system and the absorption spectrum, neglecting the effects of trigonal warping.

Chapter 4 discusses the combined effects of a shallow confining potential depth and the presence of minivalleys on the resulting QD energy levels due to TW. We analyze the influence of TW on the energy spectrum as the confining potential depth varies, identifying a regime where three minivalleys for each K-valley dominate the QD conduction and valence band levels. Considering both K-valleys, this results in six-fold degenerate QD levels, which become twelve-fold degenerate when including spin. We also study the effects of TW on the optical selection rules, exciton spectrum, and absorption spectrum for a shallow confining potential depth, which amplifies the effects of TW on the optical properties.

Chapter 5 presents an effective mass model for BLG QDs that considers parabolic and Gaussian confining potentials separately. This model aims to explain better the optical selection rules obtained in Chapter 3, where the effects of trigonal warping were neglected.

Chapter 2

Methodology

This chapter will discuss the models and numerical methods utilized throughout this thesis. Section 2.1 will begin with a discussion of an atomistic tight-binding model, which will be the building block for our analysis. The analysis is conducted in the single electron picture for monolayer bulk graphene, and an extension will be made to bulk bilayer graphene. Here, we will construct the bulk Hamiltonian for both monolayer and bilayer graphene and study the electronic properties, such as the band structure.

Then, we will study the many-body Hamiltonian, which we will use to describe a more complex system consisting of multiple electrons, including the electron-electron interactions via Columb matrix elements. We will explain how to derive and compute these Coulomb matrix elements numerically. Additionally, we will outline a derivation of the Bethe-Salpeter equation (BSE), which we will use to solve for the exciton energy spectrum and wavefunctions when we study bilayer graphene quantum dots.

Finally, we will conclude with an essential numerical technique called the configuration interaction (CI) method. This method allows us to obtain solutions consisting of multiple electron-hole pair configurations and represents a fully numerical alternative to the BSE equation. One can use CI to study one and two-electron-hole pair excitations, particularly biexcitons, and their interaction and mixing with excitons in BLG QDs.

2.1 Tight-binding model

The tight-binding model is a commonly employed method to accurately and simply model the electrical properties of graphene and other two-dimensional materials, such as MoS_2 [77] and WSe_2 [61]. It allows for an accurate prediction of the band structure in large systems consisting of millions of atoms. Let's consider the Hamiltonian describing an electron in the presence of a single effective atom $H_{\text{at}}(\vec{r})$:

$$H_{\text{at}}(\vec{r}) = -\frac{\hbar^2}{2m}\nabla^2 + V_{\text{at}}(\vec{r}), \tag{2.1}$$

where the first term represents the kinetic energy of the electron and the second term accounts for the interaction with the effective potential of the atom. Consider eigenstates $\phi_m(\vec{r})$ of the single effective atom Hamiltonian, they satisfy the Schrodinger equation:

$$H_{\text{at}}(\vec{r})\phi_m(\vec{r}) = \varepsilon_m \phi_m(\vec{r}), \tag{2.2}$$

where ε_m are the energy levels with eigenfunctions $\phi_m(\vec{r})$. If we consider the Hamiltonian of an electron in a crystal with N atoms:

$$H(\vec{r}) = -\frac{\hbar^2}{2m}\nabla^2 + \sum_{n=1}^{N} V_{\text{at}}(\vec{r} - \vec{R}_n). \tag{2.3}$$

To diagonalize $H(\vec{r})$, we can write our wavefunction as a linear combination of atomic orbitals m centered on an atom n at position $\vec{R}_n$:

$$\psi(\vec{r}) = \sum_{n=1}^{N} C_n \, \phi_m(\vec{r} - \vec{R}_n). \tag{2.4}$$

Using the wavefunction form in Eq. (2.1), one can construct the Hamiltonian of the crystal and diagonalize it to obtain the eigenvalues. The tight-binding model assumes that the overlap of wavefunctions localized on different atoms is minimal and that the electron on a single atom is tightly bound. This assumption means that the orbitals are essentially

orthogonal to one another, i.e.:

$$\int \phi_m^*(\vec{r} - R_{n'})\phi_m(\vec{r} - R_{m'})d\vec{r} = \delta_{n',m'}, \tag{2.5}$$

which is the overlap between m orbitals localized on atoms n' and m'. In the subsequent sections, we will use the tight-binding model to obtain the band structure of bulk monolayer and bilayer graphene, and we will consider Slater-like p_z orbitals, which have the following form [3]:

$$\phi_z(\vec{r} - \vec{R}_i) = \left(\frac{\xi^5}{32\pi}\right)^{\frac{1}{2}} (z - z_i)e^{\frac{-\xi|\vec{r}-\vec{r}_i|}{2}}, \tag{2.6}$$

where $\xi = 3.25$ in units of inverse Bohr radii and $\vec{r}_i$ is the position of the carbon atom i in Bohr radii.

2.1.1 Tight-binding model for bulk graphene

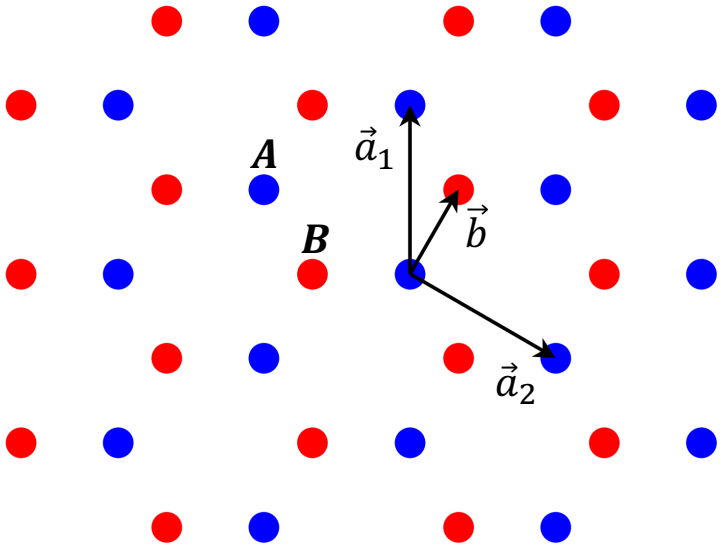

Figure 2.1: Structure of monolayer graphene with atoms on sublattice A (blue) and B (red). The primitive unit cell vectors $\vec{a}_1$ and $\vec{a}_2$, and the nearest neighbour vector $\vec{b}$ are illustrated.

In this section, we will derive the Hamiltonian for a single layer of bulk graphene and study the resulting band structure following Wallace's derivation in 1946 [2, 3]. Graphene consists of carbon atoms arranged in a hexagonal honeycomb pattern, as depicted in Fig. 2.1. The unit cell comprises one atom from sublattice A and one from sublattice B, with the selected unit cell vectors defined as $\vec{a}_1 = a(0, \sqrt{3})$ and $\vec{a}_2 = \frac{a}{2}(3, -\sqrt{3})$, where the NN in-plane bond length is $a = 0.143$ nm. The positions of the atoms within sublattices A and B are given by:

$$\vec{R}_A = n\vec{a}_1 + m\vec{a}_2, \tag{2.7}$$

$$\vec{R}_B = n\vec{a}_1 + m\vec{a}_2 + \vec{b}, \tag{2.8}$$

where n and m are integers, and $\vec{b} = \frac{a}{2}(1, \sqrt{3})$ is a vector that connects an atom in sublattice A to an atom in sublattice B within a unit cell. We can solve for the reciprocal lattice vectors using the condition $\vec{b}_j \cdot \vec{a}_i = 2\pi\delta_{i,j}$, which can be expressed in matrix form as:

$$\begin{pmatrix} b_{1x} & b_{1y} \\ b_{2x} & b_{2y} \end{pmatrix} \begin{pmatrix} a_{1x} & a_{2x} \\ a_{1y} & a_{2y} \end{pmatrix} = 2\pi \begin{pmatrix} 1 & 0 \\ 0 & 1 \end{pmatrix}. \tag{2.9}$$

Solving Eq. (2.9) yields the reciprocal vectors $\vec{b}_1 = \left(\frac{2\pi}{3a}, \frac{2\pi}{\sqrt{3}a}\right)$ and $\vec{b}_2 = \left(\frac{4\pi}{3a}, 0\right)$. Utilizing Bloch's theorem [78], the wavefunctions of an electron on sublattice A and B can be written as:

$$\psi^A_{\vec{k}}(\vec{r}) = \frac{1}{\sqrt{N}} \sum_{\vec{R}_A} e^{i\vec{k}\cdot\vec{R}_A} \phi_z(\vec{r} - \vec{R}_A), \tag{2.10a}$$

$$\psi^B_{\vec{k}}(\vec{r}) = \frac{1}{\sqrt{N}} \sum_{\vec{R}_B} e^{i\vec{k}\cdot\vec{R}_B} \phi_z(\vec{r} - \vec{R}_B), \tag{2.10b}$$

where $\phi_z(\vec{r} - \vec{R}_A)$ is a p_z orbital localized on an atom at position $\vec{R}_A$ and N is the total number of unit cells. The electron wavefunction can be written as a linear combination of the wavefunctions on sublattices A and B as:

$$\psi_{\vec{k}}(\vec{r}) = A_{\vec{k}}\psi^A_{\vec{k}}(\vec{r}) + B_{\vec{k}}\psi^B_{\vec{k}}(\vec{r}). \tag{2.11}$$

The Hamiltonian that describes our system is given by:

$$\hat{H} = \frac{p^2}{2m} + \sum_{\vec{R}_A} V(\vec{r} - \vec{R}_A) + \sum_{\vec{R}_B} V(\vec{r} - \vec{R}_B), \tag{2.12}$$

where the first term gives the kinetic energy of the electron while the second and third terms account for the interaction with the effective potential of atoms on sublattices A and B, respectively. We now write the Schrodinger equation:

$$\hat{H}\psi_{\vec{k}}(\vec{r}) = E_k \psi_{\vec{k}}(\vec{r}). \tag{2.13}$$

Using Eq. (2.11), we can write Eq. (2.13) as:

$$\hat{H}(A_{\vec{k}}\psi^A_{\vec{k}}(\vec{r}) + B_{\vec{k}}\psi^B_{\vec{k}}(\vec{r})) = E_k(A_{\vec{k}}\psi^A_{\vec{k}}(\vec{r}) + B_{\vec{k}}\psi^B_{\vec{k}}(\vec{r})), \tag{2.14}$$

or in Dirac notation:

$$\hat{H}(A_{\vec{k}}|\psi^A_{\vec{k}}\rangle + B_{\vec{k}}|\psi^B_{\vec{k}}\rangle) = E_k(A_{\vec{k}}|\psi^A_{\vec{k}}\rangle + B_{\vec{k}}|\psi^B_{\vec{k}}\rangle). \tag{2.15}$$

To build our Hamiltonian matrix, we first apply $\langle\psi^A_{\vec{k}}|$ to Eq. (2.15) which gives:

$$A_{\vec{k}}\langle\psi^A_{\vec{k}}|\hat{H}|\psi^A_{\vec{k}}\rangle + B_{\vec{k}}\langle\psi^A_{\vec{k}}|\hat{H}|\psi^B_{\vec{k}}\rangle = E_k A_{\vec{k}}, \tag{2.16}$$

where we have assumed that the wavefunctions on the sublattices are orthonormal. Similarly, we can apply $\langle\psi^B_{\vec{k}}|$ to Eq. (2.15) which gives:

$$A_{\vec{k}}\langle\psi^B_{\vec{k}}|\hat{H}|\psi^A_{\vec{k}}\rangle + B_{\vec{k}}\langle\psi^B_{\vec{k}}|\hat{H}|\psi^B_{\vec{k}}\rangle = E_k B_{\vec{k}}. \tag{2.17}$$

Combining Eq. (2.16) and Eq. (2.17) gives an eigenvalue equation:

$$\begin{pmatrix} \langle\psi^A_{\vec{k}}|\hat{H}|\psi^A_{\vec{k}}\rangle & \langle\psi^A_{\vec{k}}|\hat{H}|\psi^B_{\vec{k}}\rangle \\ \langle\psi^B_{\vec{k}}|\hat{H}|\psi^A_{\vec{k}}\rangle & \langle\psi^B_{\vec{k}}|\hat{H}|\psi^B_{\vec{k}}\rangle \end{pmatrix} \begin{pmatrix} A_{\vec{k}} \\ B_{\vec{k}} \end{pmatrix} = E_{\vec{k}} \begin{pmatrix} A_{\vec{k}} \\ B_{\vec{k}} \end{pmatrix}. \tag{2.18}$$

We first begin by computing the element $\langle\psi^A_{\vec{k}}|\hat{H}|\psi^A_{\vec{k}}\rangle$, where we expand it using Eq. (2.12) as:

$$\langle\psi^A_{\vec{k}}|\hat{H}|\psi^A_{\vec{k}}\rangle = \langle\psi^A_{\vec{k}}|\frac{p^2}{2m} + \sum_{\vec{R}_A} V(\vec{r}-\vec{R}_A)|\psi^A_{\vec{k}}\rangle + \langle\psi^A_{\vec{k}}|\sum_{\vec{R}_B} V(\vec{r}-\vec{R}_B)|\psi^A_{\vec{k}}\rangle. \tag{2.19}$$

We can expand the first term in Eq. (2.19) as:

$$\langle\psi^A_{\vec{k}}|\frac{p^2}{2m} + \sum_{\vec{R}_A} V(\vec{r}-\vec{R}_A)|\psi^A_{\vec{k}}\rangle = \frac{1}{N}\sum_{\vec{R}_A,\vec{R}'_A} e^{i\vec{k}\cdot(\vec{R}_A-\vec{R}'_A)}\int d\vec{r}\phi^*_z(\vec{r}-\vec{R}'_A)\frac{p^2}{2m}\phi_z(\vec{r}-\vec{R}_A) \tag{2.20}$$

$$+\frac{1}{N}\sum_{\vec{R}_A,\vec{R}'_A,\vec{R}''_A} e^{i\vec{k}\cdot(\vec{R}_A-\vec{R}'_A)}\int d\vec{r}\phi^*_z(\vec{r}-\vec{R}'_A)V(\vec{r}-\vec{R}''_A)\phi_z(\vec{r}-\vec{R}_A).$$

In the NN approximation, the terms that contribute involve $\vec{R}_A = \vec{R}'_A$ and $\vec{R}_A = \vec{R}'_A = \vec{R}''_A$ in the first and second terms of Eq. (2.20), respectively. This gives:

$$\langle\psi^A_{\vec{k}}|\frac{p^2}{2m} + \sum_{\vec{R}_A} V(\vec{r}-\vec{R}_A)|\psi^A_{\vec{k}}\rangle = \int d\vec{r}\phi^*_z(\vec{r}-\vec{R}_A)\frac{p^2}{2m}\phi_z(\vec{r}-\vec{R}_A) \tag{2.21}$$

$$+\int d\vec{r}\phi^*_z(\vec{r}-\vec{R}_A)V(\vec{r}-\vec{R}_A)\phi_z(\vec{r}-\vec{R}_A). \tag{2.22}$$

The Slater orbitals fulfill Eq. (2.2), resulting in:

$$\langle\psi^A_{\vec{k}}|\frac{p^2}{2m} + \sum_{\vec{R}_A} V(\vec{r}-\vec{R}_A)|\psi^A_{\vec{k}}\rangle \approx \epsilon_A, \tag{2.23}$$

where ϵ_A is the onsite energy of sublattice A. The second term in Eq. (2.19) can be expanded as:

$$\langle\psi^A_{\vec{k}}|\sum_{\vec{R}_B} V(\vec{r}-\vec{R}_B)|\psi^A_{\vec{k}}\rangle = \frac{1}{N}\sum_{\vec{R}_A,\vec{R}'_A,\vec{R}_B} e^{i\vec{k}\cdot(\vec{R}_A-\vec{R}'_A)}\int d\vec{r}\phi^*_z(\vec{r}-\vec{R}'_A)V(\vec{r}-\vec{R}_B)\phi_z(\vec{r}-\vec{R}_A), \tag{2.24}$$

which consists of three center integrals. It describes the hopping of an electron on an atom from sublattice A to another atom on sublattice A while feeling the potential from atoms on sublattice B. Since atoms on sublattice A are next NN with each other, this term can be neglected in the NN approximation. Therefore we have:

$$\langle \psi_{\vec{k}}^{A} | \hat{H} | \psi_{\vec{k}}^{A} \rangle = \epsilon_A. \tag{2.25}$$

Similarly, for the other diagonal matrix element of Eq. (2.18):

$$\langle \psi_{\vec{k}}^{B} | \hat{H} | \psi_{\vec{k}}^{B} \rangle = \epsilon_B, \tag{2.26}$$

where we take $\epsilon_A = \epsilon_B = \epsilon$ as there should be no difference in the onsite energy between those of atoms in sublattice A and B. Next, we compute the off-diagonal elements of Eq. (2.18) beginning with $\langle \psi_{\vec{k}}^{B} | \hat{H} | \psi_{\vec{k}}^{A} \rangle$:

$$\begin{aligned}
\langle \psi_{\vec{k}}^{B} | \hat{H} | \psi_{\vec{k}}^{A} \rangle &= \langle \psi_{\vec{k}}^{B} | \frac{p^2}{2m} + \sum_{\vec{R}_A} V(\vec{r} - \vec{R}_A) | \psi_{\vec{k}}^{A} \rangle + \langle \psi_{\vec{k}}^{B} | \sum_{\vec{R}_B} V(\vec{r} - \vec{R}_B) | \psi_{\vec{k}}^{A} \rangle \\
&= \epsilon \langle \psi_{\vec{k}}^{B} | \psi_{\vec{k}}^{A} \rangle + \frac{1}{N} \sum_{\vec{R}_A, \vec{R}_B, \vec{R'}_B} e^{i\vec{k}\cdot(\vec{R}_A - \vec{R}_B)} \int d\vec{r} \phi_z^*(\vec{r} - \vec{R}_B) V(\vec{r} - \vec{R'}_B) \phi_z(\vec{r} - \vec{R}_A) \\
&= \frac{1}{N} \sum_{\langle \vec{R}_A, \vec{R}_B \rangle} e^{i\vec{k}\cdot(\vec{R}_A - \vec{R}_B)} \int d\vec{r} \phi_z^*(\vec{r} - \vec{R}_B) V(\vec{r} - \vec{R}_B) \phi_z(\vec{r} - \vec{R}_A),
\end{aligned} \tag{2.27}$$

where we have neglected three center integrals ($\vec{R}_B \neq \vec{R'}_B$) and, in the last step, have restricted our summation over NN. The summation will run over all atoms in sublattice A, and for each of these atoms, the corresponding three NN in sublattice B, as shown in Fig. 2.1. We can define the hopping integral for NNs as:

$$t = \int d\vec{r} \phi_z^*(\vec{r} - \vec{R}_B) V(\vec{r} - \vec{R}_B) \phi_z(\vec{r} - \vec{R}_A), \tag{2.28}$$

which allows us to write Eq. (2.27) as:

$$\begin{aligned}\langle\psi^B_{\vec{k}}|\hat{H}|\psi^A_{\vec{k}}\rangle &= \frac{t}{N}\sum_{\langle\vec{R}_A,\vec{R}_B\rangle} e^{i\vec{k}\cdot(\vec{R}_A-\vec{R}_B)} \\ &= \frac{t}{N}\cdot N(e^{i\vec{k}\cdot\vec{\delta}_1}+e^{i\vec{k}\cdot\vec{\delta}_2}+e^{i\vec{k}\cdot\vec{\delta}_3}) \\ &= te^{i\vec{k}\cdot\vec{b}}(1+e^{-i\vec{k}\cdot\vec{a}_1}+e^{-i\vec{k}\cdot(\vec{a}_2+\vec{a}_1)}).\end{aligned} \tag{2.29}$$

The NN vectors $\vec{\delta}_1, \vec{\delta}_2$ and $\vec{\delta}_3$ are given by:

$$\vec{\delta}_1 = \vec{b}, \tag{2.30a}$$

$$\vec{\delta}_2 = \vec{b} - \vec{a}_1, \tag{2.30b}$$

$$\vec{\delta}_3 = \vec{b} - \vec{a}_2 - \vec{a}_1. \tag{2.30c}$$

If we define $f(\vec{k}) = e^{i\vec{k}\cdot\vec{b}}(1+e^{-i\vec{k}\cdot\vec{a}_1}+e^{-i\vec{k}\cdot(\vec{a}_2+\vec{a}_1)})$ and take $\epsilon = 0$ which is just a shift in the energy, Eq. (2.18) becomes:

$$\begin{pmatrix} 0 & tf(\vec{k}) \\ tf^*(\vec{k}) & 0 \end{pmatrix}\begin{pmatrix} A_{\vec{k}} \\ B_{\vec{k}} \end{pmatrix} = E_{\vec{k}}\begin{pmatrix} A_{\vec{k}} \\ B_{\vec{k}} \end{pmatrix}. \tag{2.31}$$

Diagonalizing the Hamiltonian in Eq. (2.31) results in energies given by:

$$E^{\pm}_{\vec{k}} = \pm t|f(\vec{k})|, \tag{2.32}$$

where the positive and negative energies correspond to the conduction and valence bands, respectively. The resulting band structure is presented in Fig. 2.2. The valence (blue) and conduction (red) bands touch at certain points in the Brillouin zone, specifically at the K and K' points. Since there is no energy gap between the valence and conduction bands, graphene is a semimetal.

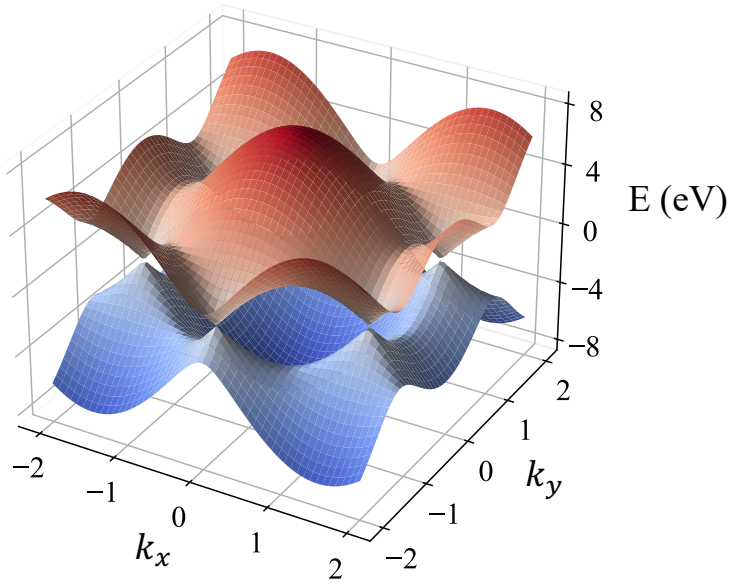

Figure 2.2: The band structure of monolayer graphene in the NN approximation with conduction band (red) and valence band (blue). The hopping element t is set to -2.8 eV.

2.1.2 Tight-binding model for bulk bilayer graphene

In this section, we will extend our tight-binding model to bilayer graphene. In particular, we will focus on Bernal-stacked bilayer graphene [79], as shown in Fig. 2.3. We begin by writing the wavefunction for our lattice as a linear combination of the wavefunctions on sublattices A_1, B_1, A_2 and B_2 as:

$$\psi_{\vec{k}}(\vec{r}) = A^1_{\vec{k}}\psi^{A_1}_{\vec{k}}(\vec{r}) + B^1_{\vec{k}}\psi^{B_1}_{\vec{k}}(\vec{r}) + A^2_{\vec{k}}\psi^{A_2}_{\vec{k}}(\vec{r}) + B^2_{\vec{k}}\psi^{B_2}_{\vec{k}}(\vec{r}), \tag{2.33}$$

where the wavefunction of each of the four sublattices can be expressed in the same form using Bloch's theorem as in Eq. (2.10). The Hamiltonian describing our bilayer graphene system is similar to that of Eq. (2.12) but extended for four sublattices:

$$\hat{H} = \frac{p^2}{2m} + \sum_{\vec{R}_{A_1}} V(\vec{r} - \vec{R}_{A_1}) + \sum_{\vec{R}_{B_1}} V(\vec{r} - \vec{R}_{B_1}) + \sum_{\vec{R}_{A_2}} V(\vec{r} - \vec{R}_{A_2}) + \sum_{\vec{R}_{B_2}} V(\vec{r} - \vec{R}_{B_2}). \tag{2.34}$$

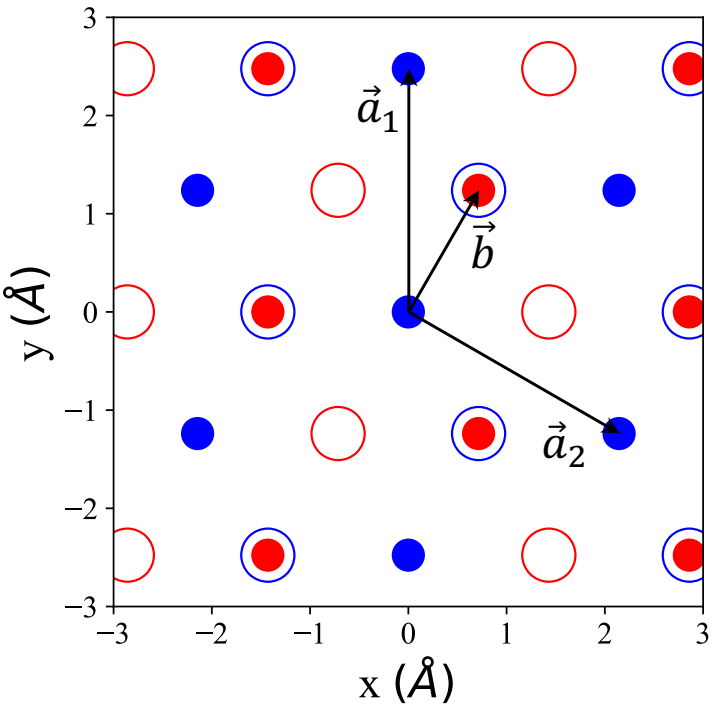

Figure 2.3: Structure of Bernal-stacked bilayer graphene with atoms on sublattice A (blue) and B (red). The solid circles represent atoms on the bottom layer and the open circles are atoms on the top layer. The primitive unit cell vectors $\vec{a}_1$ and $\vec{a}_2$, and the nearest neighbour vector $\vec{b}$ are also illustrated.

We can now construct the Schrodinger equation and solve for each element of the 4×4 matrix as was done in the previous section for monolayer graphene, and we will obtain [12, 80–82]:

$$H_{\text{bulk}}(\vec{k}) = \begin{pmatrix} 0 & \gamma_0 f(\vec{k}) & \gamma_4 f(\vec{k}) & \gamma_3 f^*(\vec{k}) \\ \gamma_0 f^*(\vec{k}) & 0 & \gamma_1 & \gamma_4 f(\vec{k}) \\ \gamma_4 f^*(\vec{k}) & \gamma_1 & 0 & \gamma_0 f(\vec{k}) \\ \gamma_3 f(\vec{k}) & \gamma_4 f^*(\vec{k}) & \gamma_0 f^*(\vec{k}) & 0 \end{pmatrix}, \tag{2.35}$$

where the parameter $\gamma_0 = -2.5$ eV represents the NN intralayer hopping and $\gamma_1 = 0.34$ eV denotes the interlayer hopping between pairs of orbitals on sublattices B_1 and A_2 [60].

These values for γ_0 and γ_1 were determined through fitting tight-binding parameters to ab initio density functional theory calculations of the BLG band structure [65]. The parameters γ_3 and γ_4 describe the next NN interlayer hopping. The inclusion of γ_3 introduces the effects of TW, and we will study its effects in great detail in Chapter 4. For now, we neglect the effects of γ_3 and γ_4 and our Hamiltonian simplifies to:

$$H_{\text{bulk}}(\vec{k}) = \begin{pmatrix} 0 & \gamma_0 f(\vec{k}) & 0 & 0 \\ \gamma_0 f^*(\vec{k}) & 0 & \gamma_1 & 0 \\ 0 & \gamma_1 & 0 & \gamma_0 f(\vec{k}) \\ 0 & 0 & \gamma_0 f^*(\vec{k}) & 0 \end{pmatrix}. \tag{2.36}$$

Taking a path between the K and K' points and passing through the Γ point, as depicted in Fig. 3.1(b), we can diagonalize the 4×4 Hamiltonian given in Eq. (2.36) for each k-point to obtain the band structure presented in Fig. 2.4(a). The valence and conduction bands

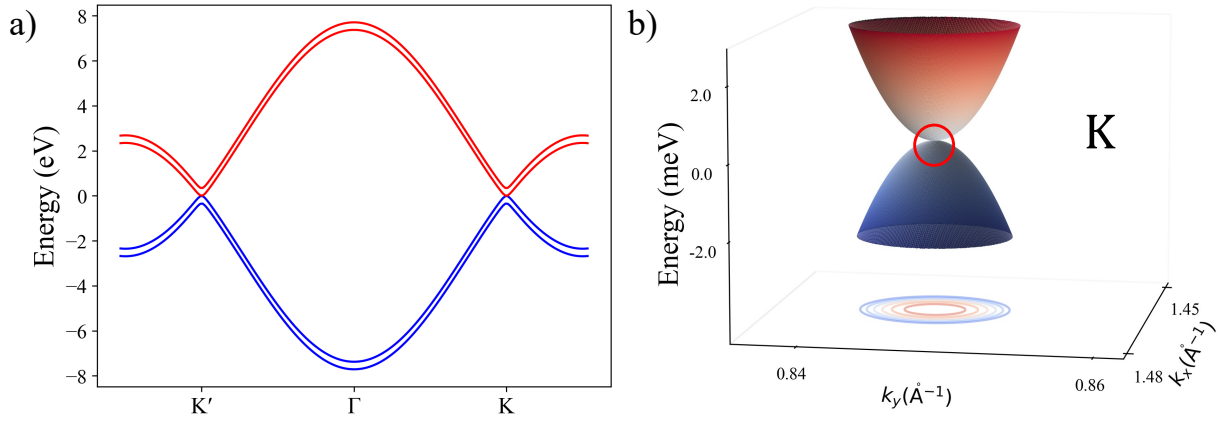

Figure 2.4: The band structure of bilayer graphene neglecting γ_3 and γ_4 with conduction band (red) and valence band (blue) (a) along the path from K' to K passing through Γ (b) zoomed in around K point.

touch at the K and K' points, resulting in a zero energy gap, making BLG a semimetal, as was the case with monolayer graphene. Fig. 2.4(b) depicts a 3D zoom around the K point, revealing parabolic dispersion, which differs from the linear dispersion found in monolayer

graphene. To open an energy gap, we apply an external electric field perpendicular to the layers, resulting in a potential of $V_E/2$ ($-V_E/2$) on the bottom (top) layer and an overall potential difference between layers of $V_E = 380$ meV. The resulting Hamiltonian is given by:

$$H_{\text{bulk}}(\vec{k}) = \begin{pmatrix} \frac{V_E}{2} & \gamma_0 f(\vec{k}) & 0 & 0 \\ \gamma_0 f^*(\vec{k}) & \frac{V_E}{2} & \gamma_1 & 0 \\ 0 & \gamma_1 & -\frac{V_E}{2} & \gamma_0 f(\vec{k}) \\ 0 & 0 & \gamma_0 f^*(\vec{k}) & -\frac{V_E}{2} \end{pmatrix}. \tag{2.37}$$

After diagonalizing the Hamiltonian given above near the K point, we have an energy gap opening, as shown in Fig. 2.5. The energy difference between the lowest conduction band (CB) and highest valence band (VB) equals the displacement voltage V_E at the K point. In Chapter 3, we will revisit this gated bilayer graphene Hamiltonian and consider a QD with a Gaussian-shaped potential profile. This potential profile will allow for the confinement of electrons and holes on different layers of the bilayer graphene structure.

2.2 Configuration interaction method

In this section, I will briefly outline the configuration interaction (CI) method, also known as exact diagonalization. This method allows for an accurate description of the effects of electron-electron interactions and is particularly useful for studying excitations where an electron is promoted to the CB, leaving behind a hole in the VB, thereby forming an exciton. Consider the many-electron Hamiltonian, written in the basis of single-particle QD states given by:

$$\hat{H}_{\text{MB}} = \sum_{p,\sigma} E_p c^\dagger_{p,\sigma} c_{p,\sigma} + \frac{1}{2} \sum_{p,q,r,s} \sum_{\sigma,\sigma'} \langle p, q|V_C|r, s\rangle \, c^\dagger_{p,\sigma} c^\dagger_{q,\sigma'} c_{r,\sigma'} c_{s,\sigma} - \sum_{p,s,\sigma} V^P_{p,s} c^\dagger_{p,\sigma} c_{s,\sigma}, \tag{2.38}$$

where the operators $c^\dagger_{p,\sigma}$ ($c_{p,\sigma}$) create (annihilate) an electron in a QD state p with spin σ. The summation indices in Eq. (2.38) run over all QD states and spin up and down. The first term, $E_{p,\sigma}$, represents the single-particle QD energies and the second term accounts for

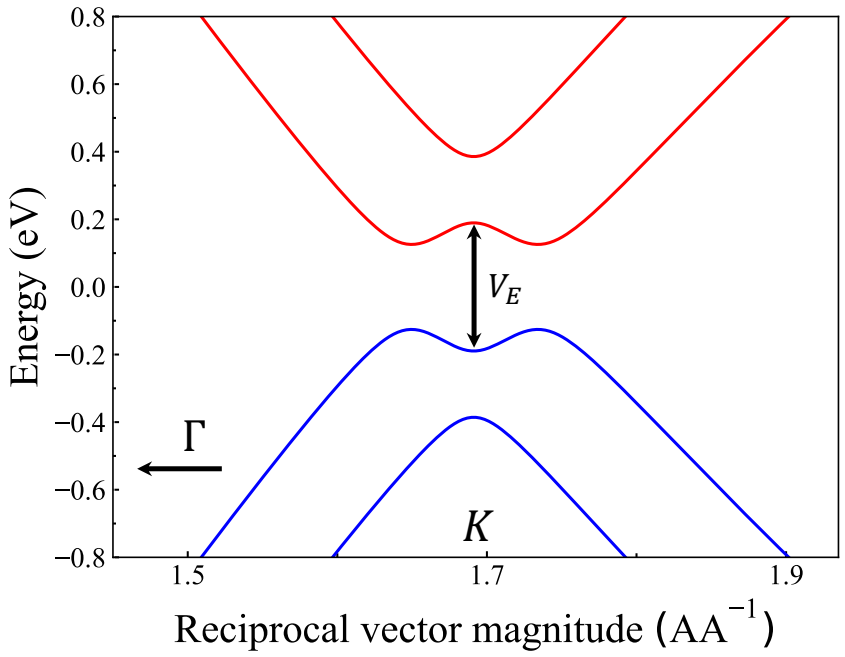

Figure 2.5: The band edges of gated bilayer graphene along the path $\Gamma - K$ around the K point with a displacement voltage of $V_E = 380$ meV, $\gamma_0 = -2.5$ eV and $\gamma_1 = 0.34$ eV, neglecting trigonal warping effects.

the electron-electron interactions with potential $V_C = \frac{e^2}{4\pi\epsilon_0\kappa|\vec{r}_1-\vec{r}_2|}$, where ϵ_0 is the vacuum permittivity and κ is the dielectric constant and is taken as $\kappa = 6$ [3, 65]. The explicit expression for the Coulomb matrix elements $\langle p, q|V_C|r, s\rangle$ is given by:

$$\langle p, q|V_C|r, s\rangle = \iint d\vec{r}_1\, d\vec{r}_2\, \varphi_p^*(\vec{r}_1)\varphi_q^*(\vec{r}_2)\varphi_r(\vec{r}_2)\varphi_s(\vec{r}_1)\frac{e^2}{4\pi\epsilon_0\kappa|\vec{r}_1 - \vec{r}_2|}. \tag{2.39}$$

The Coulomb matrix elements in the above equation can be written in terms of Slater-like p_z orbitals and computed numerically; this will be explained in more detail in a subsequent section of this chapter. In the last term, we consider a positive charge background to

maintain charge neutrality of the system and model it as:

$$V^P_{n_1,n_2} = \sum_{n}^{N_{occ}} \langle n_1, n|V_C|n, n_2\rangle \,. \tag{2.40}$$

We assume that the positive charges occupy orbitals identical to those of electrons and have the same distribution as the electrons in a filled VB. To diagonalize the many-body Hamiltonian in Eq. (2.38), we write the wavefunction as a linear combination of Slater determinants $|S\rangle$:

$$|\Psi\rangle = \sum_{s} A_s \,|S\rangle \,, \tag{2.41}$$

where $|S\rangle$ is a configuration that can expressed as:

$$|S\rangle = \prod_{i=1}^{L} (c^\dagger_{i,\uparrow})^{\alpha_{i,\uparrow}} \prod_{i=1}^{L} (c^\dagger_{i,\downarrow})^{\alpha_{i,\downarrow}} |0\rangle, \tag{2.42}$$

where L is the number of QD states, $|0\rangle$ represents the vacuum state, and $\alpha_i = 0, 1$, indicating whether the state is unoccupied (0) or occupied (1). When including all possible configurations, the Hamiltonian can be diagonalized exactly. However, the basis size grows rapidly with the number of VB and CB QD states and becomes computationally expensive quickly. In the next section, we will restrict our configurations to one-pair excitations from the ground state, that is:

$$|q, p, \sigma\rangle = c^\dagger_{q,\sigma} c_{p,\sigma} \,|GS\rangle \,, \tag{2.43}$$

where an electron is removed from the VB state p with spin σ, and excited to a CB state q with the same spin and the many-electron ground state is defined as:

$$|GS\rangle = \prod_{i \in VB} c^\dagger_{i,\uparrow} \prod_{i \in VB} c^\dagger_{i,\downarrow} |0\rangle, \tag{2.44}$$

which corresponds to a fully occupied VB. To translate the configuration given in Eq. (2.42) into something that can be coded, we can create an array and organize our states with

spin up on the left and spin down on the right as:

$$|S\rangle = |\alpha_{1,\uparrow}\alpha_{2,\uparrow}...\alpha_{j,\uparrow}...\alpha_{L,\uparrow};\alpha_{1,\downarrow}\alpha_{2,\downarrow}...\alpha_{j,\downarrow}...\alpha_{L,\downarrow}\rangle. \tag{2.45}$$

It is important that we maintain consistency and organize the spin up creation operators on the left and spin down creation operators on the right. Let's now consider the action of a creation operator on the general state $|S\rangle$ given in Eq. (2.42):

$$c^\dagger_{j,\sigma}|S\rangle = c^\dagger_{j,\sigma}\prod_{i=1}^{L}(c^\dagger_{i,\uparrow})^{\alpha_{i,\uparrow}}\prod_{i=1}^{L}(c^\dagger_{i,\downarrow})^{\alpha_{i,\downarrow}}|0\rangle. \tag{2.46}$$

Consider the case where $\sigma =\downarrow$, then Eq. (2.46) becomes:

$$\begin{aligned}
c^\dagger_{j,\downarrow}\prod_{i=1}^{L}(c^\dagger_{i,\uparrow})^{\alpha_{i,\uparrow}}\prod_{i=1}^{L}(c^\dagger_{i,\downarrow})^{\alpha_{i,\downarrow}}|0\rangle &= (-1)^{\sum_{i=1}^{L}\alpha_{i,\uparrow}}\prod_{i=1}^{L}(c^\dagger_{i,\uparrow})^{\alpha_{i,\uparrow}}c^\dagger_{j,\downarrow}\prod_{i=1}^{L}(c^\dagger_{i,\downarrow})^{\alpha_{i,\downarrow}}|0\rangle \\
&= (-1)^{\sum_{i=1}^{L}\alpha_{i,\uparrow}}\prod_{i=1}^{L}(c^\dagger_{i,\uparrow})^{\alpha_{i,\uparrow}}(-1)^{\sum_{i=1}^{j-1}\alpha_{i,\downarrow}}\prod_{i=1}^{j-1}(c^\dagger_{i,\downarrow})^{\alpha_{i,\downarrow}}c^\dagger_{j,\downarrow}(c^\dagger_{j,\downarrow})^{\alpha_{j,\downarrow}}\prod_{i=j+1}^{L}(c^\dagger_{i,\downarrow})^{\alpha_{i,\downarrow}}|0\rangle \\
&= (-1)^{\sum_{i=1}^{L}\alpha_{i,\uparrow}}(-1)^{\sum_{i=1}^{j-1}\alpha_{i,\downarrow}}\prod_{i=1}^{L}(c^\dagger_{i,\uparrow})^{\alpha_{i,\uparrow}}\prod_{i=1}^{j-1}(c^\dagger_{i,\downarrow})^{\alpha_{i,\downarrow}}c^\dagger_{j,\downarrow}(1-\alpha_{j,\downarrow})\prod_{i=j+1}^{L}(c^\dagger_{i,\downarrow})^{\alpha_{i,\downarrow}}|0\rangle \\
= (1-\alpha_{j,\downarrow})(-1)^{\sum_{i=1}^{L}\alpha_{i,\uparrow}}(-1)^{\sum_{i=1}^{j-1}\alpha_{i,\downarrow}}&|\alpha_{1,\uparrow}...\alpha_{j,\uparrow}...\alpha_{L,\uparrow};\alpha_{1,\downarrow}...\alpha_{j-1,\downarrow},1,\alpha_{j+1,\downarrow}...\alpha_{L,\downarrow}\rangle.
\end{aligned} \tag{2.47}$$

If we had considered the case where $\sigma =\uparrow$ in Eq. (2.46), we would obtain a simpler expression given by:

$$c^\dagger_{j,\uparrow}|S\rangle = (1-\alpha_{j,\uparrow})(-1)^{\sum_{i=1}^{j-1}\alpha_{i,\uparrow}}|\alpha_{1,\uparrow}...\alpha_{j-1,\uparrow},1,\alpha_{j+1,\uparrow}...\alpha_{L,\uparrow};\alpha_{1,\downarrow}...\alpha_{j,\downarrow}...\alpha_{L,\downarrow}\rangle. \tag{2.48}$$

Similarly, for the annihilation operator acting on $|S\rangle$ one can show that:

$$c_{j,\downarrow}|S\rangle = \alpha_{j,\downarrow}(-1)^{\sum_{i=1}^{L}\alpha_{i,\uparrow}}(-1)^{\sum_{i=1}^{j-1}\alpha_{i,\downarrow}}|\alpha_{1,\uparrow}...\alpha_{j,\uparrow}...\alpha_{L,\uparrow};\alpha_{1,\downarrow}...\alpha_{j-1,\downarrow},0,\alpha_{j+1,\downarrow}...\alpha_{L,\downarrow}\rangle, \tag{2.49a}$$

$$c_{j,\uparrow}|S\rangle = \alpha_{j,\uparrow}(-1)^{\sum_{i=1}^{j-1}\alpha_{i,\uparrow}}|\alpha_{1,\uparrow}...\alpha_{j-1,\uparrow},0,\alpha_{j+1,\uparrow}...\alpha_{L,\uparrow};\alpha_{1,\downarrow}...\alpha_{j,\downarrow}...\alpha_{L,\downarrow}\rangle. \tag{2.49b}$$

Eqs. (2.47), (2.48), and (2.49) can be used to code functions for the creation operators that act on arrays corresponding to configurations. In this way, we can apply the many-electron Hamiltonian given in Eq. (2.38) on each basis states and construct the Hamiltonian matrix elements in the basis of configurations. Next, we can diagonalize this Hamiltonian to obtain the energy spectrum and wavefunctions. It is essential to ensure that the chosen basis of configurations is sufficiently large to describe the energy region of interest while ensuring that the Hilbert space is not so large that it introduces computational challenges. An explicit example of this CI method is provided in the next chapter, where we derive the BSE, which will be used to study excitons.

2.3 Bethe-Salpeter equation

In this section, we will derive the BSE, which we will use to obtain the exciton energy spectrum and wavefunctions. I would like to note that I am following a derivation of Ref. 65. First, consider a system such that the ground state can be written as a single Slater determinant, with a fully occupied VB defined by:

$$|GS\rangle = \prod_{p,\sigma}^{N_{occ}} c^{\dagger}_{p,\sigma} \ |0\rangle \,, \tag{2.50}$$

where the operators $c^{\dagger}_{p,\sigma}$ ($c_{p,\sigma}$) create (annihilate) an electron in a QD state p with spin σ. The index p runs over the occupied VB states and N_{occ} is the number of states that are occupied. We can write our exciton wavefunction as a linear combination of electron-hole pair excitations that conserve S_z:

$$|\Psi^{\mu}\rangle = \sum_{p,q,\sigma} A^{\mu}_{p,q,\sigma} c^{\dagger}_{q,\sigma} c_{p,\sigma} \, |GS\rangle \,. \tag{2.51}$$

Here, μ indexes the exciton states and the index p runs over all VB states, while q covers all CB states. The amplitudes $A^{\mu}_{p,q,\sigma}$ can be obtained by solving the BSE equation, which we will now derive. We begin with the many-electron Hamiltonian written in the

basis of single-particle QD states given by:

$$\hat{H}_{\mathrm{MB}} = \sum_{p,\sigma} E_p c^\dagger_{p,\sigma} c_{p,\sigma} + \frac{1}{2} \sum_{p,q,r,s} \sum_{\sigma,\sigma'} \langle p,q|V_C|r,s\rangle \, c^\dagger_{p,\sigma} c^\dagger_{q,\sigma'} c_{r,\sigma'} c_{s,\sigma} - \sum_{p,s,\sigma} V^P_{p,s} c^\dagger_{p,\sigma} c_{s,\sigma}, \tag{2.52}$$

where the summation indices run over all QD states as well as spin up and down. We can write this many-electron Hamiltonian in a more compact notation with indices consisting of single-particle QD state and spin:

$$\begin{aligned} \hat{H}_{\mathrm{MB}} =& \sum_{n} E_n c^\dagger_n c_n + \frac{1}{2} \sum_{n_1,n_2,n_3,n_4} \langle n_1,n_2|V_C|n_3,n_4\rangle \, c^\dagger_{n_1} c^\dagger_{n_2} c_{n_3} c_{n_4} - \sum_{n_1,n_2} V^P_{n_1 n_2} c^\dagger_{n_1} c_{n_2} \\ =& \hat{H}_1 + \hat{H}_2 - \hat{H}_3 \end{aligned} \tag{2.53}$$

The exciton wavefunction in Eq. (2.51) written in compact notation becomes:

$$|\Psi^\mu\rangle = \sum_{a,b} A^\mu_{a,b} c^\dagger_b c_a \, |GS\rangle = \sum_s A^\mu_s \, |X_s\rangle \, . \tag{2.54}$$

Acting the many-electron Hamiltonian in Eq. (2.53) on the exciton wavefunction in Eq. (2.54) and utilizing the Schrodinger equation, we obtain:

$$\hat{H}_{MB} \, |\Psi^\mu\rangle = E_\mu \, |\Psi^\mu\rangle \tag{2.55}$$

Acting $\langle \Psi^{\mu'}|$ to the above equation gives:

$$\sum_{s_1} A^\mu_{s_1} \langle X_{s_2}|\hat{H}_1 + \hat{H}_2 - \hat{H}_3|X_{s_1}\rangle = E_\mu A^\mu_{s_2}. \tag{2.56}$$

We first compute the single-particle term:

$$\langle X_{s_2}|\hat{H}_1|X_{s1}\rangle = \sum_n E_n \langle GS|c^\dagger_{a_2} c_{b_2} c^\dagger_n c_n c^\dagger_{b_1} c_{a_1} \, |GS\rangle \, . \tag{2.57}$$

To compute the expectation value of the above can be very long and tedious, but we can

use Wick's theorem [83] to help evaluate these expectation values, which gives:

$$\langle GS|c^\dagger_{a_2}c_{b_2}c^\dagger_n c_n c^\dagger_{b_1}c_{a_1}\,|GS\rangle = \delta_{a_2,n}\langle GS|c_{b_2}c^\dagger_n c^\dagger_{b_1}c_{a_1}\,|GS\rangle + \delta_{a_2,a_1}\langle GS|c_{b_2}c^\dagger_n c_n c^\dagger_{b_1}\,|GS\rangle\,, \quad (2.58)$$

where we have used the fact that a_1 and a_2 are from the VB and b_1 and b_2 are from the CB, so we cannot have $a = b$. In a similar way we can solve for the terms $\langle GS|c_{b_2}c^\dagger_n c^\dagger_{b_1}c_{a_1}\,|GS\rangle$ and $\langle GS|c_{b_2}c^\dagger_n c_n c^\dagger_{b_1}\,|GS\rangle$:

$$\langle GS|c_{b_2}c^\dagger_n c^\dagger_{b_1}c_{a_1}|GS\rangle = -\langle GS|c_{b_2}c^\dagger_{b_1}|GS\rangle\left\langle GS\left|c^\dagger_n c_{a_1}\right|GS\right\rangle = -\delta_{b_2,b_1}\delta_{n,a_1}. \quad (2.59)$$

And:

$$\langle GS|c_{b_2}c^\dagger_n c_n c^\dagger_{b_1}|GS\rangle = \delta_{b_2,n}\delta_{n,b_1} + \delta_{b_2,b_1}\delta_{n\leq N_{occ}}, \quad (2.60)$$

where the condition on $\delta_{n\leq N_{occ}}$ is used to ensure that the state n corresponds to an occupied VB state. Bringing everything together in Eq. (2.59) and Eq. (2.60) gives:

$$\langle GS|c^\dagger_{a_2}c_{b_2}c^\dagger_n c_n c^\dagger_{b_1}c_{a_1}\,|GS\rangle = -\delta_{a_2,n}\delta_{b_2,b_1}\delta_{n,a_1} + \delta_{a_2,a_1}\delta_{b_2,n}\delta_{n,b_1} + \delta_{a_2,a_1}\delta_{b_2,b_1}\delta_{n\leq N_{occ}}, \quad (2.61)$$

Substituting the above into Eq. (2.57) results in the following:

$$\begin{aligned}\langle X_{s_2}|\hat{H}_1|X_{s_1}\rangle &= \sum_n E_n(-\delta_{a_2,n}\delta_{b_2,b_1}\delta_{n,a_1} + \delta_{a_2,a_1}\delta_{b_2,n}\delta_{n,b_1} + \delta_{a_2,a_1}\delta_{b_2,b_1}\delta_{n\leq N_{occ}}) \\ &= \delta_{a_1,a_2}\delta_{b_2,b_1}\left(E_{b_1} - E_{a_1} + \sum_n^{N_{occ}} E_n\right).\end{aligned} \quad (2.62)$$

Next, we compute the Coulomb term:

$$\langle X_{s_2}|\hat{H}_2|X_{s1}\rangle = \frac{1}{2}\sum_{n_1,n_2,n_3,n_4}\langle n_1,n_2|V_C\,|n_3,n_4\rangle\,\langle GS|c^\dagger_{a_2}c_{b_2}c^\dagger_{n_1}c^\dagger_{n_2}c_{n_3}c_{n_4}c^\dagger_{b_1}c_{a_1}\,|GS\rangle. \quad (2.63)$$

Following similar algebra as was done for the single-particle term and using Wick's theorem,

we obtain:

$$\begin{aligned}\langle X_{s_2}|\hat{H}_2|X_{s_1}\rangle &= \langle a_1, b_2|V_C|\, a_2, b_1\rangle - \langle a_1, b_2|V_C|\, b_1, a_2\rangle \\ &\quad - \delta_{b_1,b_2}\sum_{n}^{N_{\rm occ}}[\langle\ a_1, n\,|V_C|n, a_2\rangle - \langle n, a_1\,|V_C|\, n, a_2\rangle] \\ &\quad + \delta_{a_1,a_2}\sum_{n}^{N_{\rm occ}}[\langle\ b_2, n\,|V_C|\, n, b_1\rangle - \langle n, b_2\,|V_C|\, n, b_1\ \rangle] \\ &\quad + \delta_{a_1,a_2}\delta_{b_1,b_2}\sum_{n<n_1}^{N_{\rm occ}}[\langle\ n_1, n\,|V_C|\, n, n_1\rangle - \langle n_1, n\,|V_C|\, n_1, n\rangle]\,.\end{aligned} \tag{2.64}$$

Lastly, we have the positive background term, which is given by:

$$\begin{aligned}\langle X_{s_2}|\hat{H}_3|X_{s_1}\rangle &= \delta_{b_1,b_2}\sum_{n}^{N_{\rm occ}}\langle a_1, n\,|V_C|\, n, a_2\rangle + \delta_{a_1,a_2}\sum_{n}^{N_{\rm occ}}\langle b_2, n\,|V_C|\, n, b_1\rangle \\ &\quad + \delta_{a_1,a_2}\delta_{b_1,b_2}\sum_{n,n_1}^{N_{\rm occ}}\langle n_1, n\,|V_C|\, n, n_1\rangle.\end{aligned} \tag{2.65}$$

The first two terms describe the scattering of a hole in the VB and an electron in the CB given by the interaction with the positive background, respectively, while the third term represents the interaction of the filled VB with the background. We want to measure the energy of an exciton relative to the energy of the ground state, and so we must first compute the ground state energy. The energy of the ground state can be found as follows:

$$\langle GS|\hat{H}_{MB}|GS\rangle = \sum_{n}^{N_{occ}} E_n + \sum_{n<n_1}^{N_{occ}}[\langle n_1, n|\, V_C\,|n, n_1\rangle - \langle n_1, n|\, V_C\,|n_1, n\rangle] - \sum_{n,n_1}\langle n_1, n|\, V_C\,|n, n_1\rangle\,. \tag{2.66}$$

We can now subtract the ground state energy found in Eq. (2.66) from the energy of our

exciton to obtain the energy of the exciton relative to the ground state:

$$\begin{aligned}\langle X_{s_2}|\hat{H}|X_{s_1}\rangle - \delta_{s_2,s_1}\langle GS|\hat{H}_{MB}|GS\rangle = \delta_{a_1,a_2}\delta_{b_2,b_1}\left[E_{b_1} - E_{a_1}\right] + \langle a_1, b_2\left|V_C\right|a_2, b_1\rangle \\ - \langle a_1, b_2\left|V_C\right|b_1, a_2\rangle + \delta_{b_1,b_2}\sum_{m}^{N_{\text{occ}}}\langle n, a_1\left|V_C\right|n, a_2\rangle \\ - \delta_{a_1,a_2}\sum_{n}^{N_{\text{occ}}}\langle n, b_2\left|V_C\right|n, b_1\rangle .\end{aligned} \tag{2.67}$$

If we assume that the scattering elements of the form $\langle n, i|\, V_C\, |n, j\rangle$ with $i \neq j$ are negligible we can obtain a more compact form:

$$\begin{aligned}\langle X_{s_2}|\hat{H}|X_{s_1}\rangle - \delta_{s_2,s_1}\langle GS|\hat{H}_{MB}|GS\rangle = \delta_{a_1,a_2}\delta_{b_2,b_1}[E_{b_1} + \Sigma_{(b_1)} - (E_{a_1} + \Sigma_{(a_1)})] \\ + \langle a_1, b_2\left|V_C\right|a_2, b_1\rangle - \langle a_1, b_2\left|V_C\right|b_1, a_2\rangle ,\end{aligned} \tag{2.68}$$

Substituting Eq. (2.68) into Eq. (2.56) gives the BSE:

$$\begin{aligned}&\left[(E_q + \textstyle\sum_{q,\sigma}) - (E_p + \textstyle\sum_{p,\sigma})\right] A^{\mu}_{p,q,\sigma} + \sum_{p',q',\sigma'}\left[\langle p', q|\, V_C\, |p, q'\rangle - \langle p', q|\, V_C\, |q', p\rangle\, \delta_{\sigma,\sigma'}\right] A^{\mu}_{p',q',\sigma'} \\ &= E_{\mu} A^{\mu}_{p,q,\sigma},\end{aligned} \tag{2.69}$$

where the self-energies $\Sigma_{q,\sigma} = -\sum_{p,\sigma'}\delta_{\sigma,\sigma'}\langle p, q|\, V_C\, |p, q\rangle$ renormalize the electron-hole pair energy and p indexes VB states with spin σ'. Eq. (2.69) matches the expression for the BSE found in Ref. 65. We will solve the BSE in Chapters 3 and 4, where we will study excitons in BLG QDs in the presence of deep and shallow confinement as well as the effects of TW.

2.4 Coulomb matrix elements

This section will briefly outline the procedure for computing the Coulomb matrix elements necessary for studying many-body interactions. These Coulomb matrix elements will be needed in Chapters 3 and 4, where we study excitons in BLG QDs. Throughout this thesis,

I have used the Coulomb matrix elements codes provided to me by Dr. Yasser Saleem and Dr. Daniel Miravet. Recalling the many-electron Hamiltonian in Eq. (2.38) written in terms of single-particle QD states, we need to compute $\langle p, q|V_C|r, s\rangle$. The expression for the wavefunctions of the single-particle QD states is given by:

$$|s\rangle = \sum_i D_i^s \, |i\rangle \, , \tag{2.70}$$

where D_i^s are the amplitudes, the sum goes over all atoms within each sublattice, and $|i\rangle$ is a Slater-like p_z orbital localized on atom i. In Chapter 3, we analyze the form of the QD wavefunctions and study their charge density in real and momentum space. Using Eq. (2.70), we can write the Coulomb matrix elements $\langle p, q|V_C|r, s\rangle$ between different QD states in terms of orbitals localized on different atoms as:

$$\langle p, q|V_C|r, s\rangle = \sum_{i,j,k,l} (D_i^p)^* \, (D_j^q)^* \, D_k^r \, D_l^s \, \langle i, j|V_C|k, l\rangle \, , \tag{2.71}$$

where $\langle i, j|V_C|k, l\rangle$ is given by:

$$\langle i, j|V_C|k, l\rangle = \iint \mathrm{d}\vec{r}_1 \, \phi_z^*(\vec{r}_1 - \vec{R}_i) \, \phi_z(\vec{r}_1 - \vec{R}_l) \mathrm{d}\vec{r}_2 \, \phi_z^*(\vec{r}_2 - \vec{R}_j) \, \phi_z(\vec{r}_2 - \vec{R}_k) \, \frac{e^2}{4\pi\epsilon_0\kappa|\vec{r}_1 - \vec{r}_2|}. \tag{2.72}$$

It is important to note that one must compute n_{SP}^4 of these Coulomb matrix elements $\langle p, q|V_C|r, s\rangle$, where n_{SP} is the number of single-particle QD states chosen. In the subsequent chapter, we take 32 QD states around the Fermi level, resulting in $1,048,576$ Coulomb matrix elements. Additionally, we will consider a computational box with over a million atoms, leading to the sum in Eq. (2.71), giving a computational complexity of $O(N^4)$ with around 10^{24} operations for this case.

We will only consider direct terms $\langle i, j|V_C|j, i\rangle$ as they provide the dominant contributions while scattering between different atoms has a much smaller impact. For the first case where the atomic positions $\vec{R}_i, \vec{R}_j, \vec{R}_k$, and $\vec{R}_l$ are near each other, the integral in Eq. (2.72) must be computed exactly using the Slater-like p_z orbitals defined in Eq. (2.6). Table 2.1

lists direct Coulomb matrix elements computed by numerical integration as reported in Ref. 64. The indices for atoms 1,2, 3, and 4 are defined such that when the values differ by 0, it represents that atoms i and j are identical; a difference of 1 indicates they are NNs; a difference of 2 indicates they are NNNs and a difference of 3 indicates they are next NNNs. The second case we will consider is long-ranged interaction, that is, for $\vec{R}_i = \vec{R}_l$

Coulomb matrix element	Value (eV)	Layer relation
$\langle 1,1\|V_C\|1,1\rangle$	17.307	Intralayer
$\langle 1,2\|V_C\|2,1\rangle$	8.942	Intralayer
$\langle 1,3\|V_C\|3,1\rangle$	5.582	Intralayer
$\langle 1,4\|V_C\|4,1\rangle$	4.856	Intralayer
$\langle 1,2\|V_C\|2,1\rangle$	4.562	Interlayer
$\langle 1,3\|V_C\|3,1\rangle$	4.103	Interlayer

Table 2.1: Direct Coulomb matrix elements for bilayer graphene in atomistic basis using Slater-like p_z orbitals. The first column specifies the matrix element, the second column corresponds to its value taken from Ref. 64 with $\xi = 3.25$, and the last column indicates whether the atoms are on the same layer (intralayer) or different layers (interlayer).

and $\vec{R}_j = \vec{R}_k$, but the positions of atoms i and j are far from each other (beyond NNN), then the interaction can be approximate as point-like:

$$\begin{aligned}\langle i,j|V_C|k,l\rangle &= \int \mathrm{d}\vec{r}_1\,|\phi_z(\vec{r}_1-\vec{R}_i)|^2 \int \mathrm{d}\vec{r}_2\,|\phi_z(\vec{r}_2-\vec{R}_j)|^2\,\frac{e^2}{4\pi\epsilon_0\kappa|\vec{r}_1-\vec{r}_2|}\\ &\approx \int \mathrm{d}\vec{r}_1\,\delta(\vec{r}_1-\vec{R}_i)\int \mathrm{d}\vec{r}_2\,\delta(\vec{r}_2-\vec{R}_j)\,\frac{e^2}{4\pi\epsilon_0\kappa|\vec{r}_1-\vec{r}_2|}\\ &= \frac{e^2}{4\pi\epsilon_0\kappa|\vec{R}_i-\vec{R}_j|},\end{aligned} \tag{2.73}$$

which simplifies the computation of the original 6-dimensional integrals. Substituting Eq. (2.73) into Eq. (2.71) gives:

$$\langle p,q|V_C|r,s\rangle = \sum_{i,j}(D_i^p)^*\,(D_j^q)^*\,D_j^r\,D_i^s\frac{e^2}{4\pi\epsilon_0\kappa|\vec{R}_i-\vec{R}_j|}, \tag{2.74}$$

which reduces the computational complexity to $O(N^2)$. Note that in Eq. (2.71) the Coulomb matrix elements depend on the difference between the positions of $\vec{R}_i$ and $\vec{R}_j$ rather than their positions themselves, allowing us to reduce the number of repetitive computations. To further accelerate the computation, we introduce the matrix $F^{\alpha\beta}$ given by:

$$F^{\alpha\beta} = \sum_i (D_i^\alpha)^* \, D_i^\beta. \tag{2.75}$$

Defining $V(\vec{R}_i - \vec{R}_j) = \frac{e^2}{4\pi\epsilon_0\kappa|\vec{R}_i - \vec{R}_j|}$, we can write Eq. (2.74) as:

$$\langle p, q|V_C|r, s\rangle = \sum_i F_i^{ps} \sum_j F_j^{qr} \, V(\vec{R}_i - \vec{R}_j). \tag{2.76}$$

We can define:

$$G_i^{qr} = \sum_j F_j^{qr} \, V(\vec{R}_i - \vec{R}_j), \tag{2.77}$$

and express the Coulomb matrix elements in Eq. (2.74) in terms of the new data structure G_i^{qr} as:

$$\langle p, q|V_C|r, s\rangle = \sum_i F_i^{ps} G_i^{qr}. \tag{2.78}$$

Although computing G_i^{qr} is computationally expensive, once we have a G vector, such as G^{11}, we can compute many Coulomb matrix elements of the form $\langle p, 1|V_C|1, s\rangle$ quickly, as there is only one sum in Eq. (2.78), resulting in computational complexity of $O(N)$. The codes used in this thesis implemented these techniques to reduce the runtime of computing Coulomb matrix elements.

Chapter 3

Excitons in Gated Bilayer Graphene Quantum Dots

I would like to note that this chapter is based on Ref. 65, but in the next chapter, we will extend this theory of excitons in BLG QDs. I have performed all calculations and computations except for density functional theory fitting for the hopping parameters and coding Coulomb matrix elements.

While BLG is gapless, applying a perpendicular electric field opens the gap, making BLG a voltage tunable semiconductor [16–23]. The tunability of the bandgap with the gate motivated the study of excitons in biased BLG [26, 27, 84, 85]. An exciton is a quasi-particle, bound state of interacting electron and a hole that forms upon optical excitation of an electron to the CB, leaving behind a hole in the valence band VB, which then interacts via Coulomb attraction. Excitons play an important role in the optical response of semiconductors, and those coupled strongly to light are particularly of interest [84,86,87].

Excitons in nanoscale semiconductors, e.g., self-assembled and graphene QDs, have been studied due to their potential applications, including lasers [52], LEDs [53], storage devices [54], and sources of entangled photon pairs via biexciton-exciton cascade [55–57]. However, the optical properties of these QDs are controlled by confining both electrons and holes through their structural attributes: size, shape, edge type, and material composition,

which are challenging to tune once fabricated. On the other hand, highly tunable laterally gated QDs confine either electrons or holes. Surprisingly, lateral gates can be applied to BLG in a way that leads to the emergence of a QD that effectively confines both electrons and holes [60,63–65]. BLG QDs offer high tunability of the optical and electronic properties through lateral gate voltages and provide an ideal system for studying electrically tunable excitons.

In this chapter, we employ an atomistic tight-binding model for BLG (outlined in section 2.1.2) for millions of atoms to obtain the gated BLG band structure. Next, we apply a Gaussian-shaped lateral confining potential to the gated BLG system and compute the resulting single-particle QD energy spectrum and wavefunctions. We also compute dipole matrix elements to analyze the oscillator strengths and optical selection rules for VB to CB transitions. We then include electron-electron interactions by first computing the microscopic Coulomb matrix elements, electron self-energy, and solving the Bethe-Salpeter equation to obtain the excitonic spectrum. Finally, we obtain the excitonic absorption spectrum and characterize the ground state exciton as a dark intervalley triplet exciton.

3.1 Gated bilayer graphene

We begin by considering Bernal-stacked BLG (described in section 2.1.2) as illustrated in Fig. 2.3, where the bottom (top) layer consists of sublattices A_1 and B_1 (A_2 and B_2). The NN in-plane bond length is $a = 0.143$ nm, and the interlayer distance is $h = 0.335$ nm. Our selected unit cell vectors are defined as $\vec{a}_1 = a(0, \sqrt{3})$ and $\vec{a}_2 = \frac{a}{2}(3, -\sqrt{3})$. We model our BLG graphene system by considering a rhomboidal computational box (Fig. 3.1(a); not to scale) constructed from $N_1 = N_2 = 633$ unit cells along the directions $\vec{a}_1$ and $\vec{a}_2$, encompassing over 1.6 million carbon atoms. Utilizing Bloch's theorem, the wavefunction on a sublattice l is expressed as:

$$\left|\phi_{\vec{k}}^{l}\right\rangle = \frac{1}{\sqrt{N}} \sum_{\vec{R}_l} e^{i\vec{k}\cdot\vec{R}_l} |\vec{R}_l\rangle, \tag{3.1}$$

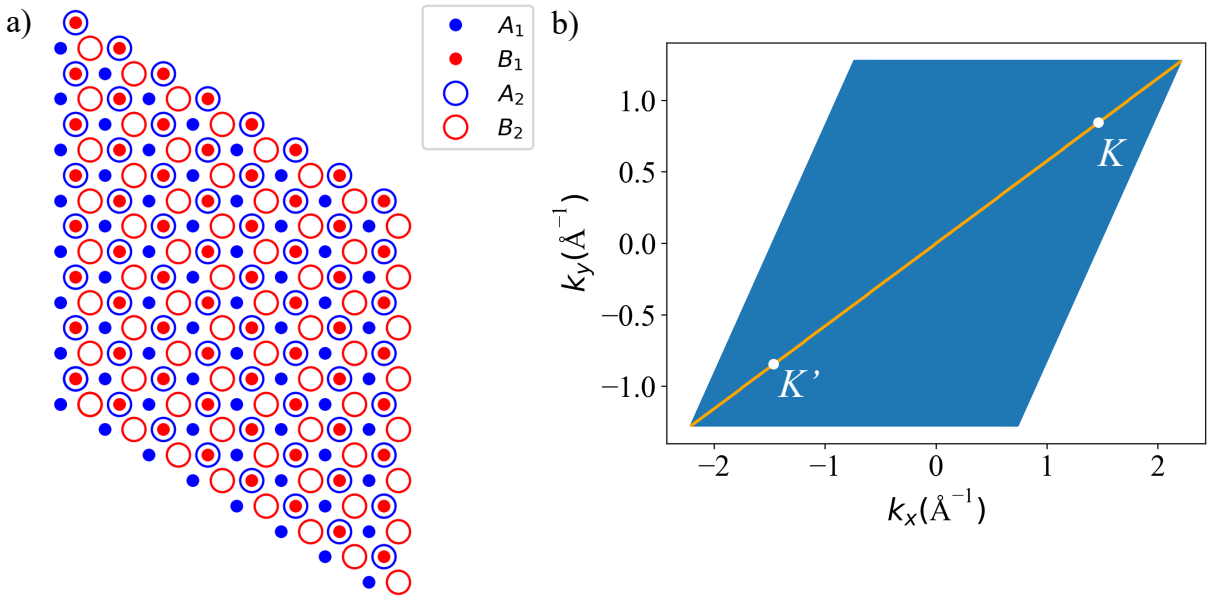

Figure 3.1: The rhomboidal computational box geometry used in the gated BLG QD calculations in (a) real space (dimensions not to scale) (b) momentum space. The orange line marks a path in momentum space between K and K' (white points) passing through Γ point.

where $N = N_1 \times N_2$ is the total number of unit cells, and $|\vec{R}_l\rangle$ represents a p_z Slater-like orbital localized on an atom at position $\vec{R}_l$. We can write the wavefunction of the lattice by taking a linear combination of the wavefunction for the four sublattice which is given by:

$$|\phi_{\vec{k}}\rangle = \frac{1}{\sqrt{N}} \sum_{l=1}^{4} \sum_{\vec{R}_l} A_{\vec{k},l}\, e^{i\vec{k}\cdot\vec{R}_l} |\vec{R}_l\rangle, \tag{3.2}$$

where we can write $\vec{R}_l = \vec{R} + \vec{d}_l$ with $\vec{R}$ being a position vector to a unit cell and $\vec{d}_l$ is the relative position of an atom on sublattice l within a unit cell. $\vec{d}_l$ can be chosen as:

$$\vec{d}_{A_1} = -\frac{h}{2}\hat{z}, \tag{3.3a}$$

$$\vec{d}_{B_1} = \vec{b} - \frac{h}{2}\hat{z}, \tag{3.3b}$$

$$\vec{d}_{A_2} = \vec{b} + \frac{h}{2}\hat{z}, \tag{3.3c}$$

$$\vec{d}_{B_2} = \frac{1}{3}(\vec{a}_1 + 2\vec{a}_2) + \frac{h}{2}\hat{z}, \tag{3.3d}$$

where $\vec{b} = a(\frac{1}{2}, \frac{\sqrt{3}}{2})$. Next, we impose the periodic boundary conditions on the wavefunction given in Eq. (3.2): $\phi_{\vec{k}}(\vec{r}) = \phi_{\vec{k}}(\vec{r} + N_1\vec{a}_1)$ and $\phi_{\vec{k}}(\vec{r}) = \phi_{\vec{k}}(\vec{r} + N_2\vec{a}_2)$ to eliminate finite-size effects, resulting in a discrete set of k-points in momentum space [60]. This gives the two conditions:

$$e^{-iN_1\vec{k}\cdot\vec{a}_1} = 1, \tag{3.4a}$$

$$e^{-iN_2\vec{k}\cdot\vec{a}_2} = 1, \tag{3.4b}$$

which can be equivalently written as:

$$k_x a_{1x} + k_y a_{1y} = \frac{2\pi n_1}{N_1}, \tag{3.5a}$$

$$k_x a_{2x} + k_y a_{2y} = \frac{2\pi n_2}{N_2}, \tag{3.5b}$$

where n_1 and n_2 are integers. Using Eq. (3.5a) and Eq. (3.5b) we can solve for k_x and k_y as:

$$k_x = \frac{\frac{2\pi n_1}{N_1}a_{2y} - \frac{2\pi n_2}{N_2}a_{1y}}{a_{2y}a_{1x} - a_{1y}a_{2x}}, \tag{3.6a}$$

$$k_y = \frac{\frac{2\pi n_1}{N_1}a_{2x} - \frac{2\pi n_2}{N_2}a_{1x}}{a_{2x}a_{1y} - a_{1x}a_{2y}}. \tag{3.6b}$$

Thus, we have the discrete set of allowed k-points given by:

$$\vec{k} = \frac{2\pi}{a_{1x}a_{2y} - a_{2x}a_{1y}} \left[\left(\frac{n_1}{N_1} a_{2y} - \frac{n_2}{N_2} a_{1y} \right) \hat{k}_x + \left(-\frac{n_1}{N_1} a_{2x} + \frac{n_2}{N_2} a_{1x} \right) \hat{k}_y \right], \tag{3.7}$$

where we have $n_i = -\frac{N_i - 1}{2}, \ldots, \frac{N_i - 1}{2}$ for both $i = 1, 2$. The discrete set of allowed k-points form a rhombus in momentum space as depicted in Fig. 3.1(b), which includes the K and $-K$ points. Recall from section 2.1.2 that the Hamiltonian describing bulk BLG in the presence of the applied electric field expressed in the basis of sublattices is given by:

$$H_{\text{bulk}}(\vec{k}) = \begin{pmatrix} \frac{V_E}{2} & \gamma_0 f(\vec{k}) & 0 & 0 \\ \gamma_0 f^*(\vec{k}) & \frac{V_E}{2} & \gamma_1 & 0 \\ 0 & \gamma_1 & -\frac{V_E}{2} & \gamma_0 f(\vec{k}) \\ 0 & 0 & \gamma_0 f^*(\vec{k}) & -\frac{V_E}{2} \end{pmatrix}, \tag{3.8}$$

where the parameter $\gamma_0 = -2.5$ eV represents the NN intralayer hopping and $\gamma_1 = 0.34$ eV denotes the interlayer hopping between pairs of orbitals on sublattices B_1 and A_2. We neglect the effects of trigonal warping for the moment, and we will study its effects in the subsequent chapter. The function $f(\vec{k})$ is given as $f(\vec{k}) = \sum_{j=1}^{3} e^{i\vec{k}\cdot\vec{\delta}_j}$, where $\vec{\delta}_j$ are the positions of the three NNs of a given atom. We can write them as $\vec{\delta}_1 = \vec{b}$, $\vec{\delta}_2 = \vec{b} - \vec{a}_2 - \vec{a}_1$ and $\vec{\delta}_3 = \vec{b} - \vec{a}_1$.

For a particular $\vec{k}$, we diagonalize the 4×4 Hamiltonian in Eq. (3.8) obtaining band eigenstates of the form $|\psi^p_{\vec{k}}\rangle = \sum_l A^p_{\vec{k},l} |\phi^l_{\vec{k}}\rangle$, where p labels one of the four bands (two VB and two CB), and l represents the sublattices A_1, B_1, A_2 and B_2. In the absence of TW, a ring of low-energy minima emerges around the K point in the lowest CB, which exhibits rotational symmetry and resembles the shape of a Mexican hat [88,89]. Additional details will be provided in Chapter 4.

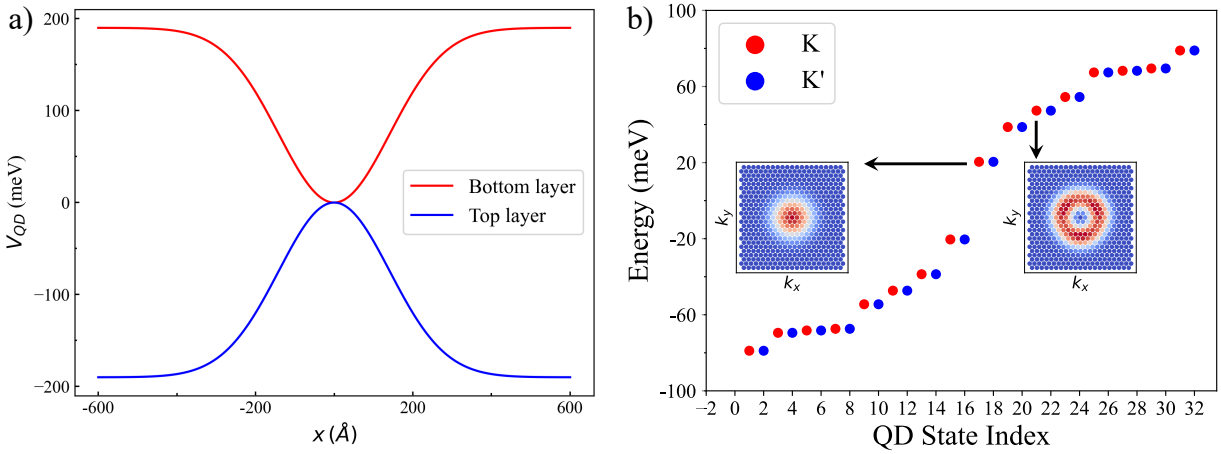

Figure 3.2: (a) Gaussian-shaped lateral confining potential with QD radius $R_{QD} = 20$ nm. (b) Single-particle energy spectrum of gated BLG QD near the Fermi level with a QD radius of $R_{QD} = 20$ nm, displacement voltage of $V_E = 380$ meV and confining potential depth of $V_0 = 190$ meV. Insets present the Fourier transform of the charge density in momentum space for QD states in valley K.

3.2 Gated bilayer graphene quantum dot

We apply different lateral confining potentials to each layer, effectively confining holes on the top layer ($z = +\frac{h}{2}$) and electrons on the bottom layer ($z = -\frac{h}{2}$) [60, 64, 65]. We adopt a single Gaussian potential given by:

$$V_{QD}(\rho) = \begin{cases} +V_0\, e^{-\frac{\rho^2}{R_{QD}^2}}, & z = +\frac{h}{2}, \\ -V_0\, e^{-\frac{\rho^2}{R_{QD}^2}}, & z = -\frac{h}{2}, \end{cases} \tag{3.9}$$

where R_{QD} is the QD radius and V_0 represents the depth of the confining potential. The confining potential given in Eq. (3.9) resembles a parabolic confining potential [63, 90–92] near the center of the dot, but differs in that it converges to zero at large distances from the center of the dot. We will take $V_0 = \frac{V_E}{2}$, the voltage drop on the bottom layer will cancel the displacement field potential difference of $\frac{V_E}{2}$ resulting in zero potential at the center of the QD. The same applies to the top layer. Experimentally this corresponds to forming

circular openings in the top and bottom gates [64]. To account for the redistribution of charge as a result of the applied electric field, we account for screening by introducing an effective potential that is the sum of Gaussians [60, 65]:

$$V_{QD}^{\text{eff}}(\rho) = \begin{cases} +(c_1 e^{-\frac{\alpha_1 \rho^2}{R_{QD}^2}} + c_2 e^{-\frac{\alpha_2 \rho^2}{R_{QD}^2}}), & z = +\frac{h}{2}, \\ -(c_1 e^{-\frac{\alpha_1 \rho^2}{R_{QD}^2}} + c_2 e^{-\frac{\alpha_2 \rho^2}{R_{QD}^2}}), & z = -\frac{h}{2}, \end{cases} \tag{3.10}$$

where the parameters $c_1 = -0.018$ eV, $c_2 = 0.207$ eV, $\alpha_1 = 6.128, \alpha_2 = 1.006$ and the QD radius is taken to be $R_{QD} = 20$ nm. The resulting confining potential profile is presented in Fig 3.2(a), which includes the overall potential of the displacement field and V_{QD}^{eff} given in Eq. (3.10). Including this confining potential, the Hamiltonian for the gated BLG QD becomes:

$$\hat{H}_{QD} = \hat{H}_{\text{bulk}} + \hat{V}_{QD}^{\text{eff}}. \tag{3.11}$$

To obtain the single-particle eigenstates of the QD Hamiltonian, we expand the QD states in the basis of band eigenstates of the bulk Hamiltonian in Eq. (3.8) as:

$$\varphi_s(\vec{r}) = \sum_{\vec{k}} \sum_{p} B_{p,\vec{k}}^{s} \, \psi_{\vec{k}}^{p}(\vec{r}), \tag{3.12}$$

where $\vec{k}$ represents the discrete set of points in the momentum space, and p denotes the BLG band index. Using the single-particle QD wavefunctions with index s in Eq. (3.12) as a solution of the Schrodinger equation corresponding to the QD, we can diagonalize the QD Hamiltonian in Eq. (3.11) by solving the eigenvalue equation given by:

$$\varepsilon_{p,\vec{k}} \, B_{p,\vec{k}}^{s} + \sum_{p',\vec{k}'} \langle \psi_{\vec{k}}^{p} | \hat{V}_{QD}^{\text{eff}} | \psi_{\vec{k}'}^{p'} \rangle B_{p',\vec{k}'}^{s} = E_s B_{p,\vec{k}}^{s}. \tag{3.13}$$

Here $\varepsilon_{p,\vec{k}}$ are the eigenenergies of the bulk Hamiltonian in Eq. (3.8) and the coefficients $B_{p,\vec{k}}^{s}$ are obtained by solving Eq. (3.13). Note that in obtaining Eq. (3.13) we have used the fact that $|\psi_{\vec{k}}^{p}\rangle$ are eigenstates of the bulk Hamiltonian and that $\langle \psi_{\vec{k}'}^{p'} | \psi_{\vec{k}}^{p} \rangle = \delta_{\vec{k},\vec{k}'} \delta_{p,p'}$. The

confining potential couples wavevectors $\vec{k}$ and $\vec{k}'$ in bands p and p' via the matrix element:

$$\langle \psi^p_{\vec{k}} | \hat{V}^{\text{eff}}_{QD} | \psi^{p'}_{\vec{k}'} \rangle = \sum_{l,l'} (A^p_{\vec{k},l})^* \, A^{p'}_{\vec{k}',l'} \langle \phi^l_{\vec{k}} | \hat{V}^{\text{eff}}_{QD} | \phi^{l'}_{\vec{k}'} \rangle. \tag{3.14}$$

Substituting the expression for the wavefunction on a sublattice l given in Eq. (3.1) into Eq. (3.14) results in:

$$\langle \psi^p_{\vec{k}} | \hat{V}^{\text{eff}}_{QD} | \psi^{p'}_{\vec{k}'} \rangle = \frac{1}{N} \sum_{l,l'} \sum_{\vec{R}_l, \vec{R}'_{l'}} (A^p_{\vec{k},l})^* \, A^{p'}_{\vec{k}',l'} e^{-i\vec{k}\cdot\vec{R}_l} e^{i\vec{k}'\cdot\vec{R}'_{l'}} \langle \vec{R}_l | \hat{V}^{\text{eff}}_{QD} | \vec{R}'_{l'} \rangle. \tag{3.15}$$

Substituting $\vec{R}_l = \vec{R} + \vec{d}_l$ gives:

$$\langle \psi^p_{\vec{k}} | \hat{V}^{\text{eff}}_{QD} | \psi^{p'}_{\vec{k}'} \rangle = \frac{1}{N} \sum_{l,l'} \sum_{\vec{R},\vec{R}'} (A^p_{\vec{k},l})^* \, A^{p'}_{\vec{k}',l'} e^{-i\vec{k}\cdot(\vec{R}+\vec{d}_l)} e^{i\vec{k}'\cdot(\vec{R}'+\vec{d}_{l'})} \langle \vec{R}_l | \hat{V}^{\text{eff}}_{QD} | \vec{R}'_{l'} \rangle. \tag{3.16}$$

Assuming that the confining potential in real space does not vary much within a unit cell and making the approximation $\langle \vec{R}_l | \hat{V}^{\text{eff}}_{QD} | \vec{R}'_{l'} \rangle \approx \hat{V}^{\text{eff}}_{QD}(\rho = \frac{\vec{R}+\vec{R}'}{2}) \langle \vec{R}_l | \vec{R}'_{l'} \rangle$ gives:

$$\langle \psi^p_{\vec{k}} | \hat{V}^{\text{eff}}_{QD} | \psi^{p'}_{\vec{k}'} \rangle = \frac{1}{N} \sum_{l,l'} \sum_{\vec{R},\vec{R}'} (A^p_{\vec{k},l})^* \, A^{p'}_{\vec{k}',l'} e^{-i\vec{k}\cdot(\vec{R}+\vec{d}_l)} e^{i\vec{k}'\cdot(\vec{R}'+\vec{d}_{l'})} \hat{V}^{\text{eff}}_{QD}(\rho = \frac{\vec{R}+\vec{R}'}{2}) \delta_{\vec{R},\vec{R}'} \delta_{l,l'}, \tag{3.17}$$

and this can be simplified to:

$$\langle \psi^p_{\vec{k}} | \hat{V}^{\text{eff}}_{QD} | \psi^{p'}_{\vec{k}'} \rangle = \frac{1}{N} \sum_{l} e^{i(\vec{k}'-\vec{k})\cdot\vec{d}_l} (A^p_{\vec{k},l})^* \, A^{p'}_{\vec{k}',l} \sum_{\vec{R}} e^{i(\vec{k}'-\vec{k})\cdot\vec{R}} \hat{V}^{\text{eff}}_{QD}(\rho = \vec{R}). \tag{3.18}$$

Let's define $V_{\vec{k},\vec{k}',l} = \frac{1}{N} \sum_{\vec{R}} e^{i(\vec{k}'-\vec{k})\cdot\vec{R}} \, \hat{V}^{\text{eff}}_{QD}(\rho = \vec{R})$, which represents the Fourier transform of the confining potential. Therefore, Eq. (3.18) becomes:

$$\langle \psi^p_{\vec{k}} | \hat{V}^{\text{eff}}_{QD} | \psi^{p'}_{\vec{k}'} \rangle = \frac{1}{N} \sum_{l} e^{i(\vec{k}'-\vec{k})\cdot\vec{d}_l} (A^p_{\vec{k},l})^* \, A^{p'}_{\vec{k}',l} V_{\vec{k},\vec{k}',l}. \tag{3.19}$$

We can solve for the Fourier transform for the top layer and relate it to the bottom layer

as they differ only by a negative sign. Let us write $\vec{R} = R_x\hat{x} + R_y\hat{y}$, then the Fourier transform of a 2D Gaussian is given by:

$$\mathcal{F}\left(e^{-\frac{R^2}{R_{QD}^2}}\right) = \frac{R_{QD}^2}{2}e^{-\frac{R_{QD}^2 q^2}{4}} \tag{3.20}$$

Taking the inverse Fourier Transform of both sides of Eq. (3.20) gives:

$$e^{-\frac{R^2}{R_{\rm QD}^2}} = \frac{R_{\rm QD}^2}{4\pi}\int_{-\infty}^{\infty} d\vec{q}\, e^{-\frac{R_{\rm QD}^2 q^2}{4}} e^{i\vec{q}\cdot\vec{R}}.$$

We can convert the integral in the above expression into a discrete sum:

$$e^{-\frac{R^2}{R_{\rm QD}^2}} = \frac{R_{\rm QD}^2}{4\pi}\sum_{\vec{q}} A_k\, e^{-\frac{R_{\rm QD}^2 q^2}{4}} e^{i\vec{q}\cdot\vec{R}}, \tag{3.21}$$

where A_k represents the reciprocal lattice unit cell area and can be found to be $A_k = \frac{8\pi^2}{3\sqrt{3}a^2 N_1 N_2}$. We can now compute $V_{\vec{k},\vec{k}',l}$ for top layer with $l = A_2, B_2$:

$$\begin{aligned}
V_{\vec{k},\vec{k}',l=A_2,B_2} &= \frac{1}{N}\sum_{\vec{R}} e^{i\left(\vec{k}'-\vec{k}\right)\cdot\vec{R}}\hat{V}_{QD}^{\rm eff}(\rho=\vec{R}) \\
&= \frac{1}{N}\sum_{\vec{R}} e^{i\left(\vec{k}'-\vec{k}\right)\cdot\vec{R}}(c_1 e^{-\frac{\alpha_1 R^2}{R_{QD}^2}} + c_2 e^{-\frac{\alpha_2 R^2}{R_{QD}^2}}) \\
&= \frac{R_{\rm QD}^2 A_k}{4\pi N}\sum_{\vec{R}}\sum_{\vec{q}} e^{i\left(\vec{k}'-\vec{k}+\vec{q}\right)\cdot\vec{R}}\left(\frac{c_1}{\alpha_1}e^{-\frac{R_{\rm QD}^2 q^2}{4\alpha_1}} + \frac{c_2}{\alpha_2}e^{-\frac{R_{\rm QD}^2 q^2}{4\alpha_2}}\right) \\
&= \frac{R_{\rm QD}^2 A_k}{4\pi N}\sum_{\vec{q}}\left(\frac{c_1}{\alpha_1}e^{-\frac{R_{\rm QD}^2 q^2}{4\alpha_1}} + \frac{c_2}{\alpha_2}e^{-\frac{R_{\rm QD}^2 q^2}{4\alpha_2}}\right)\sum_{\vec{R}} e^{i\left(\vec{k}'-\vec{k}+\vec{q}\right)\cdot\vec{R}} \\
&= \frac{R_{\rm QD}^2 A_k}{4\pi N}\sum_{\vec{q}}\left(\frac{c_1}{\alpha_1}e^{-\frac{R_{\rm QD}^2 q^2}{4\alpha_1}} + \frac{c_2}{\alpha_2}e^{-\frac{R_{\rm QD}^2 q^2}{4\alpha_2}}\right) N\delta_{\vec{k}'-\vec{k},\vec{q}} \\
&= \frac{R_{\rm QD}^2 A_k}{4\pi}\left(\frac{c_1}{\alpha_1}e^{-\frac{R_{\rm QD}^2(\vec{k}'-\vec{k})^2}{4\alpha_1}} + \frac{c_2}{\alpha_2}e^{-\frac{R_{\rm QD}^2(\vec{k}'-\vec{k})^2}{4\alpha_2}}\right).
\end{aligned} \tag{3.22}$$

Therefore, we have the expression for the Fourier transform of the confining potential on both layers given by:

$$V_{\vec{k},\vec{k}',l} = \pm \frac{R_{\mathrm{QD}}^2 A_k}{4\pi} \left(\frac{c_1}{\alpha_1} e^{-\frac{R_{\mathrm{QD}}^2 (\vec{k}'-\vec{k})^2}{4\alpha_1}} + \frac{c_2}{\alpha_2} e^{-\frac{R_{\mathrm{QD}}^2 (\vec{k}'-\vec{k})^2}{4\alpha_2}} \right), \tag{3.23}$$

where the + (−) sign corresponds to sublattices $l = A_2, B_2$, ($l = A_1, B_1$). We impose an energy cut-off of $E_{cut} = 600$ meV on our band states $|\psi_{\vec{k}}^p\rangle$, including only those band states with energy $\varepsilon_{p,\vec{k}}$ in the range $|\varepsilon_{p,\vec{k}}| \leq E_{cut}$. This ensures the convergence of single-particle QD energies around the Fermi level. Half of our band states are near the K point, while the other half cluster around the $-K$ point, giving rise to valley doublets and quadruply degenerate shells (including spin).

To obtain the QD energy spectrum, we solve the eigenvalue problem defined by Eq. (3.13), with a displacement voltage of $V_E = 380$ meV, QD radius of $R_{QD} = 20$ nm and confining potential depth of $V_0 = 190$ meV. The resulting energy levels, displayed in Fig. 3.2(b), are doubly degenerate due to valley degeneracy. We can also examine the Fourier transform of the charge density to understand where these QD states are localized in momentum space. In the insets of Fig. 3.2(b), we present the Fourier transform of the charge density around valley K for the first and third QD CB states. The lowest energy CB states in gated BLG originate from the ring of minima's along the Mexican hat, as shown in the top panel of Fig. 4.2(a). However, one notices that for the lowest QD CB state, the Fourier transform of the charge density is centered around the K point. Furthermore, upon examining the third QD CB state, one observes a ring-like shape around the K point, closely resembling the ring of minima's found in the CB of gated BLG. The real space QD wavefunctions can also be expressed in terms of p_z orbitals as:

$$|\phi^s\rangle = \sum_{\vec{R}} \sum_{l=1}^{4} C_{\vec{R},l}^s |\vec{R}_l\rangle, \tag{3.24}$$

where $C^s_{\vec{R},l} = \frac{1}{\sqrt{N_u}} \sum_{\vec{k}} \sum_{p=1}^{4} B^s_{p,\vec{k}} A^p_{\vec{k},l} e^{i\vec{k}\cdot(\vec{R}+\vec{d}_l)}$ or in a more compact notation:

$$|s\rangle = \sum_i D^s_i \, |i\rangle \, , \tag{3.25}$$

where the sum goes over all atoms within each sublattice and $|i\rangle = |\vec{R}_i\rangle$. After solving Eq. (3.13), we obtained the amplitudes $B^s_{p,\vec{k}}$, which we used to determine the coefficients $C^s_{\vec{R},l}$, allowing us to plot the charge density of the QD states in real space on the two layers. In Fig. 3.3(a-d), we present the charge densities for the single-particle QD states from the first and third lowest CB valley doublets. Specifically, we plot the charge densities for the QD states 17 and 21 from Fig. 3.2(b) on the lower (left) and upper (right) layers of the BLG. Notably, the probability density is higher on the lower layer than the upper layer, consistent with the findings in gated BLG, where the lowest CB near the K point is predominantly on sublattice A_1. On the lower layer, the first CB QD state is localized around the center of the QD, while the third CB state forms a ring. On the upper layer, both CB states form a ring around the center of the dot. In Fig. 3.3(e), we analyze the probability density of the 32 QD states around the Fermi level displayed in Fig. 3.2(b). We observe that the CB states are mostly on sublattice A_1, while the VB states are predominantly on sublattice B_2, again consistent with the findings in gated BLG near the K point [64].

3.3 Dipole matrix elements

Now that we have obtained the single-particle QD states, the next step is to examine the interaction of the BLG QD with light. We incorporate the coupling of light with different states through dipole matrix elements $\vec{D}_{p,q} = \langle p|\vec{r}|q\rangle$, which connect the QD states p and q, with $\vec{r}$ denoting the electron position. Using the expression for the QD wavefunctions in Eq. (3.25), we can write the DME as:

$$\vec{D}_{pq} = \sum_{(i,j)} (C^p_i)^* (C^q_j) \langle i|\vec{r}|j\rangle. \tag{3.26}$$

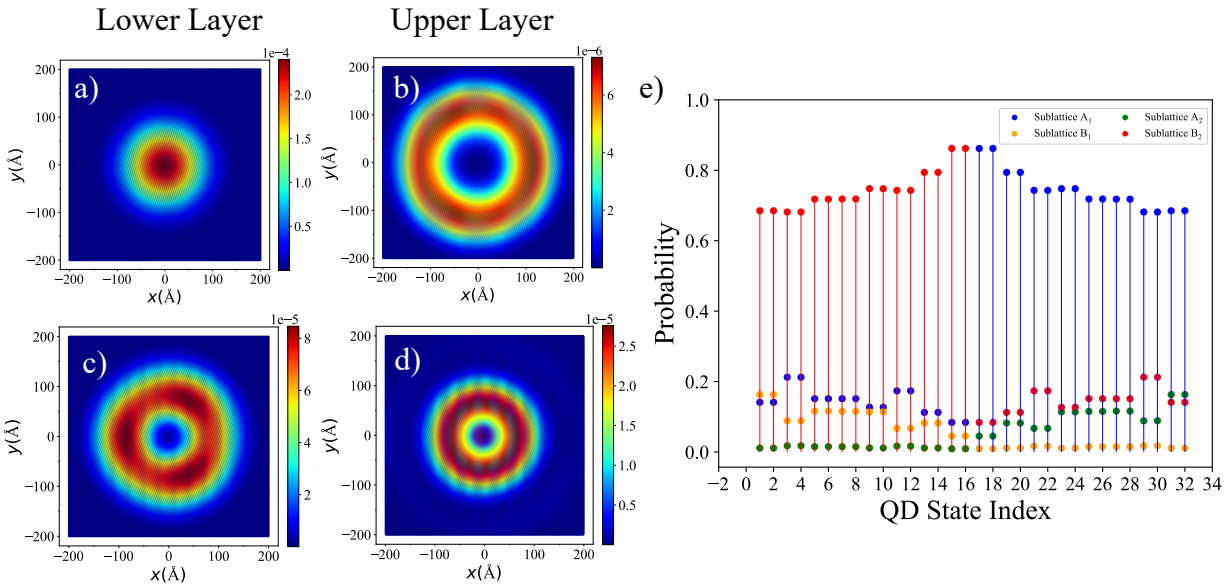

Figure 3.3: Probability densities of single-particle states from the first and third lowest CB valley doublets. Panels (a) and (c) show the charge densities of states 17 and 21, respectively, on the lower layer, while panels (b) and (d) show the densities on the top layer. (e) Charge density of the QD wavefunctions by sublattices of gated BLG QD.

To obtain an explicit expression for the DME, we begin with $\langle i|\vec{r}|j\rangle$:

$$\langle i|\vec{r}|j\rangle = \int \mathrm{d}\vec{r}\,\phi_z^*(\vec{r}-\vec{R}_i)\,\vec{r}\,\phi_z(\vec{r}-\vec{R}_j), \tag{3.27}$$

we can now shift $\vec{r}$ by the position of the jth atomic orbital, $\vec{r}\to\vec{r}+\vec{R}_j$, which gives:

$$\begin{aligned}\langle i|\vec{r}|j\rangle &= \int \mathrm{d}\vec{r}\,\phi_z^*(\vec{r}+\vec{R}_j-\vec{R}_i)\,(\vec{r}+\vec{R}_j)\,\phi_z(\vec{r}) \\ &= \int \mathrm{d}\vec{r}\,\phi_z^*(\vec{r}+\vec{R}_j-\vec{R}_i)\,\vec{r}\,\phi_z(\vec{r}) + \vec{R}_j\int \mathrm{d}\vec{r}\,\phi_z^*(\vec{r}+\vec{R}_j-\vec{R}_i)\,\phi_z(\vec{r}) \\ &= \int \mathrm{d}\vec{r}\,\phi_z^*(\vec{r}+\vec{R}_j-\vec{R}_i)\,\vec{r}\,\phi_z(\vec{r}) + \vec{R}_j\,\delta_{ij}.\end{aligned} \tag{3.28}$$

If $i = j$, the first term in Eq. (3.28) will equal zero as it is an integral over an odd function. We can write Eq. (3.28) as:

$$\langle i|\vec{r}|j\rangle = \int \mathrm{d}\vec{r}\,\phi_z^*(\vec{r} + \vec{R}_j - \vec{R}_i)\,\vec{r}\,\phi_z(\vec{r})(1 - \delta_{ij}) + \vec{R}_j\delta_{ij}, \tag{3.29}$$

The first term in Eq. (3.29) is a vector in the direction $\hat{R}_j - \hat{R}_i$, since the electron changes states from j to i, but the direction of the dipole moment is opposite of this (negative to positive charge). Utilizing this fact, we can rewrite the first term of Eq. (3.29) as a magnitude times a direction:

$$\langle i|\vec{r}|j\rangle = D_{ij}(\hat{R}_j - \hat{R}_i)(1 - \delta_{ij}) + \vec{R}_j\delta_{ij}, \tag{3.30}$$

where $D_{ij} = \left|\int \mathrm{d}\vec{r}\,\phi_z^*(\vec{r} + \vec{R}_j - \vec{R}_i)\,\vec{r}\,\phi_z(\vec{r})\right|$ and $\phi_z(\vec{r})$ is a Slater p_z orbital. If i and j are NN, we find numerically by Riemann sums that $D_{ij} = 0.3137625\,a_0$, whereas for NNN $D_{ij} = 0.0711159\,a_0$ where a_0 is the Bohr radius. In Fig. 3.4(a), black arrows connect states in the VB and CB with large DMEs for two K-valleys. In contrast to self-assembled and graphene QDs [48, 93], the state at the top of the VB (identified by the QD index 16) exhibits a weak connection to the lowest CB state (18) but instead couples more strongly to the third excited state (22). λ_a denotes this transition. Symmetrically, the strong transition λ_b occurs between the bottom of the CB (+17) and the third VB state (11). One can conduct an identical analysis with QD states in the other valley. Transitions within each valley can be analyzed separately, as QD states from different valleys do not optically couple.

In Fig. 3.4(b), we present the joint optical density of states for non-interacting electron-hole pairs. We label the transitions corresponding to each peak; the brightest peaks correspond to the transitions λ_a and λ_b. Furthermore, we will analyze why the transition across the gap is dark and why the brightest transition occurs between the QD states corresponding to the transitions λ_a and λ_b in Chapter 5 using an effective mass model.

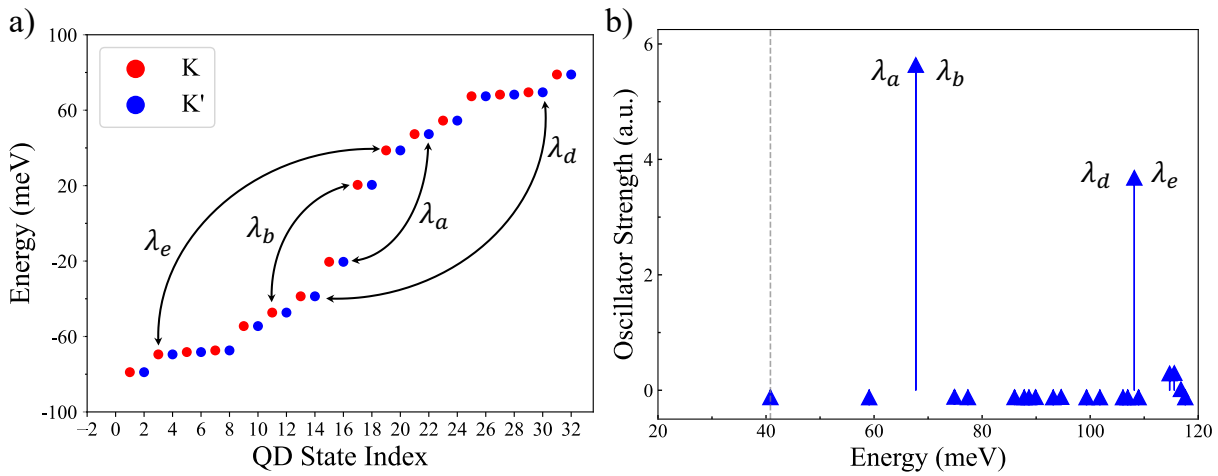

Figure 3.4: Dipole Matrix Elements for optical transitions. (a) Single-particle energy spectrum of gated BLG QD near the Fermi level for two K-valleys. Black arrows connect pairs of VB and CB states characterized by significant dipole matrix elements. (b) Joint optical density of states for the non-interacting electron and hole in BLG QD. Blue arrows show the magnitude of the corresponding dipole elements.

3.4 Exciton spectrum

In this section, we study the excitonic properties of gated BLG QDs and analyze the exciton energy spectrum. We approximate the many-electron ground state as a single Slater determinant $|GS\rangle = \prod_{p,\sigma} c^\dagger_{p,\sigma} |0\rangle$, where index p runs over occupied VB states. The exciton wavefunction $|\Psi^\mu\rangle$ for exciton state μ is a linear combination of electron-hole pair excitations conserving S_z:

$$|\Psi^\mu\rangle = \sum_{p,q,\sigma} A^\mu_{p,q,\sigma} c^\dagger_{q,\sigma} c_{p,\sigma} |GS\rangle \,. \tag{3.31}$$

Here, μ indexes the exciton states, and the index p labels all VB states, while q labels all CB states. The amplitudes $A^\mu_{p,q,\sigma}$ and excitonic energies E_μ can be obtained by solving the

Bethe-Salpeter equation (derived in section 2.2):

$$\begin{aligned}&\left[(E_q + \textstyle\sum_{q,\sigma}) - (E_p + \textstyle\sum_{p,\sigma})\right] A^{\mu}_{p,q,\sigma} \\ &+ \sum_{p',q',\sigma'} \left[\langle p', q|V_C|p, q'\rangle - \langle p', q|V_C|q', p\rangle \delta_{\sigma,\sigma'}\right] A^{\mu}_{p',q',\sigma'} \\ &= E_{\mu} A^{\mu}_{p,q,\sigma}.\end{aligned} \tag{3.32}$$

The electron-hole pair energy is renormalized by self-energies $\Sigma_{q,\sigma} = -\sum_{p,\sigma'} \delta_{\sigma,\sigma'} \langle p, q|V_C|p, q\rangle$, where p indexes VB states. Examining the second line of Eq. (3.32) with $p = p'$ and $q = q'$, one observes that the repulsive exchange interaction raises the energy of an electron-hole pair. In contrast, the direct electron-hole attraction lowers it. The other Coulomb matrix elements account for the interaction between different electron-hole pairs. We solve the Bethe-Salpeter equation in the subspace of 32 QD states around the Fermi level. In Fig. 3.5, we plot the exciton energy spectrum for different levels of electron-electron interactions.

We begin by examining the exciton energy spectrum of noninteracting electron-hole pairs, as shown in Fig. 3.5(a). This analysis assumes all Coulomb matrix elements in Eq. (3.32) are zero. The existence of eight-fold degenerate low-energy exciton states can be understood by constructing electron-hole pairs from states at the top of the VB and bottom of the CB while conserving S_z. This involves removing an electron from the top of the VB (QD states 15/16) and placing this electron on the lowest CB state (17/18) in Fig. 3.4(a). Due to the spin and valley degeneracies of the QD level, there are two possible electron-hole pairs in each valley and four pairs between valleys (including spin), resulting in eight electron-hole pair configurations constructed across the gap.

Above these eight low-energy exciton states, one observes sixteen-fold degenerate shells beginning at around 60 meV. The origin of these sixteen degenerate levels can be understood through a similar analysis. By removing an electron from the VB with QD index (13/14) and placing it in the bottom of the CB (17/18) in Fig. 3.4(a), we obtain eight degenerate exciton states. However, since we have not included the hopping parameter γ_4, the system retains electron-hole symmetry, which means that removing an electron from the top of the VB (15/16) and placing it in the second CB doublet states (19/20) results

in eight additional electron-hole pairs with the same energy. Consequently, this leads to a shell of sixteen degenerate exciton states.

Next, we include the electron and hole self-energy terms in Eq. (3.32), which require 120 VB states to achieve full convergence. This inclusion results in a blue-shift of the exciton energy spectra as displayed in Fig. 3.5(b). Additionally, the sixteen-fold degenerate shells found in the case of noninteracting electron-hole pairs are split into shells of eight because the self-energies for electron-hole pairs involving QD states 13/14 and 17/18 are different from those involving QD states 15/16 and 19/20.

Subsequently, we include direct and exchange Coulomb matrix elements, i.e., the second line of Eq. (3.32) with $p = p', q = q'$ and $\sigma = \sigma'$ in addition to the self-energies to obtain the exciton energy spectra presented in Fig. 3.5(c). The eight-fold degenerate low-energy exciton states remained degenerate until the inclusion of direct and exchange interactions. With this inclusion, the eight configurations mix and separate in energy. The configurations are categorized as intervalley and intravalley electron-hole pairs, where the electron and hole can either be from QD states in different or the same valleys. While the direct interaction is valley-independent, the exchange interaction is larger within a valley than between valleys. Intervalley electron-hole pairs increase the valley polarization compared to intravalley pairs, resulting in lower energy for intervalley pairs through increased exchange interaction. However, the energy difference is almost not visible in Fig. 3.5(c).

After including all electron-electron interactions in Eq. (3.32), we obtain the excitonic energy spectra shown in Fig. 3.5(d). These excitons can be further categorized by spin as singlets or triplets, with triplets having lower energy due to exchange interaction. This is why the ground state exciton is an intervalley triplet exciton, a linear combination of intervalley electron-hole pairs with total spin $S = 1$.

3.5 Absorption spectra

We now investigate the absorption of a single photon by the gated BLG QD, which is excited from the ground state to an exciton state optically. The absorption spectrum gives

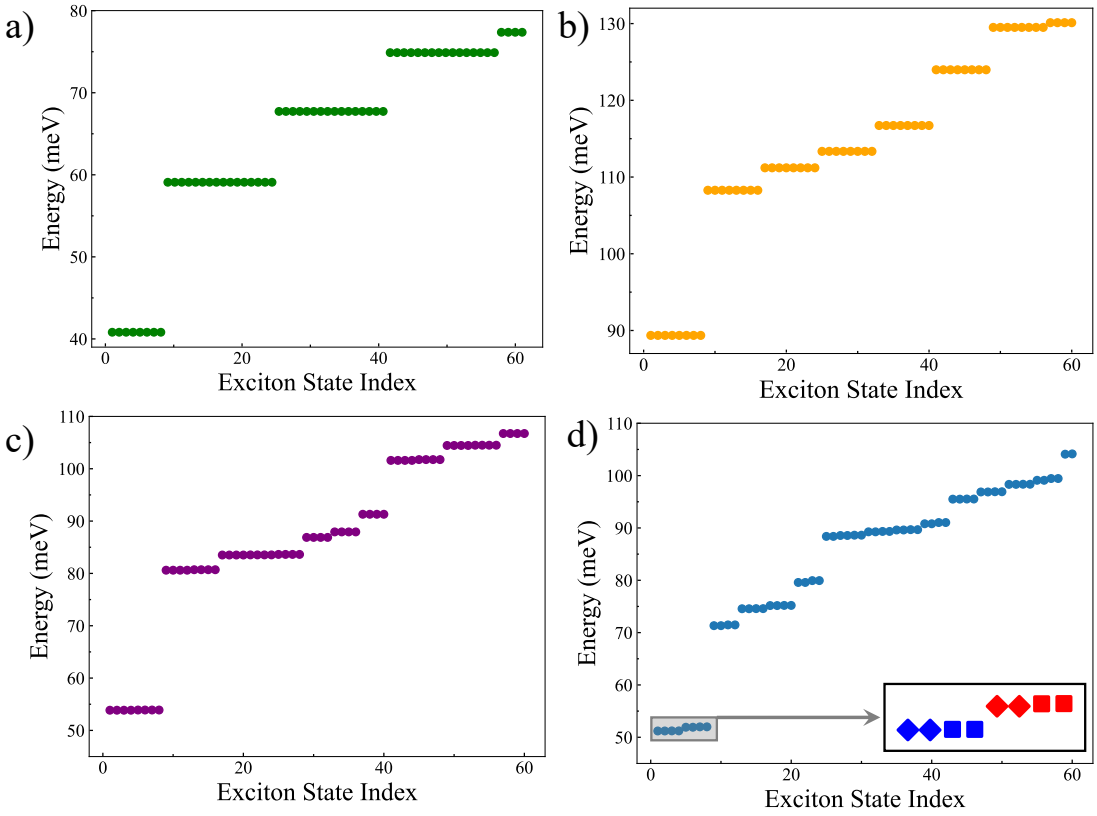

Figure 3.5: Exciton energy spectra including different levels of electron-electron interaction. Exciton energy spectra in the case of (a) noninteracting electron-hole pairs. (b) renormalized by self-energy. (c) self-energy and attractive direct and repulsive exchange interaction. (d) all electron-electron interaction, including correlation.

the probability that a photon with energy ω is absorbed and can be derived from Fermi's golden rule [48, 56, 65, 94] as:

$$A(\omega) = \sum_{\nu,\nu'} W_\nu \left| \langle \Phi_{\nu'} | \hat{P}^+ | \Phi_\nu \rangle \right|^2 \delta(E_{\nu'} - E_\nu - \omega), \tag{3.33}$$

Where W_ν is the probability that the initial state ν is occupied and $\hat{P}^+ = \sum_{p,q,\sigma} (\vec{\varepsilon} \cdot \vec{D}_{qp}) \hat{c}^\dagger_{q\sigma} \hat{c}_{p\sigma}$ is the polarization operator with $\vec{\varepsilon}$ being the polarization vector of the applied electric field. For a ground state given by a fully occupied valence band, for an excitation

to a state $\nu' = \mu$ we have:

$$A(\omega) = \sum_{\mu} \left| \langle \Phi_{\mu} | \hat{P}^{+} | GS \rangle \right|^{2} \delta(E_{\mu} - \omega), \tag{3.34}$$

where we shift our energies so that $E_{GS} = 0$ and since $|\Phi_{\beta}\rangle = \sum_{p,q,\sigma} A^{\mu}_{p,q,\sigma} \hat{c}^{\dagger}_{q\sigma} \hat{c}_{p\sigma} |GS\rangle$, substituting gives:

$$A(\omega) = \sum_{\mu} \left| \sum_{p,q,\sigma,p',q'} \left(A^{\mu}_{p,q,\sigma}\right)^{*} (\vec{\varepsilon} \cdot \vec{D}_{q'p'}) \langle GS | \hat{c}^{\dagger}_{p\sigma} \hat{c}_{q\sigma} \hat{c}^{\dagger}_{q'\sigma'} \hat{c}_{p'\sigma'} | GS \rangle \right|^{2} \delta(E_{\mu} - \omega).$$

Using the anti-commutation rules, $\{c_i, c_j^{\dagger}\} = \delta_{ij}$ and $\{c_i, c_j\} = \{c_i^{\dagger}, c_j^{\dagger}\} = 0$, we obtain:

$$A(\omega) = \sum_{\mu} \left| \sum_{p,q,\sigma} \vec{\epsilon}_{\pm} \cdot \vec{D}_{q,p} (A^{\mu}_{p,q,\sigma})^{*} \right|^{2} \delta(E_{\mu} - \omega). \tag{3.35}$$

Here, we consider circularly polarized light with $\vec{\epsilon}_{\pm} = \frac{1}{\sqrt{2}}(1, \pm i)$, allowing for both left or right-handed polarizations. We assumed the initial state to be the ground state, corresponding to a fully occupied valence band.

In Fig. 3.6, we plot the Gaussian broadened absorption spectrum, including different levels of electron-electron interactions. The grey vertical lines correspond to the excitonic energies E_{μ}. Starting with the case of noninteracting electron-hole pairs in Fig. 3.6(a), one observes a bright peak around 68 meV, which corresponds to the bright optical transitions labeled λ_a and λ_b in Fig. 3.4(a). The second bright peak around 108 meV corresponds to the bright optical transition λ_d and λ_e. Next, we include the effects of electron and hole self-energies, causing the bright peaks to shift to higher energy as shown in Fig. 3.6(b). Furthermore, the effects of the self-energies split the sixteen-fold degenerate exciton states into eight-fold states, causing both bright peaks to split into two.

In Fig. 3.6(c), one observes that including direct and exchange interactions, in addition to the self-energies, has red-shifted the energy of the bright peaks. Despite this shift, both bright peaks have remained split into two. Including all correlation effects from electron-

electron interactions has resulted in a large peak around 105 meV, corresponding to the brightest transitions, and a second bright peak around 143 meV as presented in Fig. 3.6(d). However, no peaks are visible for the ground state exciton around 51 meV, indicating the ground state is dark. Many dark intervalley excitons at lower energy arise from electron-electron interactions, which split exciton states into intervalley and intravalley excitons. Intervalley excitons consist of electron-hole pairs originating from different valleys connected by vanishing dipole matrix elements, rendering them dark. The excitons group into spin singlets and triplets, with triplets being dark as they cannot couple optically to the ground state, which is a singlet. Several dark low-energy excitons highlight the potential of BLG QDs as a candidate for efficient photon storage [65].

In the subsequent chapter, we will compare the absorption obtained here with the results obtained when including trigonal warping effects and a shallow confinement depth, which further amplifies the effects of trigonal warping on the excitonic spectra.

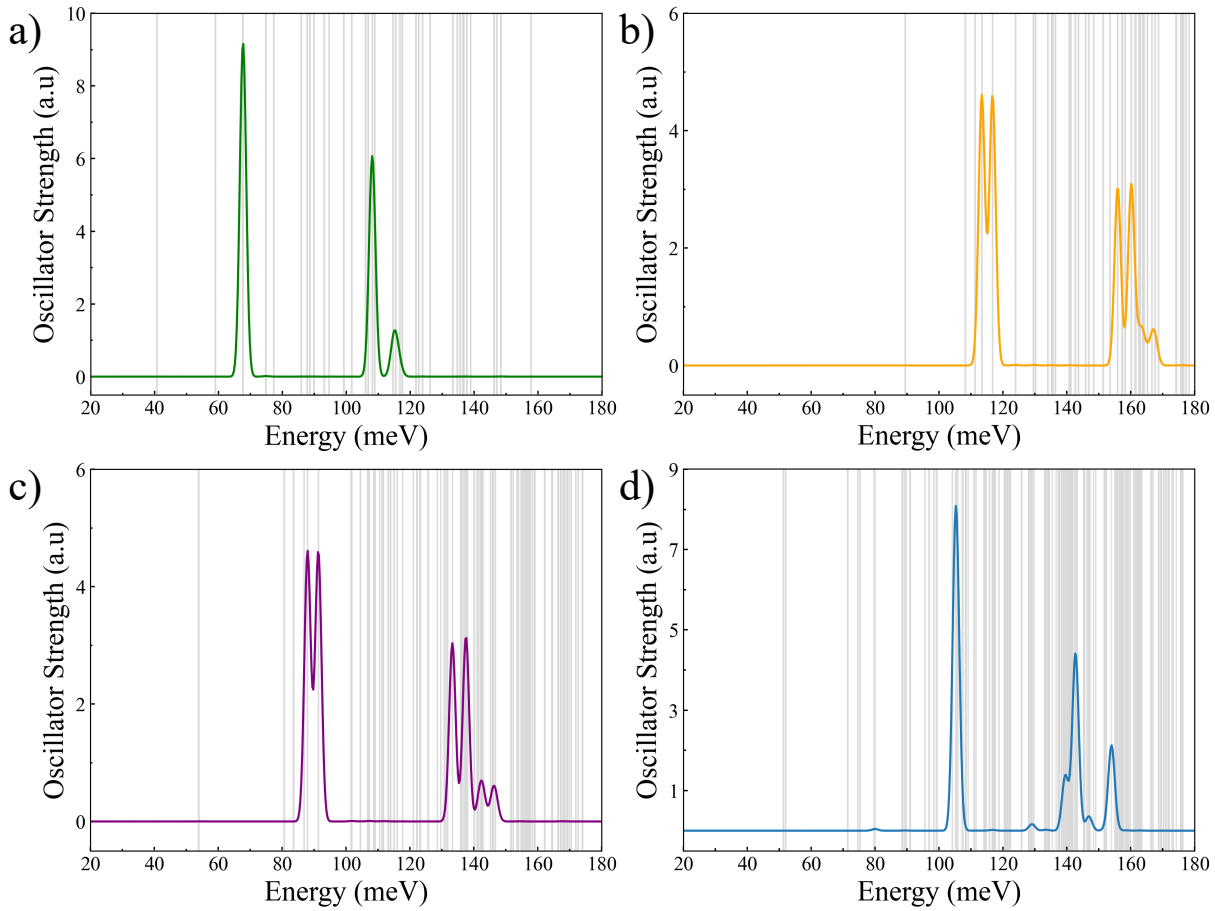

Figure 3.6: Absorption spectra including different levels of electron-electron interaction. Absorption spectra in the case of (a) noninteracting electron-hole pairs. (b) renormalized by self-energy. (c) self-energy and attractive direct and repulsive exchange interaction. (d) all electron-electron interactions, including correlation.

Chapter 4

Trigonal Warping Effects in Gated Bilayer Graphene Quantum Dots

I would like to note that this chapter is based on Ref. 66 except with more details provided.

Recently, the effects of trigonal warping in biased Bernal-stacked BLG have become of interest [7, 95–101]. The interplay of TW with strong electron-electron interactions, van Hove singularities, and a large applied electric field has led to isospin phase transitions [7,96,97], along with correlated phases exhibiting metallic and insulating properties [98]. In gated BLG QDs, which exhibit C_3 symmetry due to TW, it was found that under specific conditions, three-fold degenerate QD energy levels in each K-valley can arise [102, 103]. This three-fold degeneracy results from the presence of the three minivalleys around each K-valley. While its effects have been studied in the context of transport measurements, resulting in the bunching of twelve conductance resonances [103], its impact on excitonic and optical properties remains unexplored.

In this chapter, we extend our prior theory of excitons in a gated BLG QD from chapter 3. The focus shifts to modulating the depth of the confining potential and analyzing TW effects on the optical properties. This chapter is structured as follows. We begin by analyzing the effect of TW on the band structure of the biased BLG system. Next, we discuss the combined effect of the confining potential depth and the presence of three

minivalleys on the QD level degeneracies and optical selection rules. Finally, we present the excitonic energy and absorption spectra and identify the optical signatures of strong and weak TW.

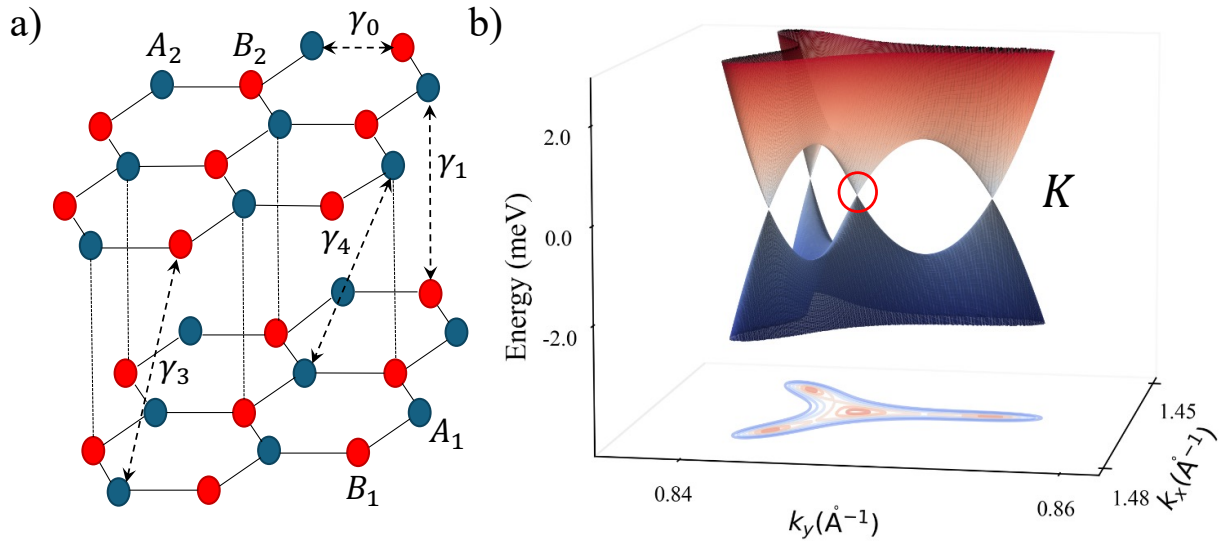

Figure 4.1: Band structure of gated AB-stacked BLG. (a) 3-dimensional view of AB-stacked BLG with atoms from sublattices A_1 and B_1 (A_2 and B_2) on the bottom (top) layer. (b) The lowest conduction and highest valence energy bands of bilayer graphene around the K point include γ_3 but without γ_4 and applied bias.

4.1 Gated bilayer graphene with trigonal warping

Building upon the previous chapter, we consider the same Bernal-stacked BLG as illustrated in Fig. 4.1(a), where the bottom (top) layer consists of sublattices A_1 and B_1 (A_2 and B_2). We begin with bulk bilayer graphene in the absence of an applied bias as in

Eq. (2.36) but with the added inclusion of the hopping parameter γ_3:

$$H_{\text{bulk}}(\vec{k}) = \begin{pmatrix} 0 & \gamma_0 f(\vec{k}) & 0 & \gamma_3 f^*(\vec{k}) \\ \gamma_0 f^*(\vec{k}) & 0 & \gamma_1 & 0 \\ 0 & \gamma_1 & -0 & \gamma_0 f(\vec{k}) \\ \gamma_3 f(\vec{k}) & 0 & \gamma_0 f^*(\vec{k}) & 0 \end{pmatrix}, \tag{4.1}$$

where the parameter γ_3 introduces the next NN interlayer hopping as shown in Fig. 4.1(a). This adds the effects of trigonal warping on the band structure presented around the K point in Fig. 4.1(b). We can see the formation of three additional Dirac cones around the K point, which meet when there is no applied bias. Now we include the hopping parameter γ_4 and an applied electric field to the Hamiltonian in Eq. (4.1) to obtain:

$$H_{\text{bulk}}(\vec{k}) = \begin{pmatrix} \frac{V_E}{2} & \gamma_0 f(\vec{k}) & \gamma_4 f(\vec{k}) & \gamma_3 f^*(\vec{k}) \\ \gamma_0 f^*(\vec{k}) & \frac{V_E}{2} & \gamma_1 & \gamma_4 f(\vec{k}) \\ \gamma_4 f^*(\vec{k}) & \gamma_1 & -\frac{V_E}{2} & \gamma_0 f(\vec{k}) \\ \gamma_3 f(\vec{k}) & \gamma_4 f^*(\vec{k}) & \gamma_0 f^*(\vec{k}) & -\frac{V_E}{2} \end{pmatrix}, \tag{4.2}$$

where γ_4 describes the next NN interlayer hopping but differs in that γ_3 represents the next NN interlayer hopping between pairs of orbitals localized on unstacked atoms, whereas γ_4 is between an orbital on a stacked and an unstacked atom, as illustrated in Fig. 4.1(a). The added effect of γ_4 is that the electron-hole symmetry is broken [104, 105]. We set $\gamma_3 = \gamma_4 = 0.12|\gamma_0|$ for the rest of our analysis [60, 64]. Fig. 4.2(a) displays a heatmap of the lowest CB energy near the K point, with $\gamma_3 = \gamma_4 = 0$ and $V_E = 380$ meV. In the absence of TW, a ring of low-energy minima emerges, which exhibits rotational symmetry and resembles the shape of a Mexican hat [88, 89]. Upon incorporating TW effects, the symmetry of our system reduces to C_3, resulting in the three minivalleys forming around the K point, as depicted in Fig. 4.2(b). Increasing the strength of the displacement field enlarges the band gap, causing the three minivalleys to shift away from each other and accentuating the depth of the three minivalleys surrounding the K and K' points [98, 103].

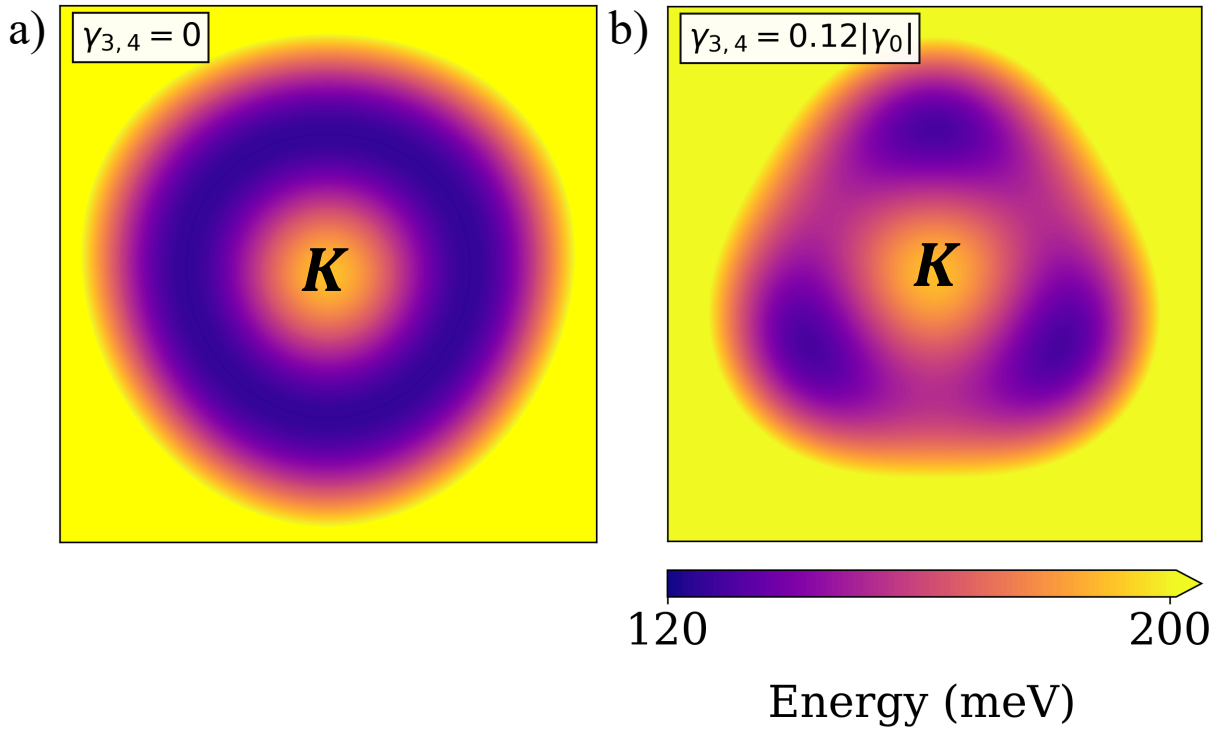

Figure 4.2: The lowest CB of the bulk band structure of BLG in the vicinity of K point (a) without the inclusion of γ_3 and γ_4 (b) with the inclusion of γ_3 and γ_4. The displacement voltage is taken to be $V_E = 380$ meV.

4.2 Evolution of quantum dot spectrum

For simplicity, we consider the single Gaussian confining potential found in Eq. (3.9):

$$V_{QD}(\rho) = \begin{cases} +V_0\, e^{-\frac{\rho^2}{R_{QD}^2}}, & z = +\frac{h}{2}, \\ -V_0\, e^{-\frac{\rho^2}{R_{QD}^2}}, & z = -\frac{h}{2}. \end{cases} \tag{4.3}$$

The explicit expression for the Fourier transform of the above confining potential is given by:

$$V_{\vec{k},\vec{k}',l} = \pm V_0 \frac{R_{QD}^2}{4\pi} A_k e^{-\frac{R_{QD}^2(\vec{k}-\vec{k}')^2}{4}}, \tag{4.4}$$

where $A_k = \frac{8\pi^2}{3\sqrt{3}a^2N}$ represents the reciprocal lattice unit cell area, and the + (−) sign corresponds to sublattices $l = A_2, B_2$, ($l = A_1, B_1$). We impose the same energy cut-off of $E_{cut} = 600$ meV on our band states as in the previous chapter.

We again solve the eigenvalue problem defined by Eq. (3.13), with a displacement voltage of $V_E = 380$ meV, QD radius of $R_{QD} = 20$ nm and confining potential depth of $V_0 = 190$ meV, but with the TW effects included. The resulting energy levels, displayed in Fig. 4.3(a), are nondegenerate when neglecting spin and valley degeneracies. In the insets of Fig. 4.3(a), we present the Fourier transform of the charge density around valley K for the first and third QD CB states. The lowest energy CB states in biased BLG originate from the three minivalleys, so one might expect a similar localization for the low-energy QD CB states. Interestingly, upon examining the Fourier transform of the charge density for the lowest QD CB state, one observes that it does not localize in the three minivalleys; instead, it appears centered around the K point. The C_3 symmetry induced by TW is noticeable when examining higher energy levels. However, for the third QD CB state, the three maxima in the charge density do not coincide with the position of the minivalleys, which suggests that TW effects do not strongly influence the low-energy QD states.

The BLG and QD parameters can be tuned to enhance the effects of TW, resulting in triple degenerate QD energy levels. The complex interplay between the inherent properties of gated BLG (C_3 symmetry from three minivalleys) and the QD confining potential possessing C_∞ symmetry governs this phenomenon. The confining potential given in Eq. (4.4) strongly couples states across momentum space for small QD radii and large confining potential depths. Notably, the three minivalleys couple, leading to low-energy QD levels localized near the center of the K point rather than the three minivalleys. As a result, the QD energy levels are singly degenerate, similar to those in parabolic confinement. Conversely, for larger QD radii and smaller confining potential depths, the confining potential weakly couples states in momentum space, leading to bulk properties manifesting more strongly in the single-particle QD energy spectrum. In this scenario, a sufficiently large applied voltage that separates the minivalleys far enough in momentum space will yield triple degenerate QD energy levels [102]. It is important to note that this triple degeneracy is robust and can be obtained for a large space of parameters.

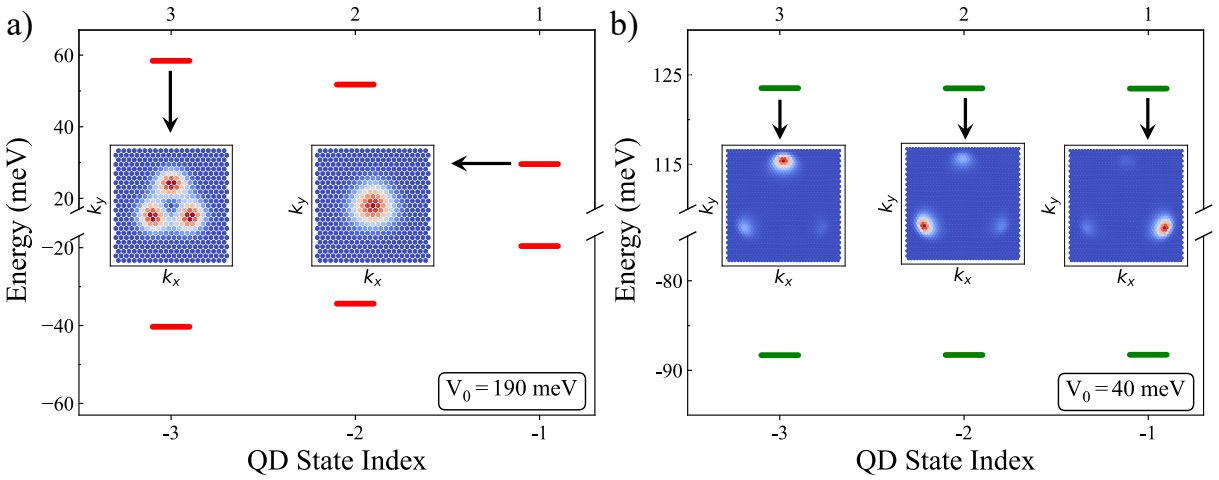

Figure 4.3: Single-particle energy spectrum of gated bilayer graphene quantum dot near the Fermi level with a QD radius of $R_{QD} = 20$ nm, displacement voltage of $V_E = 380$ meV and confining potential depth of (a) $V_0 = 190$ meV and (b) $V_0 = 40$ meV. Insets present the Fourier transform of the charge density in momentum space for QD states in valley K.

Since the displacement field of $V_E = 380$ meV is large enough to produce a significant separation of minivalleys in momentum space, we can fix V_E and R_{QD} while reducing the depth of our confining potential to achieve shallow confinement, setting $V_0 = 40$ meV. Under these conditions, a set of triple degenerate levels emerges, as depicted in Fig. 4.3(b). Upon examining the Fourier transform of the charge density for the triple-degenerate lowest CB energy levels, one observes the localization of each degenerate state around one of the three minivalleys, indicating a regime where TW's effects are significant. This reduced confinement has decreased the interlevel spacing and increased the gap between the CB and VB QD states. Additionally, this has also led to a reduction in the number of confined single-particle QD states. When selecting the confinement potential depth, one must carefully choose a depth that is shallow enough to avoid masking the effects of TW (resulting in the triple degeneracy of our QD energy spectrum) yet deep enough to yield a sufficient number of single-particle confined states, ensuring that the results are independent of the size of the computational box.

In Fig. 4.4, we illustrate the evolution of the single-particle QD spectrum as a function of

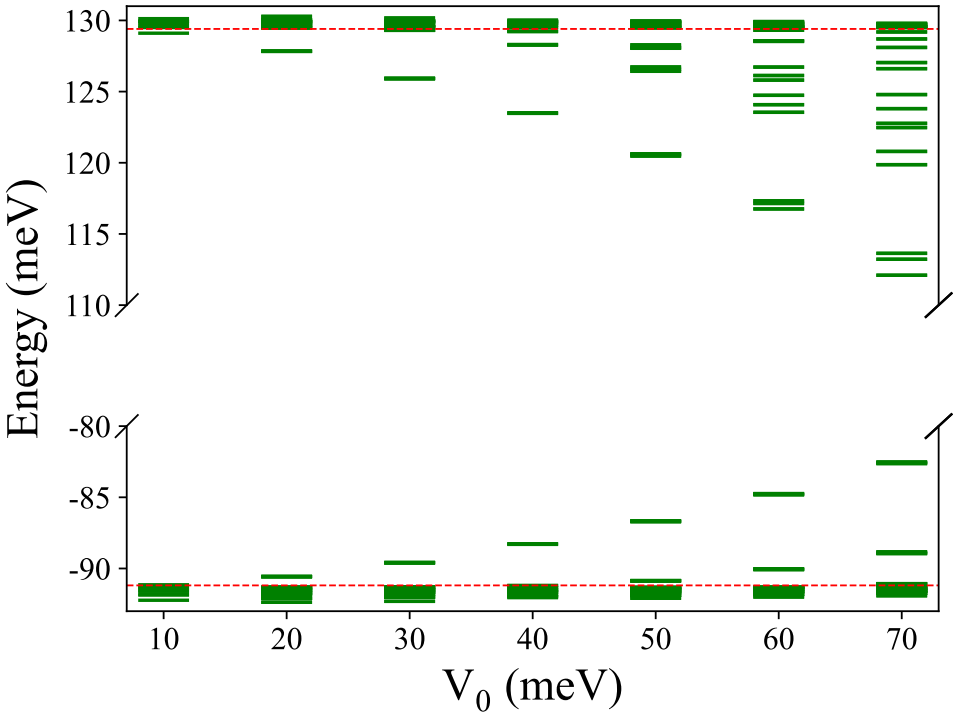

Figure 4.4: Single-particle energy spectrum of gated BLG QD as a function of confining potential depth within the 10 to 70 meV range, with $R_{QD} = 20$ nm and $V_E = 380$ meV. Green lines represent the single-particle QD energy levels, while dashed red lines at -91 and 129 meV mark the onset of the continuum in the VB and CB, respectively.

the confining potential depth V_0. Green dashes represent QD energy levels, while dashed red lines mark the border between states confined in the QD and the continuum. As V_0 increases, QD states peel off from the continuum, becoming confined within the gap. Interestingly, the rate at which QD states peel from the continuum in the CB surpasses that in the VB. This asymmetry results from γ_4, which breaks the electron-hole symmetry. Below $V_0 = 50$ meV, the QD levels exhibit triple degeneracy. However, when $V_0 = 60$ meV, we observe a small splitting of the triple degenerate shells in the CB. As the confining potential depth reaches 70 meV, the previously degenerate levels in the CB separate into three distinct QD energy levels, although the triple degeneracy persists in the VB. This observation indicates that while QD states in the CB are more easily confined, maintaining

the triple degeneracy is more challenging in the CB than in the VB.

4.3 Effect of trigonal warping on the optical selection rules

Now that we have obtained the single-particle QD states, the next step is to examine the interaction of the BLG QD with light. The aim is to explore the influence of a shallow confining potential and TW on the oscillator strengths and optical selection rules. We incorporate the coupling of light with different states through dipole matrix elements $\vec{D}_{p,q} = \langle p|\vec{r}|q\rangle$, which connect the QD states p and q, with $\vec{r}$ denoting the electron position. In Fig. 4.5(a), black arrows connect states in the VB and CB with large DMEs for a single valley, considering a deep confining potential of $V_0 = 190$ meV. In contrast to self-assembled QDs [93], the state at the top of the VB (identified by the QD index -1) exhibits a weak connection to the lowest CB state ($+1$) but instead couples strongly to the third excited state ($+3$). λ_a denotes this transition. Symmetrically, the strong transition λ_b occurs between the bottom of the CB ($+1$) and the third VB state (-3). One can conduct an identical analysis with QD states in the other valley. Transitions within each valley can be analyzed separately, as QD states from different valleys do not optically couple.

In Fig. 4.5(c), we present the joint optical density of states for non-interacting electron-hole pairs. We label the transitions corresponding to each peak, and as observed in our previous work [60], the brightest peaks correspond to the transitions λ_a and λ_b. In contrast to the scenario without TW considered in the previous chapter, the transition across the gap λ_c possesses a small but nonzero oscillator strength. This enhancement of the oscillator strength across the gap arises from the TW effect in the bulk Hamiltonian given by Eq. (3.8), which reduces the symmetry around the K and K' points to C_3 [26]. A better understanding can be derived considering an effective mass model, where the difference of angular momentum m between these two states involved in transition λ_c is $+2$ (-2) in valley K (K') when TW is neglected (more details in chapter 5). A photon changes the total angular momentum quantum number m by ± 1 [26], which is why this transition is

dark. However, with the inclusion of TW, the cylindrical symmetry around the K and K' points is broken, resulting in a difference in angular momentum between the QD states at the top of the VB and the bottom of the CB closer to ± 1, yielding a brightening of λ_c.

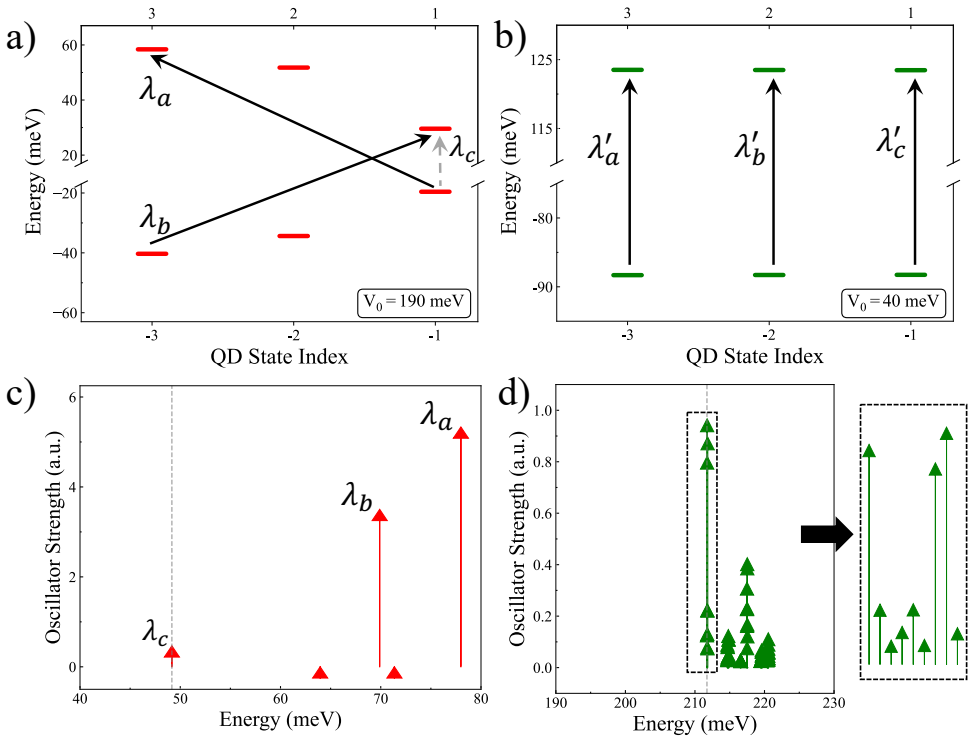

Figure 4.5: Dipole moments for optical transitions. (a,b) Single-particle energy spectrum of gated BLG QD near the Fermi level for a single valley with $V_0 = 190$ meV/40 meV. Black arrows connect pairs of VB and CB states characterized by significant dipole matrix elements, and a dashed grey arrow connects the dark transition across the gap. (c,d) Joint optical density of states for the non-interacting electron and hole in BLG QD with $V_0 = 190$ meV/40 meV. Red/green arrows show the magnitude of the corresponding dipole elements. As the transitions occur at the same energy, we split the peaks manually to display the nine transitions to the right of (d).

After tuning the depth of the confining potential to $V_0 = 40$ meV, triple degenerate energy levels emerge in the VB and CB, resulting in nine possible transitions across the band gap. Three of these nine transitions are bright and labeled as λ'_a, λ'_b, and λ'_c, as

illustrated in Fig. 4.5(b). These three bright transitions exhibit similar oscillator strengths as displayed in Fig. 4.5(d) and originate from transitions between VB and CB states localized around the same minivalley. In the subsequent sections focusing on excitons and absorption, we explore how including electron-electron interactions modifies the observed light-matter interaction and how these new selection rules impact the brightness of the low-energy exciton states.

4.4 Trigonal warping effects on exciton spectra

In this section, we study excitons and analyze the effects of combined shallow confinement and TW on the exciton spectrum. As in the previous chapter, we begin with the exciton wavefunction $|\Psi^\mu\rangle$ for exciton state μ as a linear combination of electron-hole pair excitations conserving S_z:

$$|\Psi^\mu\rangle = \sum_{p,q,\sigma} A^\mu_{p,q,\sigma} c^\dagger_{q,\sigma} c_{p,\sigma} \, |GS\rangle \, . \tag{4.5}$$

The amplitudes $A^\mu_{p,q,\sigma}$ and excitonic energies E_μ can be obtained by solving the Bethe-Salpeter equation, which was derived in section 2.3. We solve the Bethe-Salpeter equation in the subspace of 32 QD states around the Fermi level for a confining potential depth of $V_0 = 190$ meV, including the effects of TW. Fig. 4.6(a) presents the resulting excitonic energy spectrum.

We observe eight low-energy exciton states, as in the previous chapter, without trigonal warping effects; this can be understood by first examining noninteracting electron-hole pairs. We start by constructing electron-hole pairs from states at the top of the VB and bottom of the CB while conserving S_z. This involves removing an electron from the top of the VB (-1) and placing this electron on the lowest CB state ($+1$) in Fig. 4.5(a). Due to the spin and valley degeneracies of the QD level, there are two possible electron-hole pairs in each valley and four pairs between valleys (including spin), resulting in eight electron-hole pair configurations constructed across the gap. These eight configurations

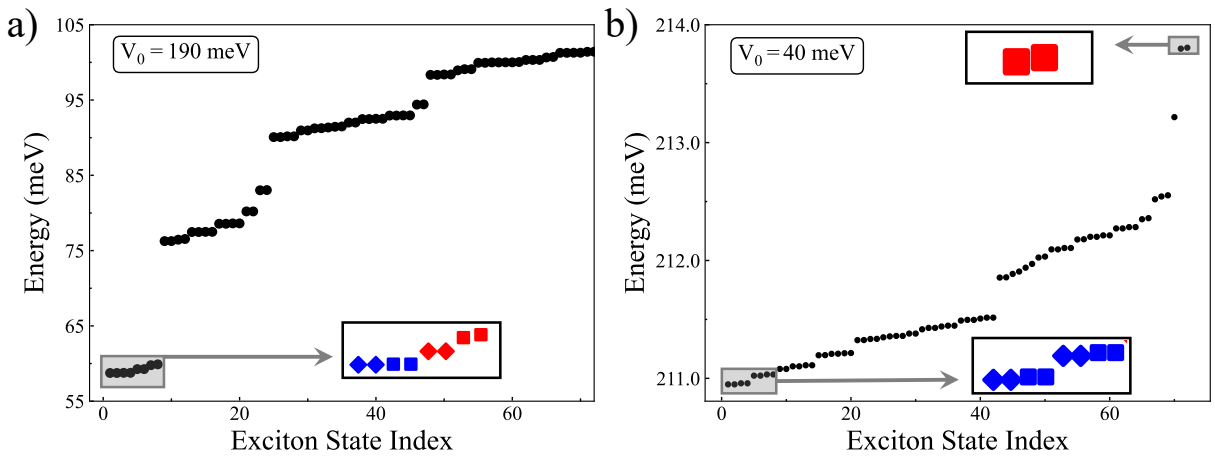

Figure 4.6: Excitonic energy spectra accounting for all electron-electron interaction for confining potential depths of (a) $V_0 = 190$ meV and (b) $V_0 = 40$ meV. The inset boxes highlight the 8 lowest (bottom right) and 2 highest (middle right) energy states. The states are labeled as intervalley (blue), intravalley (red), singlet (square), and triplet (diamond).

are degenerate; however, upon the inclusion of interactions, the eight configurations mix and separate in energy. The configurations are categorized as intervalley and intravalley electron-hole pairs, where the electron and hole can either be from QD states in different or the same valleys.

While the direct interaction is valley-independent, the exchange interaction is larger within a valley than between valleys. Intervalley electron-hole pairs increase the valley polarization compared to intravalley pairs, resulting in lower energy for intervalley pairs through increased exchange interaction. These excitons can be further categorized by spin as singlets or triplets, with triplets having lower energy due to exchange interaction.

As previously mentioned, by tuning the depth of the confining potential to $V_0 = 40$ meV, the number of confined states around the Fermi level has decreased. Upon examining Fig. 4.4, one observes that for $V_0 = 40$, three CB and one VB states are within the gap. Since each green QD level represents three degenerate QD levels, this implies the confinement of three VB and nine CB states for a single valley. Consequently, including both valleys, we have six VB and eighteen CB confined states. Hence, we solve the Bethe-

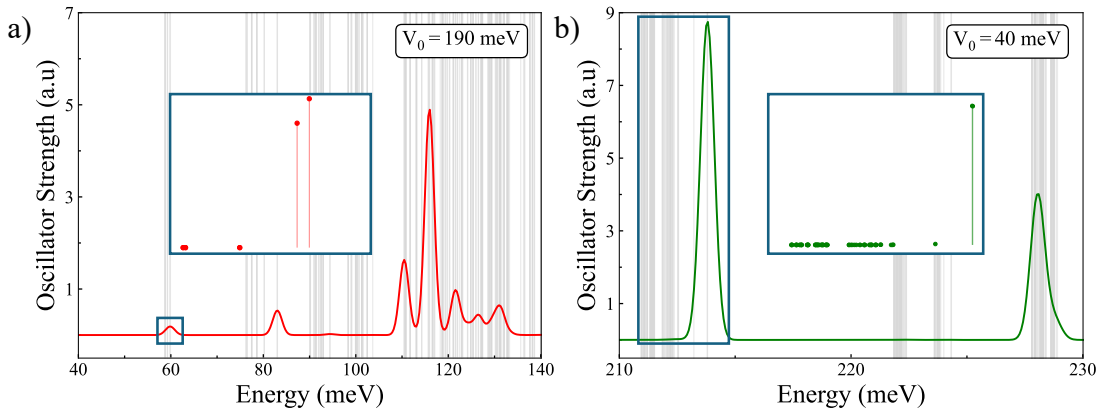

Figure 4.7: Exciton absorption spectrum with a confining potential depth of (a) $V_0 = 40$ meV and (b) $V_0 = 190$ meV. The solid lines depict the Gaussian broadened absorption spectrum, while the insets showcase the unbroadened spectrum, specifically focusing on the low-energy region. Grey vertical lines correspond to the energies of the excitonic states.

Salpeter equation in the subspace of 24 single-particle QD states around the Fermi level and present the low-energy exciton spectrum in Fig. 4.6(b). These 24 QD states give the most important contributions to the low-energy exciton spectrum.

The triple degeneracy, combined with spin and valley degeneracy, leads to 72 one-pair excitations across the gap, conserving $S_z = 0$. These one-pair excitations represent the dominant configurations forming the 72 low-energy exciton states. The ground state exciton remains an intervalley triplet, while the two highest energy $1s$ excitons are intravalley singlets. These two $1s$ intravalley excitons are primarily composed of one-pair excitation involving states participating in the bright transitions λ'_a, λ'_b and λ'_c. They are formed by one-pair excitations between QD states localized around the three minivalleys. Accordingly, we denote these two high-energy $1s$ intravalley excitons as the 'minivalley excitons'.

4.5 Absorption spectra with trigonal warping

We now investigate the absorption of a single photon by the gated BLG QD, which is excited from the ground state to an exciton state optically. The absorption spectrum gives

the probability that a photon with energy ω is absorbed as:

$$A(\omega) = \sum_{\mu} \left| \sum_{p,q,\sigma} \vec{\epsilon}_{\pm} \cdot \vec{D}_{q,p} (A^{\mu}_{p,q,\sigma})^{*} \right|^{2} \delta(E_{\mu} - \omega). \tag{4.6}$$

As in the previous chapter, we consider circularly polarized light with $\vec{\epsilon}_{\pm} = \frac{1}{\sqrt{2}}(1, \pm i)$ and we again assume that the initial state is the ground state, corresponding to a fully occupied VB. Fig. 4.7(a) displays the absorption spectrum obtained from Eq. (4.6) for a confining potential depth of $V_0 = 190$ meV. The grey vertical lines correspond to the excitonic energies E_{μ}, and the red line corresponds to the Gaussian broadened absorption spectrum. Notably, a small peak around 60 meV is observed for the low-energy exciton, corresponding to the small DME of the dark transition λ_c as observed in Fig. 4.5(c). However, at higher energies, around 116 meV, one observes a large peak corresponding to the optically bright transitions λ_a and λ_b.

We now contrast this scenario with the absorption spectrum obtained for a QD with a shallow confining potential depth of $V_0 = 40$ meV, depicted in Fig. 4.7(b). Here, one notices a large peak at around 214 meV, corresponding to optical transitions λ'_a, λ'_b, and λ'_c. An inset displays the unbroadened absorption spectrum; the bright peak arises due to the two minivalley excitons. Remarkably, these two minivalley excitons are the only bright $1s$ excitons, while the remaining seventy $1s$ exciton states are dark. This phenomenon arises from electron-electron interactions, which split exciton states into intervalley and intravalley excitons. Intervalley excitons consist of electron-hole pairs originating from different valleys connected by vanishing dipole matrix elements, rendering them dark. The excitons group into spin singlets and triplets, with triplets being dark.

Moreover, an exciton can only be bright if the dominant electron-hole pair configurations consist of optically active states connected by DMEs. The two minivalley excitons are intravalley singlet excitons built predominantly of one-pair excitations involved in the bright transitions and, thereby, are bright. The abundance of dark, low-energy excitons highlights the potential of BLG QDs as an excellent candidate for efficient photon storage [65]. Furthermore, the energy difference between the ground state and the first bright

exciton state has decreased, potentially allowing for control over the radiative lifetime of these excitons [85], thus offering customizable emission properties in the THz photon energy regime.

Chapter 5

Effective Mass Model for Bilayer Graphene Quantum Dots

In this chapter, we present an effective mass model for bilayer graphene quantum dots. This model will help us better understand the optical selection rules obtained in Chapter 3, where the effects of the hopping parameters γ_3 and γ_4 were neglected. By examining the generalized angular momentum of discrete QD states, we gain a deeper insight into the optical selection rules for bright and dark transitions compared to the atomistic model. We will begin with a parabolic confining potential and examine the resulting energy spectrum as a function of angular momenta. However, the main focus of this chapter will be on the more familiar Gaussian confinement that has been utilized throughout this thesis.

5.1 Parabolic confinement

We begin by considering the same lattice geometry for the BLG system described in section 2.1.2, where we have the NN vectors given by:

$$\vec{\delta}_1 = \vec{b}, \tag{5.1a}$$

$$\vec{\delta}_2 = \vec{b} - \vec{a}_1, \tag{5.1b}$$

$$\vec{\delta}_3 = \vec{b} - \vec{a}_2 - \vec{a}_1, \tag{5.1c}$$

where $\vec{a}_1 = a(0, \sqrt{3}), \vec{a}_2 = \frac{a}{2}(3, -\sqrt{3})$, and $\vec{b} = \frac{a}{2}(1, \sqrt{3})$ with $a = 0.143$ nm being the NN in-plane both length. One can solve for the K points, one of which is given by $\vec{K} = \left(\frac{2\pi}{3a}, \frac{2\pi}{3a\sqrt{3}}\right)$. We can expand $f(\vec{k})$ around $\vec{K}$ as:

$$f(\vec{K} + \vec{q}) \approx f(\vec{K}) + f'(\vec{K}) \cdot \vec{q} = f'(\vec{K}) \cdot \vec{q}, \tag{5.2}$$

where we have used the fact that $f(\vec{K}) = 0$. Since $f(\vec{K}) = \sum_i e^{i\vec{K}\cdot\vec{\delta}_i}$ we can expand Eq. (5.2) as:

$$\begin{aligned} f(\vec{K} + \vec{q}) &= i\vec{q} \cdot \vec{\delta}_1 e^{i\vec{K}\cdot\vec{\delta}_1} + i\vec{q} \cdot \vec{\delta}_2 e^{i\vec{K}\cdot\vec{\delta}_2} + i\vec{q} \cdot \vec{\delta}_3 e^{i\vec{K}\cdot\vec{\delta}_3} \\ &= i\vec{q} \cdot \vec{\delta}_1 e^{i\frac{2\pi}{3}} + i\vec{q} \cdot \vec{\delta}_2 e^{-i\frac{2\pi}{3}} + i\vec{q} \cdot \vec{\delta}_3 \\ &= i\left(\frac{a}{2\sqrt{3}} q_x + \frac{a}{2} q_y\right) e^{i\frac{2\pi}{3}} - i\frac{a}{\sqrt{3}} q_x e^{-i\frac{2\pi}{3}} + i\left(\frac{a}{2\sqrt{3}} q_x - \frac{a}{2} q_y\right) \\ &= i\frac{3a}{2} e^{i\frac{\pi}{3}} (q_x + iq_y). \end{aligned} \tag{5.3}$$

To remove the imaginary phase in Eq. (5.3), we can consider a rotated geometry of the bilayer graphene system where the NN vectors are given by:

$$\vec{r}_1 = \left(\frac{\sqrt{3}a}{2}, \frac{a}{2}\right), \tag{5.4a}$$

$$\vec{r}_2 = (0, -a), \tag{5.4b}$$

$$\vec{r}_3 = \left(-\frac{\sqrt{3}a}{2}, \frac{a}{2}\right), \tag{5.4c}$$

The reason for considering this rotated geometry of our lattice will become apparent after we expand $f(k)$ as we have previously done around a different K point. If we instead consider a K point given by $\vec{K} = \left(\frac{4\pi}{3\sqrt{3}a}, 0\right)$, we can expand $f(\vec{k})$ around $\vec{K}$ as:

$$f(\vec{K} + \vec{q}) = -\frac{3a}{2}(q_x + iq_y). \tag{5.5}$$

We can see from Eq. (5.5) that there is no imaginary phase factor as in Eq. (5.3), which looks a bit nicer, although the physics will not change by rotating the system. From Eq. (3.8), we have the Hamiltonian describing bulk BLG in the presence of the applied electric field (neglecting the hopping parameters γ_3 and γ_4) given by:

$$H_{\text{bulk}}(\vec{k}) = \begin{pmatrix} \frac{V_E}{2} & \gamma_0 f(\vec{k}) & 0 & 0 \\ \gamma_0 f^*(\vec{k}) & \frac{V_E}{2} & \gamma_1 & 0 \\ 0 & \gamma_1 & -\frac{V_E}{2} & \gamma_0 f(\vec{k}) \\ 0 & 0 & \gamma_0 f^*(\vec{k}) & -\frac{V_E}{2} \end{pmatrix}, \tag{5.6}$$

where we can now substitute the expression for $f(\vec{k})$ expanded around $\vec{K}$ in Eq. (5.5) into the above bulk Hamiltonian to obtain:

$$H_{\text{bulk}}(\vec{q}) = \begin{bmatrix} \frac{V_E}{2} & -\gamma_0 \frac{3a}{2} q_+ & 0 & 0 \\ -\gamma_0 \frac{3a}{2} q_- & \frac{V_E}{2} & \gamma_1 & 0 \\ 0 & \gamma_1 & -\frac{V_E}{2} & -\gamma_0 \frac{3a}{2} q_+ \\ 0 & 0 & -\gamma_0 \frac{3a}{2} q_- & -\frac{V_E}{2} \end{bmatrix}. \tag{5.7}$$

where we have defined $q_+ = q_x + iq_y$ and $q_- = q_x - iq_y$. We want to construct a quantum dot that confines electrons and holes on the two layers of the bilayer graphene while maintaining that the potential is zero at the center of the dot. We choose a parabolic confinement of the form:

$$V(x,y) = \begin{cases} -\frac{1}{2} m\Omega_0^2 (x^2+y^2), & z = +\frac{h}{2}, \\ +\frac{1}{2} m\Omega_0^2 (x^2+y^2), & z = -\frac{h}{2}, \end{cases} \tag{5.8}$$

where m is the mass of a free electron and Ω_0 is the angular frequency which will be used as a scaling factor for the potential. Using the confining potential in Eq. (5.8) allows us to write the QD Hamiltonian as:

$$H_{\text{QD}} = \begin{bmatrix} \frac{1}{2} m\Omega_0^2 (x^2+y^2) & -\gamma_0 \frac{3a}{2} \hat{q}_+ & 0 & 0 \\ -\gamma_0 \frac{3a}{2} \hat{q}_- & \frac{1}{2} m\Omega_0^2 (x^2+y^2) & \gamma_1 & 0 \\ 0 & \gamma_1 & -\frac{1}{2} m\Omega_0^2 (x^2+y^2) & -\gamma_0 \frac{3a}{2} \hat{q}_+ \\ 0 & 0 & -\gamma_0 \frac{3a}{2} \hat{q}_- & -\frac{1}{2} m\Omega_0^2 (x^2+y^2) \end{bmatrix}, \tag{5.9}$$

In an effective mass or envelope function approximation, we will move from atomistic to continuous space by replacing $\hat{q}_x = -i\frac{\partial}{\partial x}$ and $\hat{q}_y = -i\frac{\partial}{\partial y}$.

We aim to express the QD Hamiltonian in Eq. (5.9) using the raising and lowering operators of the two-dimensional harmonic oscillator. To achieve this, we begin by recalling the Hamiltonian for the two-dimensional harmonic oscillator is given by [106, 107]:

$$H = -\frac{\hbar^2}{2m} \left(\frac{\partial^2}{\partial x^2} + \frac{\partial^2}{\partial y^2} \right) + \frac{1}{2} m\Omega_0^2 (x^2+y^2), \tag{5.10}$$

which can be written in terms of raising and lowering operators as:

$$H = \Omega_0 \left(a^\dagger a + \frac{1}{2} \right) + \Omega_0 \left(b^\dagger b + \frac{1}{2} \right), \tag{5.11}$$

where the operators $a^\dagger(a)$ and $b^\dagger(b)$ create (annihilate) clockwise and counter-clockwise motion of electrons. The eigenstates of the above Hamiltonian are given by [93, 106, 108, 109]:

$$|n_L, n_R\rangle = \frac{1}{\sqrt{n_L!\, n_R!}} (a^\dagger)^{n_L} (b^\dagger)^{n_R} |0, 0\rangle, \tag{5.12}$$

where n_L and n_R are the number of clockwise and counterclockwise motion, and the angular momentum is hence given by $n_L - n_R$ and $|0, 0\rangle$ is the harmonic oscillator ground state. The explicit expression for the raising and lowering operators of the two-dimensional harmonic oscillator are given by:

$$a = \frac{1}{2} \left(\frac{1}{l\sqrt{2}} (x - iy) + l\sqrt{2} \left(\frac{\partial}{\partial x} - i \frac{\partial}{\partial y} \right) \right), \tag{5.13a}$$

$$b = \frac{1}{2} \left(\frac{1}{l\sqrt{2}} (x + iy) + l\sqrt{2} \left(\frac{\partial}{\partial x} + i \frac{\partial}{\partial y} \right) \right), \tag{5.13b}$$

$$a^\dagger = \frac{1}{2} \left(\frac{1}{l\sqrt{2}} (x + iy) - l\sqrt{2} \left(\frac{\partial}{\partial x} + i \frac{\partial}{\partial y} \right) \right), \tag{5.13c}$$

$$b^\dagger = \frac{1}{2} \left(\frac{1}{l\sqrt{2}} (x - iy) - l\sqrt{2} \left(\frac{\partial}{\partial x} - i \frac{\partial}{\partial y} \right) \right), \tag{5.13d}$$

where $l = \sqrt{\frac{\hbar}{2m\Omega_0}}$ is the oscillator length.

We can express terms in the QD Hamiltonian in Eq. (5.9) in terms of the raising and lowering operators given in Eq. (5.13) as:

$$\frac{1}{2} m^* \Omega_0^2 (x^2 + y^2) = \frac{1}{2} \hbar \Omega_0 (1 + a^\dagger a + b^\dagger b + a^\dagger b^\dagger + ab), \tag{5.14a}$$

$$iq_+ = \frac{\partial}{\partial x} + i \frac{\partial}{\partial y} = \frac{1}{l\sqrt{2}} (b - a^\dagger). \tag{5.14b}$$

Using Eq. (5.14), we can write the QD Hamiltonian in Eq. (5.9) as:

$$H_{\mathrm{QD}} = \begin{bmatrix} H_+ & H_{\gamma_1} \\ H_{\gamma_1}^\dagger & H_- \end{bmatrix}, \tag{5.15}$$

with 2×2 block components given by:

$$H_+ = \begin{bmatrix} \hat{A} & \hat{B} \\ \hat{B}^\dagger & \hat{A} \end{bmatrix}, \tag{5.16a}$$

$$H_{\gamma_1} = \begin{bmatrix} 0 & 0 \\ \gamma_1 & 0 \end{bmatrix}, \tag{5.16b}$$

$$H_{\gamma_1}^\dagger = \begin{bmatrix} 0 & \gamma_1 \\ 0 & 0 \end{bmatrix}, \tag{5.16c}$$

$$H_- = \begin{bmatrix} -\hat{A} & \hat{B} \\ \hat{B}^\dagger & -\hat{A} \end{bmatrix}, \tag{5.16d}$$

where we defined the operators:

$$\hat{A} = \frac{1}{2}\hbar\Omega_0 \left(1 + a^\dagger a + b^\dagger b + a^\dagger b^\dagger + ab\right), \tag{5.17a}$$

$$\hat{B} = i\gamma_0 \frac{3a}{2} \frac{1}{l\sqrt{2}} (b - a^\dagger). \tag{5.17b}$$

We want to construct basis states and diagonalize the QD Hamiltonian in Eq. (5.15) for different values of $n_L - n_R$, corresponding to the angular momentum m. We now consider a four-component spinor solution of the QD Hamiltonian to be of the form:

$$\varphi = \begin{bmatrix} |\Psi_{A_1}\rangle \\ |\Psi_{B_1}\rangle \\ |\Psi_{A_2}\rangle \\ |\Psi_{B_2}\rangle \end{bmatrix}. \tag{5.18}$$

We recall that the eigenstates of the two-dimensional Harmonic oscillator are given by

Eq. (5.12), which we will use as a basis for the wavefunction. Note that the operators $a^\dagger(a)$ and $b^\dagger(b)$ increase (decrease) the values of n_L and n_R by one, respectively. Upon examining the (1,1) component of H_+, which conserves the value of $n_L - n_R$ and acts on the $|\Psi_{A_1}\rangle$ component of the spinor solution in Eq. (5.18), we expand $|\Psi_{A_1}\rangle$ in the following basis:

$$|\Psi_{A_1}\rangle = \sum_{i=1}^{N} A_i |n_L + i, n_R + i\rangle, \tag{5.19}$$

where N is a cutoff in the basis size. This cutoff must be large enough to ensure the results converge sufficiently and do not depend on the basis size. We construct the basis by considering a particular angular momentum $m = n_L - n_R$, if $m > 0$, we set $n_L = m$ and $n_R = 0$; if $m < 0$, we set $n_L = 0$ and $n_R = -m$.

We now consider the (1,2) component of H_+, which acts on the spinor component $|\Psi_{B_1}\rangle$ and increases the value of $n_L - n_R$ by one. To preserve the value of $n_L - n_R$, we expand $|\Psi_{B_1}\rangle$ as:

$$|\Psi_{B_1}\rangle = \sum_{i=1}^{N} B_i |n_L + i - 1, n_R + i\rangle. \tag{5.20}$$

If we now examine the (2,2) component of H_+ and the (2,1) component of H_{γ_1}, both located in the second row of the QD Hamiltonian in Eq. (5.15), we see that they act on $|\Psi_{B_1}\rangle$ and $|\Psi_{A_2}\rangle$, respectively. Neither of these components change the value of $n_L - n_R$, indicating that this value remains the same between $|\Psi_{B_1}\rangle$ and $|\Psi_{A_2}\rangle$. Thus, we can expand $|\Psi_{A_2}\rangle$ similarly as:

$$|\Psi_{A_2}\rangle = \sum_{i=1}^{N} C_i |n_L + i - 1, n_R + i\rangle. \tag{5.21}$$

Lastly, examining the (1,1) and (1,2) components of H_-, which are in the third rows of the QD Hamiltonian and act on $|\Psi_{A_2}\rangle$ and $|\Psi_{B_2}\rangle$ components, we observe that the value of $n_L - n_R$ must be one less in $|\Psi_{B_2}\rangle$ than in $|\Psi_{A_2}\rangle$. Therefore we expand $|\Psi_{B_2}\rangle$ as:

$$|\Psi_{B_2}\rangle = \sum_{i=1}^{N} D_i |n_L + i - 2, n_R + i\rangle. \tag{5.22}$$

Now that we have the form of the four component spinor, we can construct the basis states and diagonalize the QD Hamiltonian in Eq. (5.15) for different values of angular momentum m. A basis size consisting of 100 two-dimensional harmonic oscillator eigenstates per sublattice was found to be sufficiently large to ensure convergence of the energy spectrum for a given angular momentum m. Taking the value of $\hbar\Omega_0 = 10$ meV and varying the angular momentum from -3 to +3 results in the energy spectrum presented in Fig. 5.1. One observes that the angular momentum for the QD state at the top of the VB (labeled with index -1) is +2, while the angular momentum at the bottom of the CB (labeled 1) is 0, resulting in a difference in angular momenta of -2 between these states. This implies that the optical transition across the gap in a BLG QD with parabolic confinement would be dark since a single photon can only change the angular momentum of a state by ± 1 [26]. In the next section, we perform a similar analysis for the more familiar Gaussian confinement.

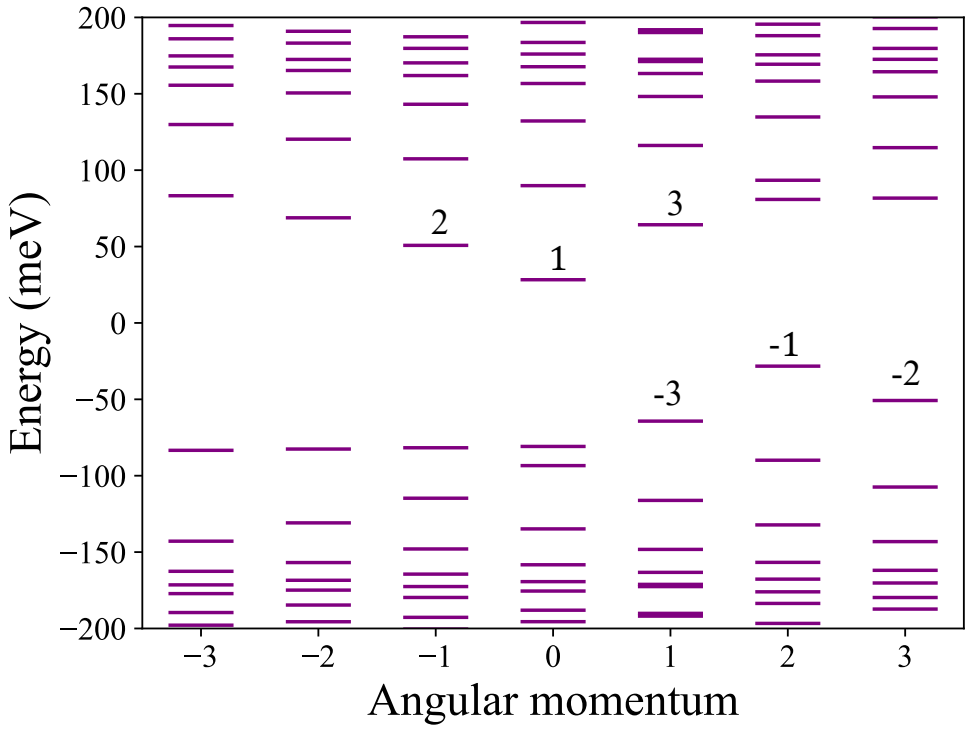

Figure 5.1: Energy spectrum for a BLG QD with parabolic confinement using an effective mass model as a function of angular momentum with $\hbar\Omega_0 = 10$ meV.

5.2 Gaussian confinement

We begin with the bulk Hamiltonian expanded around $\vec{K}$ as in Eq. (5.7):

$$H_{\text{bulk}}(\vec{q}) = \begin{bmatrix} \frac{V_E}{2} & -\gamma_0 \frac{3a}{2} q_+ & 0 & 0 \\ -\gamma_0 \frac{3a}{2} q_- & \frac{V_E}{2} & \gamma_1 & 0 \\ 0 & \gamma_1 & -\frac{V_E}{2} & -\gamma_0 \frac{3a}{2} q_+ \\ 0 & 0 & -\gamma_0 \frac{3a}{2} q_- & -\frac{V_E}{2} \end{bmatrix}. \tag{5.23}$$

We have defined $q_+ = q_x + iq_y$ and $q_- = q_x - iq_y$. To confine electrons and holes on the two different layers forming a quantum dot, we include the Gaussian confining potential as in Eq. (3.10) and the QD Hamiltonian can be written as:

$$H_{\text{QD}} = \begin{bmatrix} V(r) & -\gamma_0 \frac{3a}{2} \hat{q}_+ & 0 & 0 \\ -\gamma_0 \frac{3a}{2} \hat{q}_- & V(r) & \gamma_1 & 0 \\ 0 & \gamma_1 & -V(r) & -\gamma_0 \frac{3a}{2} \hat{q}_+ \\ 0 & 0 & -\gamma_0 \frac{3a}{2} \hat{q}_- & -V(r), \end{bmatrix}, \tag{5.24}$$

where we have defined $V(r)$ as:

$$V(r) = +\frac{V_E}{2} - (c_1 e^{-\frac{\alpha_1 r^2}{R_{QD}^2}} + c_2 e^{-\frac{\alpha_2 r^2}{R_{QD}^2}}), \tag{5.25}$$

where the parameters $c_1 = -0.018$ eV, $c_2 = 0.207$ eV, $\alpha_1 = 6.128, \alpha_2 = 1.006$ and we set the QD radius to 20 nm. To move from atomistic to continuous space, we can replace $\hat{q}_x$ and $\hat{q}_y$ with $-i\frac{\partial}{\partial x}$ and $-i\frac{\partial}{\partial y}$, respectively. And so $\hat{q}_+$ and $\hat{q}_-$ become:

$$\hat{q}_+ = -i\left(\frac{\partial}{\partial x} + i\frac{\partial}{\partial y}\right), \tag{5.26a}$$

$$\hat{q}_- = -i\left(\frac{\partial}{\partial x} - i\frac{\partial}{\partial y}\right). \tag{5.26b}$$

Since the confining potential in Eq. (5.25) is a function of the radial coordinate, it makes sense to write $\hat{q}_+$ and $\hat{q}_-$ in polar coordinates as well as:

$$\hat{q}_+ = -i\, e^{i\phi}\left(\frac{\partial}{\partial r} + \frac{i}{r}\frac{\partial}{\partial \phi}\right), \tag{5.27a}$$

$$\hat{q}_- = -i\, e^{-i\phi}\left(\frac{\partial}{\partial r} - \frac{i}{r}\frac{\partial}{\partial \phi}\right). \tag{5.27b}$$

Substituting the above expressions for $\hat{q}_+$ and $\hat{q}_-$ in polar coordinates into the QD Hamiltonian given in Eq. (5.24) results in:

$$H_{\mathrm{QD}} = \begin{bmatrix} V(r) & i\gamma_0\frac{3a}{2}\, e^{i\phi}\left(\frac{\partial}{\partial r} + \frac{i}{r}\frac{\partial}{\partial \phi}\right) & 0 & 0 \\ -\gamma_0\frac{3a}{2}q_- & V(r) & \gamma_1 & 0 \\ 0 & \gamma_1 & -V(r) & i\gamma_0\frac{3a}{2}e^{i\phi}\left(\frac{\partial}{\partial r} + \frac{i}{r}\frac{\partial}{\partial \phi}\right) \\ 0 & 0 & -\gamma_0\frac{3a}{2}q_- & -V(r), \end{bmatrix}. \tag{5.28}$$

As considered in Ref. 63, we can consider a solution of the above QD Hamiltonian in the form of a four-component spinor:

$$\varphi(r,\phi) = \begin{bmatrix} R_{A_1}(r)e^{im\phi} \\ R_{B_1}(r)e^{i(m-1)\phi} \\ R_{A_2}(r)e^{i(m-1)\phi} \\ R_{B_2}(r)e^{i(m-2)\phi} \end{bmatrix}, \tag{5.29}$$

where the integer m represents the angular momentum. This choice is appropriate as the q_+ operator raises the phase by one unit, which allows us to relate relative phases between the four sublattice components using Eq. (5.24). We expand the wavefunction of each sublattice in the basis of Bessel functions defined on a large computation box of radius R as:

$$\langle r|n,m\rangle = \frac{\sqrt{2}}{R}\frac{1}{|J_{m+1}(\alpha_m^n)|}J_m\left(\alpha_m^n\frac{r}{R}\right)\frac{1}{\sqrt{2\pi}}e^{im\phi}, \tag{5.30}$$

where n denotes the radial node number, $J_m\left(\alpha_m^n\frac{r}{R}\right)$ is the Bessel function of order m and α_m^n is the n-th zero of the m-th order Bessel function [110]. To construct the QD

Hamiltonian in the basis of the states $|n, m\rangle$, we need to compute the matrix elements:

$$\langle n_1 m_1|V(r)|n_2 m_2\rangle = \frac{2}{R^2}\frac{1}{|J_{m_1+1}(\alpha_{m_1}^{n_1})|}\frac{1}{|J_{m_2+1}(\alpha_{m_2}^{n_2})|}\int_0^R r\,dr\,V(r)\,J_{m_1}\left(\alpha_{m_1}^{n_1}\frac{r}{R}\right) \times J_{m_2}\left(\alpha_{m_2}^{n_2}\frac{r}{R}\right)\frac{1}{2\pi}\int_0^{2\pi} e^{i(m_2-m_1)\phi}\,d\phi. \quad (5.31)$$

Since $\int_0^{2\pi} e^{i(m_2-m_1)\phi}d\phi = 2\pi\delta_{m_1,m_2}$, the above equation can be simplified to:

$$\langle n_1 m_1|V(r)|n_2 m_2\rangle = \delta_{m_1,m_2}\frac{2}{R^2}\frac{1}{|J_{m_1+1}(\alpha_{m_1}^{n_1})|}\frac{1}{|J_{m_2+1}(\alpha_{m_2}^{n_2})|}\int_0^R r dr\,V(r) \times J_{m_1}(\alpha_{m_1}^{n_1}\frac{r}{R})\,J_{m_2}(\alpha_{m_2}^{n_2}\frac{r}{R}). \quad (5.32)$$

We also need to obtain an expression for the matrix elements

$$\langle n_1 m_1|q_+|n_2 m_2\rangle = -i\langle n_1 m_1|e^{i\phi}\left(\frac{\partial}{\partial r}+\frac{i}{r}\frac{\partial}{\partial\phi}\right)|n_2 m_2\rangle. \quad (5.33)$$

After some algebra, we obtain the expression:

$$\langle n_1 m_1|q_+|n_2 m_2\rangle = -\frac{2i\delta_{m_1,m_2+1}}{R}\frac{1}{|J_{m_1+1}(\alpha_{m_1}^{n_1})|}\frac{1}{|J_{m_2+1}(\alpha_{m_2}^{n_2})|}\frac{\alpha_{m_1}^{n_1}\alpha_{m_2}^{n_2}}{(\alpha_{m_1}^{n_1})^2-(\alpha_{m_2}^{n_2})^2} \times J_{m_1-1}(\alpha_{m_1}^{n_1})J_{m_1}(\alpha_{m_2}^{n_2}). \quad (5.34)$$

We can construct the QD Hamiltonian in the basis of the states $|n, m\rangle$ as in Eq. (5.30) using Eq. (5.32) and Eq. (5.34). After diagonalizing this Hamiltonian with a basis consisting of 100 Bessel functions per sublattice, we obtain the energy spectrum as a function of angular momentum presented in Fig. 5.2(a).

The QD states at the top of the VB and the bottom of the CB are labeled with indices -1 and 1, respectively. We observe that the angular momentum of the state at the top of the VB has an angular momentum of +2, while the state at the bottom of the CB has an angular momentum of 0. Therefore, the difference in angular momentum between these two QD states is -2. This explains why the dipole matrix element between these two QD

states in zero, as a single photon can only change the angular momentum of a state by ± 1 [26], and hence does not couple these two states optically.

Recall that the brightest optical transitions labeled λ_a and λ_b in Fig. 3.4(a) occur between the top of the VB and the third CB QD states, and symmetrically the bottom of the CB and the third VB state relative to the Fermi level. In Fig. 5.2(a), we see that the angular momentum of the top of the VB state (labeled -1) is +2, and the third CB state (labeled 3) has angular momentum +1, resulting in a difference in angular momenta of -1. Similarly, the difference in angular momentum between the QD states at the bottom of the CB (labeled 1), and the third VB state (labeled -3) is also -1. This matches the angular momenta of a single photon, hence there is a large oscillator strength connecting these QD states.

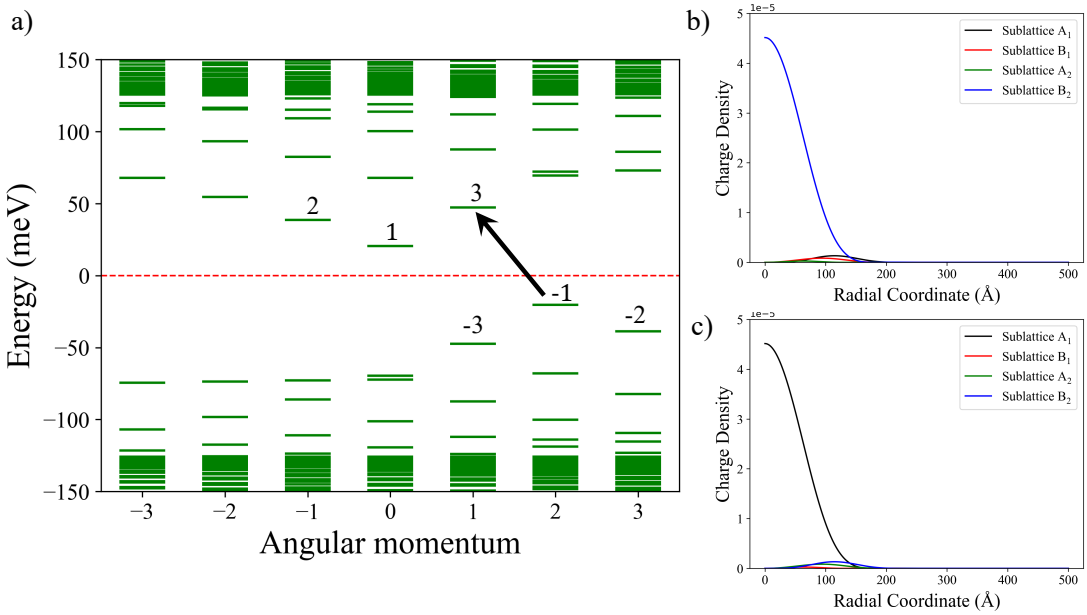

Figure 5.2: Energy spectrum for gated BLG QD using an effective mass model as a function of angular momentum for a QD radius of 20 nm. The red dashed line represents the Fermi level, and the black arrow connects an optically active transition. (b,c) Particle density for states labeled -1 and 1 in (a).

In Fig. 3.4(b), we plot the particle density as a function of the radial coordinate mea-

sured from the center of the QD for the QD state at the top of the VB. As expected, the largest contribution arises from the sublattice B_2, which is consistent with our findings in the atomistic model for the QD state with index 15/16, as shown in Fig. 3.3(b). Similarly, the dominant weight of the particle density for the QD state at the bottom of the CB resides in sublattice A_1 as presented in Fig. 3.3, again in agreement with the findings found in Fig. 3.4(c) for QD states 17/18. In both cases, we can see that the particle density decreases to nearly zero as we move radially past 20 nm, which is the radius of the QD.

Chapter 6

Conclusions

In this thesis, we have comprehensively studied the electrical and optical properties in Bernal-stacked bilayer graphene, focusing on gated bilayer graphene quantum dots. These quantum dots combine the tunability of a gate-controlled semiconductor with the ability to confine charge carriers, enabling precise manipulation of their properties. These characteristics make gated bilayer graphene quantum dots a fertile ground for numerous applications in quantum technology.

Beginning with Chapter 2, we outlined various theoretical models and numerical methods utilized throughout this thesis. We started with the tight-binding model for a single graphene layer, studying its band structure, which characterizes graphene as a semimetal, and then extended this model to bilayer graphene. Next, we described the many-body Hamiltonian for a system consisting of many electrons, discussed the configuration interaction method, and derived the Bethe-Salpeter equation to solve for the exciton energy spectrum. Additionally, we addressed the numerical challenges and techniques to compute Coulomb matrix elements to model electron-electron interactions.

Chapter 3 explored the application of a Gaussian-shaped potential profile, leading to a quantum dot that effectively confines electrons and holes on different layers. We computed the resulting quantum dot energy spectrum using an atomistic tight-binding model for millions of atoms. Subsequently, we computed dipole matrix elements and determined

the optical selection rules without trigonal warping effects. We found that the transition across the gap is dark, unlike self-assembled quantum dots, and the transition from the top of the valence band to the third excited conduction band state is bright. We computed the Coulomb matrix elements, self-energies and solved the Bethe-Salpeter equation, which we used to study the exciton fine structure. Using Fermi's golden rule, we obtained the excitonic absorption spectrum. We characterized the ground state exciton as a dark intervalley triplet exciton and observed many dark low-energy excitons. These findings highlight the potential of bilayer graphene quantum dots as a candidate for efficient photon storage.

Chapter 4 extended the theory of excitons and studied the optical properties of gated bilayer graphene quantum dots, including the effects of trigonal warping. We identified triple degenerate quantum dot energy levels emerging due to shallow confinement and trigonal warping interplay. A brightening of the oscillator strength across the gap was observed with the inclusion of trigonal warping. We determined the exciton spectrum from weak to strong trigonal warping controlled by gates. Notably, we predicted the existence of two bright $1s$ minivalley excitons and a band of low-energy dark excitons. Such electrical control of optical properties holds promise for various applications in quantum information [84], storage [65], detection [111], and emission properties in the THz photon energy range. Finally, we have demonstrated bilayer graphene quantum dots as a potential candidate for confinement of tunable neutral excitons that couple strongly to light.

In Chapter 5, we employed an effective mass model for bilayer graphene quantum dots to explain the optical selection rules previously obtained in Chapter 3 using an atomistic model that neglected trigonal warping effects. We labeled the discrete quantum dot states by generalized angular momentum. We found that the quantum dot states involved in large oscillator strengths differed in angular momenta by an amount that matched the angular momenta of the photon used to excite an electron from the valence band to the conduction band.

Bibliography

[1] Kostya S Novoselov, Andre K Geim, Sergei V Morozov, De-eng Jiang, Yanshui Zhang, Sergey V Dubonos, Irina V Grigorieva, and Alexandr A Firsov. Electric field effect in atomically thin carbon films. *science*, 306(5696):666–669, 2004.

[2] P. R. Wallace. The band theory of graphite. *Phys. Rev.*, 71:622–634, May 1947.

[3] Alev Devrim Güçlü, Pawel Potasz, Marek Korkusinski, and Pawel Hawrylak. *Graphene quantum dots*. Springer, 2014.

[4] Andre K Geim and Konstantin S Novoselov. The rise of graphene. *Nature materials*, 6(3):183–191, 2007.

[5] Klaus Zollner, Eike Icking, and Jaroslav Fabian. Electronic and spin-orbit properties of h-bn encapsulated bilayer graphene. *Phys. Rev. B*, 108:125126, Sep 2023.

[6] X. Li, K. M. Borysenko, M. Buongiorno Nardelli, and K. W. Kim. Electron transport properties of bilayer graphene. *Phys. Rev. B*, 84:195453, Nov 2011.

[7] Haoxin Zhou, Ludwig Holleis, Yu Saito, Liam Cohen, William Huynh, Caitlin L Patterson, Fangyuan Yang, Takashi Taniguchi, Kenji Watanabe, and Andrea F Young. Isospin magnetism and spin-polarized superconductivity in bernal bilayer graphene. *Science*, 375(6582):774–778, 2022.

[8] András L. Szabó and Bitan Roy. Competing orders and cascade of degeneracy lifting in doped bernal bilayer graphene. *Phys. Rev. B*, 105:L201107, May 2022.

[9] Xiu-Cai Jiang, Ze-Yi Song, Ze Ruan, and Yu-Zhong Zhang. Spontaneous charge-ordered state in bernal-stacked bilayer graphene. *Phys. Rev. Res.*, 6:013255, Mar 2024.

[10] Kostya S Novoselov, Edward McCann, SV Morozov, Vladimir I Fal'ko, MI Katsnelson, U Zeitler, D Jiang, F Schedin, and AK Geim. Unconventional quantum Hall effect and Berry's phase of 2π in bilayer graphene. *Nature physics*, 2(3):177–180, 2006.

[11] Faris Kadi and Ermin Malic. Optical properties of bernal-stacked bilayer graphene: A theoretical study. *Phys. Rev. B*, 89:045419, Jan 2014.

[12] Edward McCann and Mikito Koshino. The electronic properties of bilayer graphene. *Reports on Progress in physics*, 76(5):056503, 2013.

[13] Edward McCann and Vladimir I Fal'ko. Landau-level degeneracy and quantum hall effect in a graphite bilayer. *Physical review letters*, 96(8):086805, 2006.

[14] Edward McCann, David SL Abergel, and Vladimir I Fal'ko. The low energy electronic band structure of bilayer graphene. *The European Physical Journal Special Topics*, 148(1):91–103, 2007.

[15] Bitan Roy. Classification of massive and gapless phases in bilayer graphene. *Phys. Rev. B*, 88:075415, Aug 2013.

[16] Eduardo V. Castro, K. S. Novoselov, S. V. Morozov, N. M. R. Peres, J. M. B. Lopes dos Santos, Johan Nilsson, F. Guinea, A. K. Geim, and A. H. Castro Neto. Biased bilayer graphene: Semiconductor with a gap tunable by the electric field effect. *Phys. Rev. Lett.*, 99:216802, Nov 2007.

[17] Yuanbo Zhang, Tsung-Ta Tang, Caglar Girit, Zhao Hao, Michael C Martin, Alex Zettl, Michael F Crommie, Y Ron Shen, and Feng Wang. Direct observation of a widely tunable bandgap in bilayer graphene. *Nature*, 459(7248):820–823, 2009.

[18] Paola Gava, Michele Lazzeri, A Marco Saitta, and Francesco Mauri. Ab initio study of gap opening and screening effects in gated bilayer graphene. *Physical Review B*, 79(16):165431, 2009.

[19] Taisuke Ohta, Aaron Bostwick, Thomas Seyller, Karsten Horn, and Eli Rotenberg. Controlling the electronic structure of bilayer graphene. *Science*, 313(5789):951–954, 2006.

[20] Kin Fai Mak, Chun Hung Lui, Jie Shan, and Tony F Heinz. Observation of an electric-field-induced band gap in bilayer graphene by infrared spectroscopy. *Physical review letters*, 102(25):256405, 2009.

[21] Edward McCann. Asymmetry gap in the electronic band structure of bilayer graphene. *Phys. Rev. B*, 74:161403, Oct 2006.

[22] Feng Wang, Yuanbo Zhang, Chuanshan Tian, Caglar Girit, Alex Zettl, Michael Crommie, and Y Ron Shen. Gate-variable optical transitions in graphene. *Science*, 320(5873):206–209, 2008.

[23] Hongki Min, Bhagawan Sahu, Sanjay K. Banerjee, and A. H. MacDonald. Ab initio theory of gate induced gaps in graphene bilayers. *Phys. Rev. B*, 75:155115, Apr 2007.

[24] A. Friedlan and M. M. Dignam. Valley polarization in biased bilayer graphene using circularly polarized light. *Phys. Rev. B*, 103:075414, Feb 2021.

[25] Jeroen B Oostinga, Hubert B Heersche, Xinglan Liu, Alberto F Morpurgo, and Lieven MK Vandersypen. Gate-induced insulating state in bilayer graphene devices. *Nature materials*, 7(2):151–157, 2008.

[26] Long Ju, Lei Wang, Ting Cao, Takashi Taniguchi, Kenji Watanabe, Steven G Louie, Farhan Rana, Jiwoong Park, James Hone, Feng Wang, and Paul L Mceuen. Tunable excitons in bilayer graphene. *Science*, 358(6365):907–910, 2017.

[27] Cheol-Hwan Park and Steven G Louie. Tunable excitons in biased bilayer graphene. *Nano letters*, 10(2):426–431, 2010.

[28] Vadim M. Apalkov and Tapash Chakraborty. Controllable driven phase transitions in fractional quantum hall states in bilayer graphene. *Phys. Rev. Lett.*, 105:036801, Jul 2010.

[29] Simone Lisi, Xiaobo Lu, Tjerk Benschop, Tobias A de Jong, Petr Stepanov, Jose R Duran, Florian Margot, Irene Cucchi, Edoardo Cappelli, Andrew Hunter, Anna Tamai, Viktor Kandyba, Alessio Giampietri, Alexei Barinov, Johannes Jobst, Vincent Stalman, Maarten Leeuwenhoek, Kenji Watanabe, Takashi Taniguchi, Louk Rademaker, Sense Jan van der Molen, Milan P. Allan, Dmitri K. Efetov, and Felix Baumberger. Observation of flat bands in twisted bilayer graphene. *Nature Physics*, 17(2):189–193, 2021.

[30] Rafi Bistritzer and Allan H MacDonald. Moiré bands in twisted double-layer graphene. *Proceedings of the National Academy of Sciences*, 108(30):12233–12237, 2011.

[31] E. Suárez Morell, J. D. Correa, P. Vargas, M. Pacheco, and Z. Barticevic. Flat bands in slightly twisted bilayer graphene: Tight-binding calculations. *Phys. Rev. B*, 82:121407, Sep 2010.

[32] Aaron L Sharpe, Eli J Fox, Arthur W Barnard, Joe Finney, Kenji Watanabe, Takashi Taniguchi, MA Kastner, and David Goldhaber-Gordon. Emergent ferromagnetism near three-quarters filling in twisted bilayer graphene. *Science*, 365(6453):605–608, 2019.

[33] Xiaobo Lu, Petr Stepanov, Wei Yang, Ming Xie, Mohammed Ali Aamir, Ipsita Das, Carles Urgell, Kenji Watanabe, Takashi Taniguchi, Guangyu Zhang, Adrian Bachtold, Allan H. MacDonald, and Dmitri K. Efetov. Superconductors, orbital magnets and correlated states in magic-angle bilayer graphene. *Nature*, 574(7780):653–657, 2019.

[34] Matthew Yankowitz, Shaowen Chen, Hryhoriy Polshyn, Yuxuan Zhang, K Watanabe, T Taniguchi, David Graf, Andrea F Young, and Cory R Dean. Tuning superconductivity in twisted bilayer graphene. *Science*, 363(6431):1059–1064, 2019.

[35] Yuan Cao, Valla Fatemi, Shiang Fang, Kenji Watanabe, Takashi Taniguchi, Efthimios Kaxiras, and Pablo Jarillo-Herrero. Unconventional superconductivity in magic-angle graphene superlattices. *Nature*, 556(7699):43–50, 2018.

[36] Myungchul Oh, Kevin P Nuckolls, Dillon Wong, Ryan L Lee, Xiaomeng Liu, Kenji Watanabe, Takashi Taniguchi, and Ali Yazdani. Evidence for unconventional superconductivity in twisted bilayer graphene. *Nature*, 600(7888):240–245, 2021.

[37] Ming Xie and A. H. MacDonald. Nature of the correlated insulator states in twisted bilayer graphene. *Phys. Rev. Lett.*, 124:097601, Mar 2020.

[38] Masayuki Ochi, Mikito Koshino, and Kazuhiko Kuroki. Possible correlated insulating states in magic-angle twisted bilayer graphene under strongly competing interactions. *Physical Review B*, 98(8):081102, 2018.

[39] Yuan Cao, Valla Fatemi, Ahmet Demir, Shiang Fang, Spencer L Tomarken, Jason Y Luo, Javier D Sanchez-Yamagishi, Kenji Watanabe, Takashi Taniguchi, Efthimios Kaxiras, Ray C. Ashoori, and Pablo Jarillo-Herrero. Correlated insulator behaviour at half-filling in magic-angle graphene superlattices. *Nature*, 556(7699):80–84, 2018.

[40] Yuan Cao, Daniel Rodan-Legrain, Oriol Rubies-Bigorda, Jeong Min Park, Kenji Watanabe, Takashi Taniguchi, and Pablo Jarillo-Herrero. Tunable correlated states and spin-polarized phases in twisted bilayer–bilayer graphene. *Nature*, 583(7815):215–220, 2020.

[41] Aviram Uri, Sergio C de la Barrera, Mallika T Randeria, Daniel Rodan-Legrain, Trithep Devakul, Philip JD Crowley, Nisarga Paul, Kenji Watanabe, Takashi Taniguchi, Ron Lifshitz, Liang Fu, Raymond C. Ashoori, and Pablo Jarillo-Herrero. Superconductivity and strong interactions in a tunable moiré quasicrystal. *Nature*, 620(7975):762–767, 2023.

[42] Hyunjin Kim, Youngjoon Choi, Cyprian Lewandowski, Alex Thomson, Yiran Zhang, Robert Polski, Kenji Watanabe, Takashi Taniguchi, Jason Alicea, and Stevan Nadj-

Perge. Evidence for unconventional superconductivity in twisted trilayer graphene. *Nature*, 606(7914):494–500, 2022.

[43] Haoxin Zhou, Tian Xie, Takashi Taniguchi, Kenji Watanabe, and Andrea F Young. Superconductivity in rhombohedral trilayer graphene. *Nature*, 598(7881):434–438, 2021.

[44] I. A. Assi, J. P. F. LeBlanc, Martin Rodriguez-Vega, Hocine Bahlouli, and Michael Vogl. Floquet engineering and nonequilibrium topological maps in twisted trilayer graphene. *Phys. Rev. B*, 104:195429, Nov 2021.

[45] G William Burg, Eslam Khalaf, Yimeng Wang, Kenji Watanabe, Takashi Taniguchi, and Emanuel Tutuc. Emergence of correlations in alternating twist quadrilayer graphene. *Nature Materials*, 21(8):884–889, 2022.

[46] Eslam Khalaf, Alex J. Kruchkov, Grigory Tarnopolsky, and Ashvin Vishwanath. Magic angle hierarchy in twisted graphene multilayers. *Phys. Rev. B*, 100:085109, Aug 2019.

[47] F Pelayo García de Arquer, Dmitri V Talapin, Victor I Klimov, Yasuhiko Arakawa, Manfred Bayer, and Edward H Sargent. Semiconductor quantum dots: Technological progress and future challenges. *Science*, 373(6555):eaaz8541, 2021.

[48] Isil Ozfidan, Marek Korkusinski, A Devrim Güçlü, John A McGuire, and Pawel Hawrylak. Microscopic theory of the optical properties of colloidal graphene quantum dots. *Physical Review B*, 89(8):085310, 2014.

[49] Marek Korkusinski and Pawel Hawrylak. Atomistic theory of emission from dark excitons in self-assembled quantum dots. *Phys. Rev. B*, 87:115310, Mar 2013.

[50] Gabriel Bester, Selvakumar Nair, and Alex Zunger. Pseudopotential calculation of the excitonic fine structure of million-atom self-assembled $in_{1-x}ga_xAs$/GaAs quantum dots. *Phys. Rev. B*, 67:161306, Apr 2003.

[51] P. Hawrylak, G. A. Narvaez, M. Bayer, and A. Forchel. Excitonic absorption in a quantum dot. *Phys. Rev. Lett.*, 85:389–392, Jul 2000.

[52] M Bayer, O Stern, P Hawrylak, S Fafard, and A Forchel. Hidden symmetries in the energy levels of excitonic 'artificial atoms'. *Nature*, 405(6789):923–926, 2000.

[53] Kang L. Wang, Dongho Cha, Jianlin Liu, and Christopher Chen. Ge/si self-assembled quantum dots and their optoelectronic device applications. *Proceedings of the IEEE*, 95(9):1866–1883, 2007.

[54] T Lundstrom, W Schoenfeld, H Lee, and PM Petroff. Exciton storage in semiconductor self-assembled quantum dots. *science*, 286(5448):2312–2314, 1999.

[55] Cheng Sun, Florian Figge, Isil Ozfidan, Marek Korkusinski, Xin Yan, Liang-shi Li, Pawel Hawrylak, and John A McGuire. Biexciton binding of dirac fermions confined in colloidal graphene quantum dots. *Nano letters*, 15(8):5472–5476, 2015.

[56] Isil Ozfidan, Marek Korkusinski, and Pawel Hawrylak. Theory of biexcitons and biexciton-exciton cascade in graphene quantum dots. *Physical Review B*, 91(11):115314, 2015.

[57] Oliver Benson, Charles Santori, Matthew Pelton, and Yoshihisa Yamamoto. Regulated and entangled photons from a single quantum dot. *Phys. Rev. Lett.*, 84:2513–2516, Mar 2000.

[58] M. Ciorga, A. S. Sachrajda, P. Hawrylak, C. Gould, P. Zawadzki, S. Jullian, Y. Feng, and Z. Wasilewski. Addition spectrum of a lateral dot from coulomb and spin-blockade spectroscopy. *Phys. Rev. B*, 61:R16315–R16318, Jun 2000.

[59] Chang-Yu Hsieh, Yun-Pil Shim, Marek Korkusinski, and Pawel Hawrylak. Physics of lateral triple quantum-dot molecules with controlled electron numbers. *Reports on Progress in Physics*, 75(11):114501, 2012.

[60] Katarzyna Sadecka, Yasser Saleem, Daniel Miravet, Matthew Albert, Marek Korkusinski, Gabriel Bester, and Pawel Hawrylak. Electrically tunable fine structure of

negatively charged excitons in gated bilayer graphene quantum dots. *Physical Review B*, 109(8):085434, 2024.

[61] Daniel Miravet, Abdulmenaf Altıntaş, Alina Wania Rodrigues, Maciej Bieniek, Marek Korkusinski, and Paweł Hawrylak. Interacting holes in gated WSe_2 quantum dots. *Phys. Rev. B*, 108:195407, Nov 2023.

[62] Abdulmenaf Altıntaş, Maciej Bieniek, Amintor Dusko, Marek Korkusiński, Jarosław Pawłowski, and Paweł Hawrylak. Spin-valley qubits in gated quantum dots in a single layer of transition metal dichalcogenides. *Phys. Rev. B*, 104:195412, Nov 2021.

[63] J Milton Pereira, P Vasilopoulos, and FM Peeters. Tunable quantum dots in bilayer graphene. *Nano letters*, 7(4):946–949, 2007.

[64] Marek Korkusinski, Yasser Saleem, Amintor Dusko, Daniel Miravet, and Pawel Hawrylak. Spontaneous spin and valley symmetry-broken states of interacting massive dirac fermions in a bilayer graphene quantum dot. *Nano Letters*, 23(16):7546–7551, 2023.

[65] Yasser Saleem, Katarzyna Sadecka, Marek Korkusinski, Daniel Miravet, Amintor Dusko, and Pawel Hawrylak. Theory of excitons in gated bilayer graphene quantum dots. *Nano Letters*, 23(7):2998–3004, 2023.

[66] Matthew Albert, Daniel Miravet, Yasser Saleem, Katarzyna Sadecka, Marek Korkusinski, Gabriel Bester, and Pawel Hawrylak. Optical properties of gated bilayer graphene quantum dots with trigonal warping. *arXiv preprint arXiv:2405.09725*, 2024.

[67] Annika Kurzmann, Yaakov Kleeorin, Chuyao Tong, Rebekka Garreis, Angelika Knothe, Marius Eich, Christopher Mittag, Carolin Gold, Folkert Kornelis de Vries, Kenji Watanabe, Takashi Taniguchi, Vladimir Fal'ko, Yigal Meir, Thomas Ihn, and Klaus Ensslin. Kondo effect and spin–orbit coupling in graphene quantum dots. *Nature communications*, 12(1):6004, 2021.

[68] Luca Banszerus, K Hecker, S Möller, E Icking, K Watanabe, T Taniguchi, C Volk, and C Stampfer. Spin relaxation in a single-electron graphene quantum dot. *Nature communications*, 13(1):3637, 2022.

[69] Björn Trauzettel, Denis V Bulaev, Daniel Loss, and Guido Burkard. Spin qubits in graphene quantum dots. *Nature Physics*, 3(3):192–196, 2007.

[70] Rebekka Garreis, Chuyao Tong, Jocelyn Terle, Max Josef Ruckriegel, Jonas Daniel Gerber, Lisa Maria Gächter, Kenji Watanabe, Takashi Taniguchi, Thomas Ihn, Klaus Ensslin, et al. Long-lived valley states in bilayer graphene quantum dots. *Nature Physics*, pages 1–7, 2024.

[71] Marius Eich, František Herman, Riccardo Pisoni, Hiske Overweg, Annika Kurzmann, Yongjin Lee, Peter Rickhaus, Kenji Watanabe, Takashi Taniguchi, Manfred Sigrist, Thomas Ihn, and Klaus Ensslin. Spin and valley states in gate-defined bilayer graphene quantum dots. *Phys. Rev. X*, 8:031023, Jul 2018.

[72] Luca Banszerus, Samuel Möller, Corinne Steiner, Eike Icking, Stefan Trellenkamp, Florian Lentz, Kenji Watanabe, Takashi Taniguchi, Christian Volk, and Christoph Stampfer. Spin-valley coupling in single-electron bilayer graphene quantum dots. *Nature communications*, 12(1):5250, 2021.

[73] Luca Banszerus, Alexander Rothstein, Thomas Fabian, S Moller, Eike Icking, Stefan Trellenkamp, Florian Lentz, Daniel Neumaier, Kenji Watanabe, Takashi Taniguchi, et al. Electron–hole crossover in gate-controlled bilayer graphene quantum dots. *Nano letters*, 20(10):7709–7715, 2020.

[74] Luca Banszerus, Benedikt Frohn, Alexander Epping, Daniel Neumaier, Kenji Watanabe, Takashi Taniguchi, and Christoph Stampfer. Gate-defined electron–hole double dots in bilayer graphene. *Nano letters*, 18(8):4785–4790, 2018.

[75] Monica T Allen, Jens Martin, and Amir Yacoby. Gate-defined quantum confinement in suspended bilayer graphene. *Nature communications*, 3(1):934, 2012.

[76] S. Möller, L. Banszerus, A. Knothe, C. Steiner, E. Icking, S. Trellenkamp, F. Lentz, K. Watanabe, T. Taniguchi, L. I. Glazman, V. I. Fal'ko, C. Volk, and C. Stampfer. Probing two-electron multiplets in bilayer graphene quantum dots. *Phys. Rev. Lett.*, 127:256802, Dec 2021.

[77] Emilia Ridolfi, Duy Le, TS Rahman, ER Mucciolo, and CH Lewenkopf. A tight-binding model for MoS_2 monolayers. *Journal of Physics: Condensed Matter*, 27(36):365501, 2015.

[78] J. C. Slater and G. F. Koster. Simplified LCAO method for the periodic potential problem. *Phys. Rev.*, 94:1498–1524, Jun 1954.

[79] Takashi Yumura and Kazunari Yoshizawa. Second-order perturbational analysis of the interaction between graphite sheets. *Chemical physics*, 279(2-3):111–131, 2002.

[80] Edward McCann and Vladimir I. Fal'ko. Landau-level degeneracy and quantum hall effect in a graphite bilayer. *Phys. Rev. Lett.*, 96:086805, Mar 2006.

[81] M. Mucha-Kruczyński, O. Tsyplyatyev, A. Grishin, E. McCann, Vladimir I. Fal'ko, Aaron Bostwick, and Eli Rotenberg. Characterization of graphene through anisotropy of constant-energy maps in angle-resolved photoemission. *Phys. Rev. B*, 77:195403, May 2008.

[82] B. Partoens and F. M. Peeters. From graphene to graphite: Electronic structure around the k point. *Phys. Rev. B*, 74:075404, Aug 2006.

[83] Luca Guido Molinari. Notes on wick's theorem in many-body theory. *arXiv preprint arXiv:1710.09248*, 2017.

[84] JCG Henriques, Itai Epstein, and NMR Peres. Absorption and optical selection rules of tunable excitons in biased bilayer graphene. *Physical Review B*, 105(4):045411, 2022.

[85] Mikkel Ohm Sauer and Thomas Garm Pedersen. Exciton absorption, band structure, and optical emission in biased bilayer graphene. *Physical Review B*, 105(11):115416, 2022.

[86] Deepankur Thureja, Atac Imamoglu, Tomasz Smoleński, Ivan Amelio, Alexander Popert, Thibault Chervy, Xiaobo Lu, Song Liu, Katayun Barmak, Kenji Watanabe, Takashi Taniguchi, David J. Norris, Martin Kroner, and Puneet A Murthy. Electrically tunable quantum confinement of neutral excitons. *Nature*, 606(7913):298–304, 2022.

[87] Matthew C DeCapua, Yueh-Chun Wu, Takashi Taniguchi, Kenji Watanabe, and Jun Yan. Probing the bright exciton state in twisted bilayer graphene via resonant raman scattering. *Applied Physics Letters*, 119(1), 2021.

[88] Angelika Knothe and Vladimir Fal'ko. Influence of minivalleys and Berry curvature on electrostatically induced quantum wires in gapped bilayer graphene. *Physical Review B*, 98(15):155435, 2018.

[89] Anastasia Varlet, Marcin Mucha-Kruczyński, Dominik Bischoff, Pauline Simonet, Takashi Taniguchi, Kenji Watanabe, Vladimir Fal'ko, Thomas Ihn, and Klaus Ensslin. Tunable fermi surface topology and lifshitz transition in bilayer graphene. *Synthetic Metals*, 210:19–31, 2015.

[90] Weiming Que. Excitons in quantum dots with parabolic confinement. *Physical Review B*, 45(19):11036, 1992.

[91] M Zarenia, B Partoens, T Chakraborty, and FM Peeters. Electron-electron interactions in bilayer graphene quantum dots. *Physical Review B*, 88(24):245432, 2013.

[92] Jordan Kyriakidis, M Pioro-Ladriere, M Ciorga, AS Sachrajda, and P Hawrylak. Voltage-tunable singlet-triplet transition in lateral quantum dots. *Physical Review B*, 66(3):035320, 2002.

[93] S. Raymond, S. Studenikin, A. Sachrajda, Z. Wasilewski, S. J. Cheng, W. Sheng, P. Hawrylak, A. Babinski, M. Potemski, G. Ortner, and M. Bayer. Excitonic energy shell structure of self-assembled ingaas/gaas quantum dots. *Phys. Rev. Lett.*, 92:187402, May 2004.

[94] Michał Zieliński, M Korkusiński, and P Hawrylak. Atomistic tight-binding theory of multiexciton complexes in a self-assembled inas quantum dot. *Physical Review B*, 81(8):085301, 2010.

[95] Anna M Seiler, Nils Jacobsen, Martin Statz, Noelia Fernandez, Francesca Falorsi, Kenji Watanabe, Takashi Taniguchi, Zhiyu Dong, Leonid S Levitov, and R Thomas Weitz. Probing the tunable multi-cone band structure in bernal bilayer graphene. *Nature Communications*, 15(1):3133, 2024.

[96] Sergio C de la Barrera, Samuel Aronson, Zhiren Zheng, Kenji Watanabe, Takashi Taniguchi, Qiong Ma, Pablo Jarillo-Herrero, and Raymond Ashoori. Cascade of isospin phase transitions in bernal-stacked bilayer graphene at zero magnetic field. *Nature Physics*, 18(7):771–775, 2022.

[97] Zhiyu Dong, Margarita Davydova, Olumakinde Ogunnaike, and Leonid Levitov. Isospin-and momentum-polarized orders in bilayer graphene. *Physical Review B*, 107(7):075108, 2023.

[98] Anna M Seiler, Fabian R Geisenhof, Felix Winterer, Kenji Watanabe, Takashi Taniguchi, Tianyi Xu, Fan Zhang, and R Thomas Weitz. Quantum cascade of correlated phases in trigonally warped bilayer graphene. *Nature*, 608(7922):298–302, 2022.

[99] Frédéric Joucken, Zhehao Ge, Eberth A. Quezada-López, John L. Davenport, Kenji Watanabe, Takashi Taniguchi, and Jairo Velasco. Determination of the trigonal warping orientation in bernal-stacked bilayer graphene via scanning tunneling microscopy. *Phys. Rev. B*, 101:161103, Apr 2020.

[100] E. V. Gorbar, V. P. Gusynin, D. O. Oriekhov, and B. I. Shklovskii. Electron binding energy of donors in bilayer graphene with a gate-tunable gap. *Phys. Rev. B*, 109:165145, Apr 2024.

[101] Anastasia Varlet, Dominik Bischoff, Pauline Simonet, Kenji Watanabe, Takashi Taniguchi, Thomas Ihn, Klaus Ensslin, Marcin Mucha-Kruczyński, and Vladimir I. Fal'ko. Anomalous sequence of quantum hall liquids revealing a tunable lifshitz transition in bilayer graphene. *Phys. Rev. Lett.*, 113:116602, Sep 2014.

[102] Angelika Knothe and Vladimir Fal'ko. Quartet states in two-electron quantum dots in bilayer graphene. *Physical Review B*, 101(23):235423, 2020.

[103] Rebekka Garreis, Angelika Knothe, Chuyao Tong, Marius Eich, Carolin Gold, Kenji Watanabe, Takashi Taniguchi, Vladimir Fal'ko, Thomas Ihn, Klaus Ensslin, et al. Shell filling and trigonal warping in graphene quantum dots. *Physical Review Letters*, 126(14):147703, 2021.

[104] ZQ Li, EA Henriksen, Zhigang Jiang, Zhao Hao, Michael C Martin, P Kim, HL Stormer, and Dimitri N Basov. Band structure asymmetry of bilayer graphene revealed by infrared spectroscopy. *Physical Review Letters*, 102(3):037403, 2009.

[105] LM Zhang, ZQ Li, Dimitri N Basov, MM Fogler, Zhao Hao, and Michael C Martin. Determination of the electronic structure of bilayer graphene from infrared spectroscopy. *Physical Review B*, 78(23):235408, 2008.

[106] Pawel Hawrylak. Single-electron capacitance spectroscopy of few-electron artificial atoms in a magnetic field: Theory and experiment. *Physical review letters*, 71(20):3347, 1993.

[107] Pawel Hawrylak and Daniela Pfannkuche. Magnetoluminescence from correlated electrons in quantum dots. *Physical review letters*, 70(4):485, 1993.

[108] C. Cohen-Tannoudji, B. Diu, and F. Laloë. *Quantum Mechanics, Volume 2: Angular Momentum, Spin, and Approximation Methods*. Wiley, 2019.

[109] Lucjan Jacak, Pawel Hawrylak, and Arkadiusz Wojs. *Quantum dots*. Springer Science & Business Media, 2013.

[110] Marek Korkusinski and Pawel Hawrylak. Quantum strain sensor with a topological insulator hgte quantum dot. *Scientific reports*, 4(1):4903, 2014.

[111] Annika Kurzmann, Hiske Overweg, Marius Eich, Alessia Pally, Peter Rickhaus, Riccardo Pisoni, Yongjin Lee, Kenji Watanabe, Takashi Taniguchi, Thomas Ihn, et al. Charge detection in gate-defined bilayer graphene quantum dots. *Nano letters*, 19(8):5216–5221, 2019.